



저작자표시-비영리-변경금지 2.0 대한민국

이용자는 아래의 조건을 따르는 경우에 한하여 자유롭게

- 이 저작물을 복제, 배포, 전송, 전시, 공연 및 방송할 수 있습니다.

다음과 같은 조건을 따라야 합니다:



저작자표시. 귀하는 원저작자를 표시하여야 합니다.



비영리. 귀하는 이 저작물을 영리 목적으로 이용할 수 없습니다.



변경금지. 귀하는 이 저작물을 개작, 변형 또는 가공할 수 없습니다.

- 귀하는, 이 저작물의 재이용이나 배포의 경우, 이 저작물에 적용된 이용허락조건을 명확하게 나타내어야 합니다.
- 저작권자로부터 별도의 허가를 받으면 이러한 조건들은 적용되지 않습니다.

저작권법에 따른 이용자의 권리는 위의 내용에 의하여 영향을 받지 않습니다.

이것은 [이용허락규약\(Legal Code\)](#)을 이해하기 쉽게 요약한 것입니다.

[Disclaimer](#)

공학박사학위논문

The Study on Development of
Composites for Higher Barrier
Properties and Interfacial Phenomena

고차단성 부여를 위한 고분자 복합재료
개발 및 계면 현상에 대한 연구

2019년 8월

서울대학교 대학원

재료공학부

김 호 연

The Study on Development of
Composites for Higher Barrier
Properties and Interfacial Phenomena
고차단성 부여를 위한 고분자 복합재료
개발 및 계면 현상에 대한 연구

지도교수 서 용 석

이 논문을 김호연 박사학위논문으로 제출함
2019년 5월

서울대학교 대학원
재료공학부

김 호 연

김호연의 박사학위논문을 인준함
2019년 7월

위원장	윤재륜	(인)
부위원장	서용석	(인)
위원	유응열	(인)
위원	홍성현	(인)
위원	최형진	(인)

Abstract

The Study on Development of Composites for Higher Barrier Properties and Interfacial Phenomena

Hoyeon Kim

Department of Materials Science and Engineering

The Graduate School

Seoul National University

Composite materials are multiphase materials obtained through the artificial combination of different materials in order to attain properties that the individual components by themselves cannot attain. Composite materials can be tailored for various properties by appropriately choosing their components, their proportions, their distributions, their morphologies, their degrees of crystallinity, their crystallographic textures, as well as the structure and composition of the interface between components. Due to this strong tailorability, composite materials can be designed to satisfy the needs of technologies relating to the aerospace, automobile, electronics, construction, energy, biomedical and other industries.

The functional properties were given by the filler selection of the composite materials. Among them, the barrier (blocking) properties is an important in various industrial field and daily life. The barrier materials that protect people or objects from external sources protect the health of human body or allow to the product to operate properly. The most common barrier elements are moisture, various gases, etc. Furthermore, various external irradiations such as electromagnetic waves and radiation is an external source to be shielded.

In this study, composite materials with various barrier properties were fabricated by using light weight and ease of processing of polymer composite materials. The external sources focused on this experiment were ionizing radiation, microwaves, water vapor, and external force. In the case of radiation shielding composite materials, composites were made using bismuth, tin alloys and tungsten instead of lead. The multilayer structure was laminated to analyze radiation shielding characteristics. Through this process, X-ray and gamma ray could be effectively shielded. In addition, for the shielding of electromagnetic waves, a combination of carbon nanotubes and Sendust alloys made composite materials which are lighter than conventional shielding materials but have higher blocking efficiency. We have confirmed through various analysis that the change in electrical properties caused by the combination of the two materials is the cause of such improvement.

The study of bonding behaviors at the polymer interface has been carried out as a basic study for forming composite materials with various barrier properties into one multi-layer material. Adhesion between polymers that do not mix with each other is generally very weak. In order to overcome this problem, the adhesion between polymers was improved by adding in-situ compatibilizer or surface modification. In the process, we confirmed that the adhesive force varies with temperature and time and analyzed the cause of this behavior through additional mass analysis and surface analysis, suggesting a behavior that can reasonably understand the adhesion between polymers. In addition, the surface modification technique was used to improve the adhesion between composites and the metal oxide film. As a result, the laminates with high water vapor barrier properties were prepared.

Finally, a study on the magnetorheological fluid was carried out with the force interrupter. In order to improve the sedimentation stability of the MRF, a magnetic material coated carbon nanotubes was synthesized and succeeded in obtaining high sedimentation stability.

Keywords: Composites, electromagnetic shielding, X-ray shielding, gamma-ray shielding, interfacial adhesion, fracture mechanism, multilayered structure, magnetorheological fluid

Student Number: 2013-30935

Contents

Abstract	i
Contents	iv
List of Tables	viii
List of Figures	x
Chapter 1. Introduction	1
1. 1. Composite Materials	1
1. 2. Fundamentals of Shielding.....	7
1. 2. 1. Radiation Shielding	7
1. 2. 2. EMI Shielding	17
1. 2. 3. Gas Barrier Properties	23
1. 3. Magnetorheological Fluids	24
1. 4. Research Objectives	27
References	29
Chapter 2. Radiation Shielding Properties of Nonlead Metal/Polymer Composites	31
2. 1. Introduction	31
2. 2. Experimental Section	34
2. 2. 1. Materials.....	34

2. 2. 2. Sample Preparation	35
2. 2. 3. X-Ray Irradiation and Analysis.....	36
2. 2. 4. γ -ray Irradiation and Analysis	38
2. 3. Results and Discussion.....	41
2. 3. 1. The effect of metal fillers on X-Ray shielding.....	41
2. 3. 3. γ -Ray Shielding Properties.....	50
2. 4. Conclusions	65
References	67

Chapter 3. Microwave Absorption and Shielding Property of Fe-Si-Al Alloy/MWCNT/Polymer Nanocomposites	72
3. 1. Introduction	72
3. 2. Experimental Section	74
3. 2. 1. Materials.....	74
3. 2. 2. Preparation of Sendust/Polymer Composites.....	75
3. 2. 3. Fabrication of Sendust/MWCNT/Polymer Composites.....	75
3. 2. 4. Characterization	76
3. 3. Results and Discussion.....	79
3. 3. 1. Morphology of Sendust/MWCNT/polymer composites	79
3. 3. 2. Dielectric Properties.....	79
3. 3. 3. Microwave Absorption and EMI Shielding Properties	83
3. 4. Conclusions	93

References	94
------------------	----

Chapter 4. Enhancement of Interfacial Adhesion between Polymer Pairs and Fracture Mechanism.... 99

4. 1. Introduction	99
4. 2. Experimental Section	101
4. 2. 1. Materials.....	101
4. 2. 2. Ion beam irradiation and plasma treatment	102
4. 2. 3. Adhesion Process	103
4. 2. 4. Measurement of Fracture Toughness	103
4. 2. 5. Characterization	105
4. 2. 6. Lamination with Aluminum film and barrier properties	105
4. 3. Results and Discussion.....	111
4. 3. 1. Adhesion Strength with Bonding Time and Temperature	111
4. 3. 2. Fracture Mechanism.....	120
4. 3. 3. Barrier properties of laminates film	132
4. 4. Conclusions	136
References	137

Chapter 5. MR Fluid High-Performance Magnetorheological Suspensions of Magnetic Particle-deposited Carbon Nanotubes with Enhanced Stability 141

5. 1. Introduction	141
5. 2. Experimental Section	143
5. 2. 1. Functionalization of CNTs	143
5. 2. 2. Synthesis of CNT-Fe ₃ O ₄ particles	143
5. 2. 3. Synthesis of CNT-FeCo particles	144
5. 2. 4. Characterization	145
5. 3. Results and Discussion	146
5. 3. 1. Morphology & Structure	146
5. 3. 2. Magnetorheological behaviors	146
5. 3. 3. Suspension stability	150
5. 4. Conclusion	151
References	160
Chapter 6. Conclusions	164
6. 1. Overall Conclusions	164
6. 2. Further Works	167
국문 초록	169
List of Publication	172
Appendix	174
Appendix A. Improvement of Mechanical Properties by Introducing Curable Functional Monomers in Stereolithography 3D Printing	174

List of Tables

Table 1. 1. Classification of ionizing radiation.....	12
Table 2. 1. Dose ratios, attenuation coefficients, and mass attenuation coefficients of various composites containing 400 phr metal particles with a thickness of 1mm.....	48
Table 2. 2. Dose ratios for BiSnP multilayered sheets and laminates with either a BiSnP 400 phr composite film or a WP 400 phr composite film.....	49
Table 2. 3. γ -ray shielding efficiency of the BiSn alloy/polymer composite.....	61
Table 2. 4. Calculated shielding efficiency of multistacked (1mm thick BiSn/polymer + 1mm thick tungsten plate) sheet.....	62
Table 2. 5. Calculated shielding efficiency of multistacked (1mm thick BiSn/polymer + 1mm thick tungsten plate) sheet.....	63
Table 2. 6. Calculated shielding efficiency of multistacked (1mm thick BiSn/polymer + 1mm thick tungsten plate) sheet.....	64
Table 3. 1. Power Loss, Density, and Specific Power Loss of Magnetic, Dielectric, and Hybrid Composites.....	92
Table 4. 1. Various properties of polymeric materials.....	107
Table 4. 2. Elemental compositions of fractured PS and PA6 surfaces measured by XPS (variation of annealing time).....	127
Table 4. 3. Elemental compositions of fractured PS and PA6 surfaces measured by XPS (variation of annealing temperature).....	128
Table 4. 4. Diffusion Coefficients for d-PS, Interfacial Thickness and Reptation	

Time.....	131
Table 4. 5. Water vapor transmission rate (WVTR) of different samples.....	134
Table 5. 1. The densities of CNT, Fe ₃ O ₄ , CNT/Fe ₃ O ₄	152
Table 5. 2. Static yield stress and dynamic yield stress of the suspensions.....	152
Table 5 .3. Static yield stress and dynamic yield stress of the suspensions of CNT/FeCo suspension.....	152

List of Figures

Figure 1. 1. Classification of composites according to the matrix materials.....	5
Figure 1. 2. Classification of composites according to the reinforcements.....	6
Figure 1. 3. Illustration of the relative abilities of four different types of radiation to penetrate solid matter.....	13
Figure 1. 4. Illustration of K-shell X-ray emission by photoelectric effect.....	14
Figure 1. 5. Illustration of Compton scattering.....	15
Figure 1. 6. Schematic diagram of attenuation of X-ray passing through a thin sheet of width dx	16
Figure 1. 7. Charge distribution on a spherical conducting shell.....	21
Figure 1. 8. A spherical magnet shell with good permeability will reduce the field strength.....	21
Figure 1. 9. A thin metallic shell with good conductivity will reduce an alternating magnetic field strength.....	22
Figure 1. 10. Graphical representation of EMI shielding.....	22
Figure 2. 1. Schematic illustration of X-ray irradiation apparatus.....	39
Figure 2. 2. Schematic figure of the experimental set-up for determining incident and transmitted intensities of gamma rays.....	40
Figure 2. 3. (a) Dose ratios (the ratio of the number of transmitted photons to the total number of incident photons) of X-rays through the three composites (BiSn, Sn and tungsten particles) with a thickness of 1mm, containing 400phr metal	

particles. (b) The linear attenuation coefficients and mass attenuation coefficients of the three composites..... 45

Figure 2. 4. SEM photographs: (a) virgin gauze, (b) the surface of a 10-layer laminated sheet, (c) a cross sectional view of a fractured surface of (b); fractured surfaces of 10-layer sheets pressed at 135 °C (d), 139 °C (e), and at 160 °C (f). Some of the BiSn particles melt at the pressing temperature. (g) Photograph of a cross-section of a BiSnP stacked sheet attached to a 0.4mm WP composite film. Some melted BiSn particles are smeared inside the stacked sheet..... 46

Figure 2. 5. (a) 3D plot of the dose ratio for the BiSnP-impregnated multiple sheets (10), (b) 2D plot of (a), (c) 3D plot of the dose ratio for the BiSnP-impregnated multiple sheets (10) with a 0.4mm WP film, (d) 3D plot of the dose ratio for BiSnP-impregnated multiple sheets (10) with a 0.4mm BiSnP film. The films and stacked sheets were pressed together to ensure good adhesion..... 47

Figure 2. 6. (a) The extrudate of BiSn/polymer, (b) SEM photograph of the fractured sectional view (scale bar is 200µm), (c) Bent BiSn/polymer sheet.... 56

Figure 2. 7. γ -ray transmittance through the BiSn/polymer composite sheet. The line is a fitting of the data using the Beer-Lambert law, $I/I_0 = \exp(-0.0308 * x)$, with a correlation of 0.9995..... 57

Figure 2. 8. γ -ray transmittance through the tungsten sheet. The line is a fitting of the data using the Beer-Lambert law, $I/I_0 = \exp(-0.23282 * x)$ with a correlation of 0.994. 58

Figure 2. 9. γ -ray transmittance through the (BiSn alloy/polymer composite sheet (10mm) + tungsten sheet). The line is the calculated values using the measurement values of each sheet..... 59

Figure 2. 10. Schematic figure of the multistacked sheet of (BiSn/polymer sheet +

tungsten sheet) (a) normal view, (b) flexible bent multilayered sheet, (c) sectional view, (d) photograph of a single layer of BiSn/polymer sheet + tungsten sheet.....	60
Figure 3. 1. SEM photographs of (a) bulk Sendust (x100 magnification) and (b) micro-forged Sendust (x100 magnification).....	81
Figure 3. 2. SEM photographs of (a) fractured surface of the composite after roll milling (x500 magnification) and (b) x10000 magnification.....	82
Figure 3. 3. Complex permeability of Sendust/MWCNT/polymer composites: (a) real permeability and (b) imaginary permeability.....	88
Figure 3. 4. Complex permittivity of Sendust/MWCNT/polymer composites: (a) real permittivity and (b) imaginary permittivity.....	89
Figure 3. 5. Electromagnetic absorption performance of Sendust/MWCNT/polymer composites: (a) reflection loss and (b) power loss.....	90
Figure 3. 6. EMI shielding effectiveness (SE) of the Sendust/MWCNT/polymer composites.....	91
Figure 4. 1. Schematic illustration of asymmetric double cantilever beam (ADCB) test.....	108
Figure 4. 2. Schematic representations of structures and reaction between PSMA and PA6.....	109
Figure 4. 3. Schematic illustrations of experiments.....	110
Figure 4. 4. Variation of the fracture toughness of PS(+PSMA)/PA6 interface with the annealing time.....	115
Figure 4. 5. Variation of the fracture toughness of PS(+PSMA)/Ny6 interface with the annealing temperature.....	116

Figure 4. 6. Variation of the fracture toughness between modified PS by ion beam irradiation under reactive oxygen gas and PA6 with (a) bonding temperature and (b) bonding time.....	115
Figure 4. 7. Variation of the fracture toughness between modified PS by oxygen plasma treatment and PA6 with bonding temperature (a), and bonding time (b)	117
Figure 4. 8. Variation of the fracture toughness between modified PS by plasma treatment after ion beam irradiation without reactive gas and PA6 with bonding temperature (a), and bonding time (b).....	118
Figure 4. 9. Schematic representation of the locus of failure of PS-(+PSMA)/Ny6 interface.....	126
Figure 4. 10. Depth profiles: (a) nonannealed, (b) annealed at 120 °C for 30 min, (c) annealed at 120 °C for 90 min, (d) annealed at 120 °C for 300 min, (e) annealed at 120 °C for 900 min, (f) annealed at 150 °C for 30 min, and (g) annealed at 150 °C for 900 min; (h) calculation of the diffusion coefficient and experimental measurement (annealed at 120 °C for 90min).....	127
Figure 4. 11. Double-logarithmic plot of interfacial thickness versus annealing time for the (h-PS/d-PS) bilayer annealed at 393 K (120 °C). The slope of 1/2 is drawn in the context of the Fickian diffusion as a guide.....	129
Figure 4. 12. Schematic representation of the variation of the interfacial reactions with the reaction time: (a) early period, (b) later period.....	130
Figure 4. 13. Cross-section of the laminates of Al film and clay/MXD6.....	135
Figure 5. 1. SEM photographs of (a, b) CNT/Fe ₃ O ₄ , and (c) TEM images of	

CNT/Fe ₃ O ₄ particles.....	153
Figure 5. 2. SEM photograph of (a) CNT/FeCo and (b, c) TEM images of CNT/FeCo particles.....	153
Figure 5. 3. X-ray diffraction patterns of CNT, FeCo, and CNT/FeCo.....	154
Figure 5. 4. (a) TGA measurement data and (b) VSM data of CNT, CNT/Fe ₃ O ₄	155
Figure 5. 5. Optical microscope images of CNT/Fe ₃ O ₄ suspension (a) before and (b) after the application of the external magnetic field.....	156
Figure 5. 6. (a) Amplitude-sweep dependence of the storage modulus, G', and loss modulus, G''. (b) Frequency dependence of G', G''	157
Figure 5. 7. (a) Shear stress and (b) shear viscosity flow curves for 10 vol% CNT/Fe ₃ O ₄ suspension.....	157
Figure 5. 8. (a) Amplitude-sweep dependence of the storage modulus, G', and loss modulus, G''. (b) Frequency dependence of G', G'' of CNT/FeCo particles..	158
Figure 5. 9. (a) Shear stress flow curve of CNT/FeCo suspension and (b) storage modulus comparison between CNT/Fe ₃ O ₄ and CNT/FeCo suspensions.....	158
Figure 5. 10. (a) Static yield stress curve and (b) Dynamic yield stress -dependence on the magnetic field strength.....	159
Figure 5. 11. The light transmission [%] as function of time [h] for CNT and CNT/Fe ₃ O ₄ suspensions (10 vol%).....	160

Chapter 1. Introduction

1. 1. Composite Materials

Composite materials are multiphase materials obtained through the artificial combination of different materials in order to attain properties that the individual components by themselves cannot attain. An example is a lightweight structural composite that is obtained by embedding continuous strong fiber in one or more orientation in a polymer matrix. Moreover, we can find composite materials (composites) from the ancient age. The earliest human-made composite materials were concrete. Concrete is a structural composite obtained by combining cement, sand, gravel, and optionally other ingredients that are known as admixture [1]

Composite materials can be tailored for various properties by appropriately choosing their components, their proportions, their distributions, their morphologies, their degrees of crystallinity, their crystallographic textures, as well as the structure and composition of the interface between components. Due to this strong tailorability, composite materials can be designed to satisfy the needs of technologies relating to the aerospace, automobile, electronics, construction, energy, biomedical and other industries. As a result, composite materials constitute most commercial engineering materials.

In many cases, a strong and stiff component is present, often in elongated form, embedded in a softer constituent forming the matrix. In general, composites are

classified according to their matrix material. The main classes of composites are polymer-matrix, cement-matrix, metal-matrix, carbon-matrix and ceramic-matrix composites. [2]

1) Polymer matrix composites (PMCs)

PMCs are the most developed class of composite materials in that they have found widespread application, can be fabricated into large, complex shapes, and have been accepted in a variety of aerospace and commercial applications. They are constructed of components such as carbon or boron fibers bound together by an organic polymer matrix. These reinforced plastics are a synergistic combination of high-performance fibers and matrices.

2) Metal matrix composites (MMCs)

MMCs consist of metal alloys reinforced with continuous fibers, whiskers (a version of short fibers that are in the form of single crystals), or particulates (fine particles, as distinct from fibers). Because of their use of metals as matrix materials, they have a higher temperature resistance than PMCs but in general are heavier. They are not as widely used as PMCs but are finding increasing applications in many areas. Further development of manufacturing and processing techniques are essential to bringing down product costs and accelerating the use of MMCs.

3) Ceramic matrix composites (CMCs)

Monolithic ceramic materials have a natural high-temperature resistance but also have fundamental limitations in structural applications owing to their propensity for brittle fracture. The incorporation of a reinforcement, for example, ceramic fiber reinforcement, into the ceramic matrix can improve the forgivability of the material by allowing cracking to be retarded by the fiber-matrix interfaces. CMCs are a class of structural materials with reinforcements such as SiC fibers embedded in a ceramic matrix. The reinforcements can be continuous fibers, chopped fibers, small discontinuous whisker platelets, or particulates. They have the potential for high-temperature application.

4) Carbon-carbon composites (CCCs)

CCCs consist of carbon fiber reinforcement embedded in a carbonaceous matrix. Preliminary processing is very much like that for PMCs, but the organic matrix is subsequently heated up to the point where it is converted to carbon. Carbon-carbon is a superior structural material for applications where resistance to very high temperatures and thermal shock is required. No other material has higher specific strength properties (strength-to-density ratio). Oxidation protection systems, low-cost manufacturing, and scale-up of C/C structures are needed to effect more widespread use and subsequent flow-down to industrial applications.

Figure 1.2 represents a classification scheme for composites according to the

reinforcements [2]. The geometry of the reinforcing phase is one of the major parameters in determining the effectiveness of the reinforcements; in other words, the properties of composites are a function of the shape and dimensions of the reinforcement. We usually describe the reinforcement as being either fiber or particulate.

Particulate reinforcements have dimensions that are approximately equal in all directions. The shape of the reinforcing particles may be spherical, cubic, platelet or any regular or irregular geometry. The arrangement of the particulate reinforcement may be random or with a preferred orientation, and these characteristics is also used as a part of the classification scheme. A fibrous reinforcement is characterized by its length being much greater than its cross-sectional dimension. However, the ratio of length to the diameter, known as the aspect ratio, can vary considerably. In single-layered composites long fibers with high aspect ratios give what are called continuous fiber reinforced composites, whereas discontinuous fiber composites are fabricated using short fibers of low aspect ratio.

Multilayered composites are another category of fiber reinforced composite. These are classified either laminates or hybrids. Laminates are sheet constructions which are made by stacking layers in a specified sequence. Hybrids are usually multilayered composites with mixed fibers and are becoming commonplace. The fibers may be mixed in a ply or layer by layer and these composites are designed to benefit from the different properties of the fibers employed.

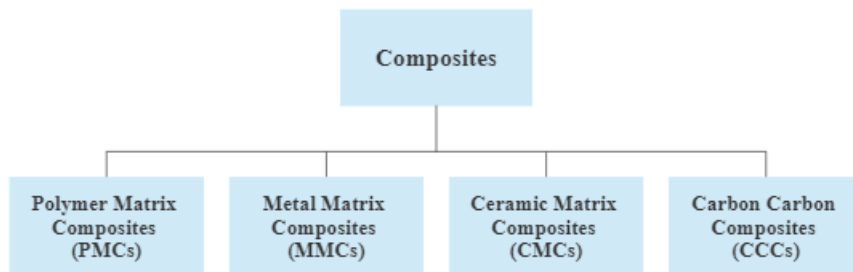


Figure 1. 1. Classification of composites according to the matrix materials. [2]

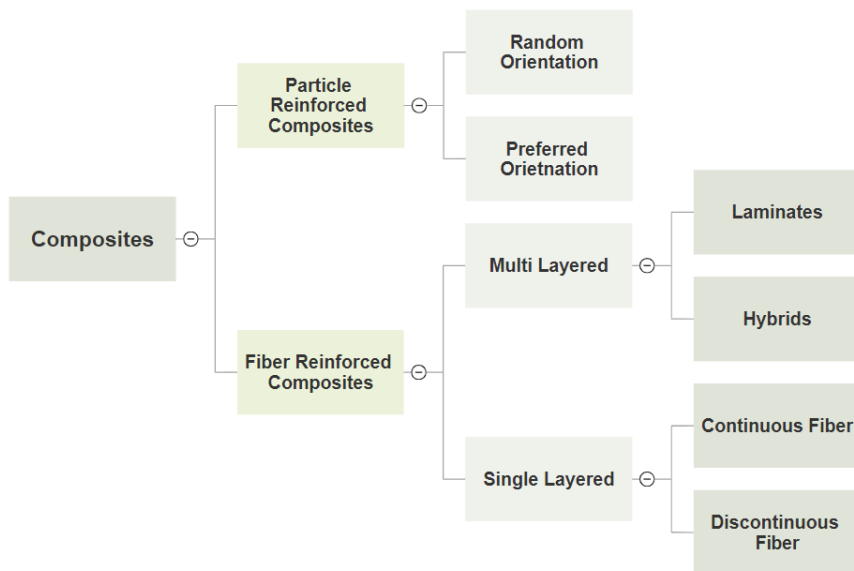


Figure 1. 2. Classification of composites according to the reinforcements. [2]

1. 2. Fundamentals of Shielding

1. 2. 1. Radiation Shielding

The definition of ionizing radiation is all the particles capable of producing ion, i.e., alpha particles, beta particles, gamma rays, X-rays, neutrons, fast electrons, high-speed protons, and other atomic particles [3]. Based upon electrical charge and mass size, the radiation can be classified into two categories, charged particles and neutral particles as shown in Table 1.1. All the radiations are produced by interactions with atomic orbital electron, acceleration of charged particle, nuclear reactions such as scattering and absorption, and spontaneous radiative nuclear transformation.

Some types of radiation such as alpha particles, beta particles and neutrons can be completely absorbed, whereas others, i.e., x-rays and gamma-rays can only be reduced to safe levels [4]. As shown in Figure 1.3, the principle and means of radiation shielding depend on the types of radiation. Heavy particles such as alpha particles are more dangerous than light particles when it reacts with human body. However, the charged particles are easy to be absorbed into matter such as a paper sheet or a thin aluminum foil. Even if they don't encounter such blockages, the charged particles cannot go forward even a short distance in atmosphere. For the neutron, however, it is difficult to shield because it has no charges and doesn't react with any materials electrically. Therefore, they have to be decelerated by the perfect elastic collisions with hydrogens having the same mass with them first, then they can

be absorbed by materials having the large cross-section, such as boron atoms.

X-rays and gamma-rays are called electromagnetic radiations because they are composed of photons of no mass and charge. Although the two radiation can be categorized by their origins, atomic and nuclear transition each, their wave-like properties are the same with each other. Therefore, the same attenuation mechanisms are applied.

In the energy range of most medical and industrial radiation applications, i.e., nominally less than 20 MeV, interactions of photons with matter are mainly via three processes, (i) photoelectric absorption; (ii) Compton scattering; (iii) pair production [4]. Among them, the main reactions of X-ray in diagnostic energy range with matter are photoelectric effect and Compton scattering.

As shown in Figure 2.4, with a photoelectric interaction, the photon transfers all of its energy to a bound electron and the kinetic energy of the electron is given by Einstein's photoelectric equation

$$T_{\max} = h\nu - \phi \quad (1. 1)$$

Where $h\nu$ is the initial photon energy, ϕ is the electron binding energy (work function) and $T_{\max} = mv^2/2$ is the maximum kinetic energy of the ejected electron. The atom is left in an excited state and will emit characteristic radiation and Auger electrons in its transition back to the ground state. The energy deposited in a photoelectric event in tissue can be assumed to be absorbed at the point of photon interaction [5].

In Compton scattering, the incoming photon is deflected through an angle θ with respect to its original direction. The photon transfers a portion of its energy to the

election, which is then known as a recoil electron. Because all angles of scattering are possible, the energy transferred to the electron can vary from zero to a large fraction of the photon energy [6]. Based on the scattering theory of photons by electrons, it is usually a satisfactory approximation to consider the electrons as free particles. If scattering is considered as in Figure., the kinetic energy T for the recoil electron and the scattering angle ϕ of the electron derived from the conservation of energy and momentum are given as follows [5].

$$T = hv \frac{\alpha(1-\cos \theta)}{1+\alpha(1-\cos \theta)} \quad (1.2)$$

$$\cos \phi = (1 + \alpha) \tan \frac{1}{2} \theta \quad (1.3)$$

The attenuation of energy by such processes depends on the bond energy of electrons orbiting the nucleus. As the Z number increases and the distance of electrons from the nucleus decrease, the incident photon gives off more energy than others reacting with materials having the lower Z number (atomic number) and electrons orbiting farther from the nucleus. And the dense inside of the shielding material makes the photons interact more easily with the electrons in shielding material. Therefore, the Z number of element and density of matter are dominant factors for shielding electromagnetic radiations.

Incident photons lose part of their energy as they pass through the shielding materials. The penetration of photons in matter is governed by the statistical probability per unit distance of travel in which photons interact with matter by one physical process or another. This probability, denoted by μ , is called the linear attenuation coefficient and has the dimension of inverse length, e.g., cm^{-1} . The larger the attenuation coefficient is, the better the shielding ability is. For this reason, the

attenuation coefficient is a reliable measure to estimate shielding ability for any matter.

As shown in illustration of Figure 1.6, photons passing through a small thickness dx will be absorbed partially. Letting the number of incident photons as I , the number of photons absorbed by the thin part, dI , is proportional to I and dx as follows.

$$-dI = \sigma N I dx \quad (1.4)$$

the absorption cross section, σ , perpendicular to the path of photon, represents the attenuation by individual atoms in the part. Defining N as the concentration of particles in the part, the multiplied value of the two constants, σN , can be regarded as a quantity indicating the shielding ability of the part in material. With an initial condition, $I=I_0$, setting σN as a constant μ , an equation of the inverse exponential power law called Beer-Lambert law is obtained as below.

$$\frac{I}{I_0} = \exp(-\mu x) \quad (1.5)$$

the linear attenuation coefficient, μ , depends on what kinds of materials are used for shielding and how mech energy and how many photons are incident. Sometimes the linear attenuation coefficient is given by mass attenuation coefficient, μ/ρ , linear attenuation coefficient divided by the density of matter. The linear attenuation coefficient is an appropriate measure to evaluate the overall ability to block the electromagnetic radiations, whereas the mass attenuation coefficient is useful to separate the effect of density from other factors.

Each of the atoms has the characteristic mass attenuation coefficient values at the several electron shells because almost every electron exists at the determined orbits. About 80 % of energy lose by photoelectric effect occurs at the K-shell of atom in

shielding material as the electrons have larger bond energy than the electrons at the outer shells. The peak at the highest photon energy is called K-edge, and with decreasing photon energy, each peak is called in the order of binding energy of electron shells, i.e., L-shell, M-shell, etc. Among equally dense materials, K-edge is the most important peak as it determines the shielding ability of matter in the diagnostic energy range of X-ray.

Table 1. 1. Classification of ionizing radiations

Charged particles	Beta particles	Electron, Positron
	Heavy charged particles	Muon, Pion, Proton, Deuteron, Triton, Helium-3, Alpha,
Neutral Particles	Photons	X-ray, Gamma-ray
	Neutrons	Fast neutron, Thermal neutron

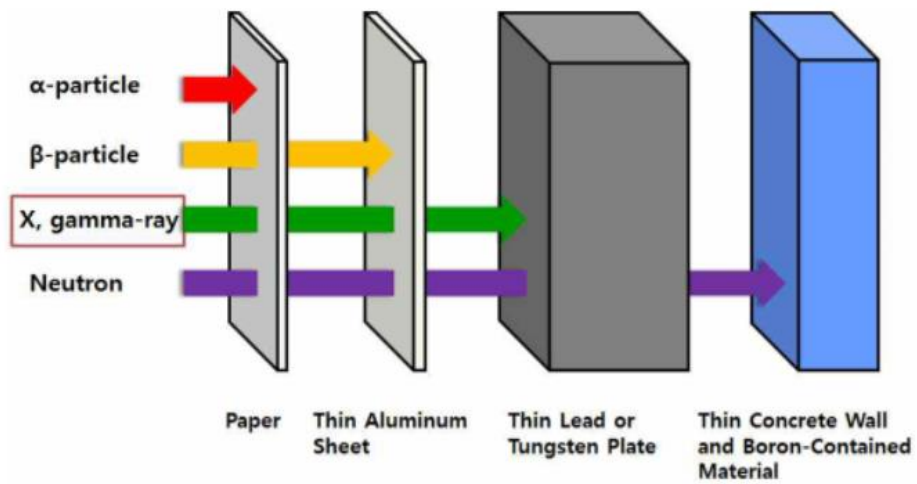


Figure 1. 3. Illustration of the relative abilities of four different types of radiation to penetrate solid matter.

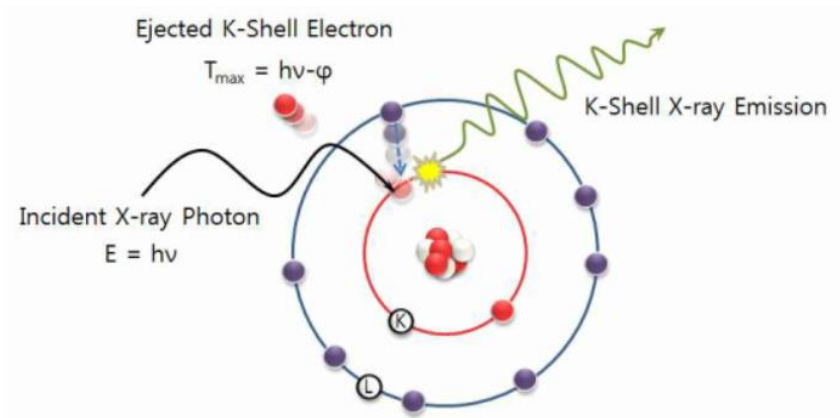


Figure 1. 4. Illustration of K-shell X-ray emission by photoelectric effect.

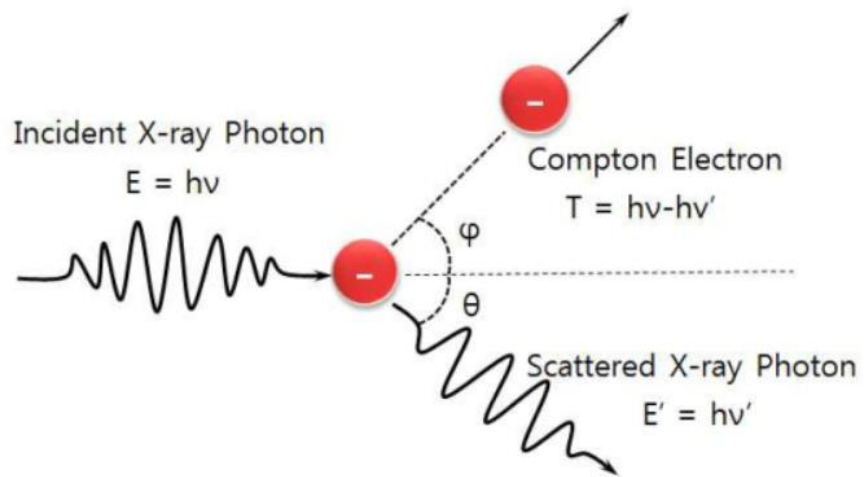


Figure 1. 5. Illustration of Compton scattering.

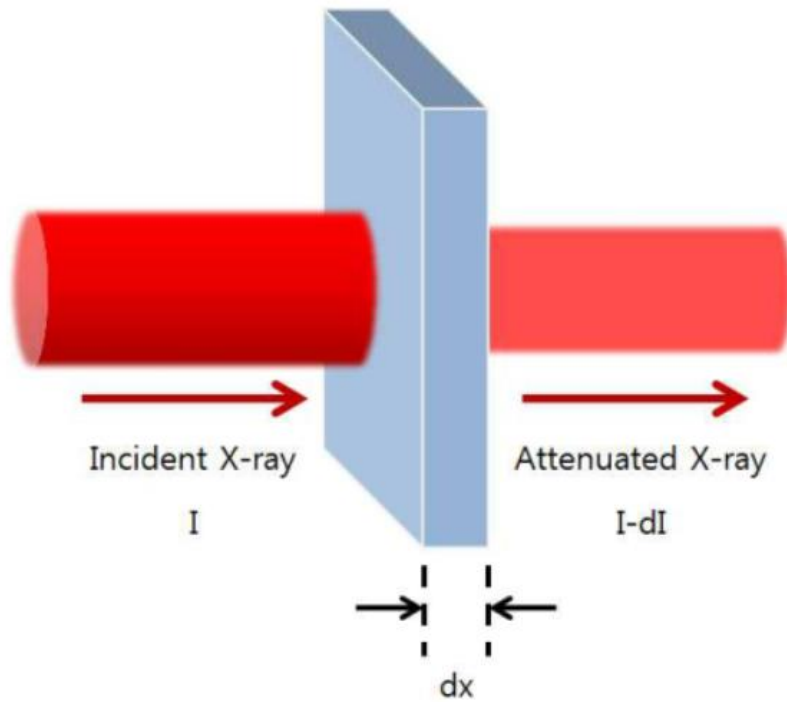


Figure 1. 6. Schematic diagram of attenuation of X-ray passing through a thin sheet of width dx .

1. 2. 2. EMI Shielding

EMI Shielding means to use a shield (a shaped conducting material) to partially or completely envelop an electronic circuit, that is, an EMI emitter or susceptor. Therefore, it limits the amount of EMI radiation from the external environment that can penetrate the circuit and, conversely, it influences how much EMI energy generated by the circuit can escape into the external environment. A variety of materials have been used for shielding with a wide range of electrical conductivity, magnetic permeability, and geometries. Shields invariably contain apertures or openings used for access and ventilation, as well as a number of joints and seams for practical manufacturing. Shields for practical equipment also allow attachment to wire or pipes used for signaling and services. All these components constitute breaches of the shield integrity and play a decisive part in the overall performance of the shield [7].

Shielding effect is provided by a conductive barrier or enclosure that harmlessly reflects or transmits EMI into the ground. In 1821, Michael Faraday first introduced the concept that an enclosed conductive housing has a zero electrical field. This principle is known as Faraday cage, which forms the basis of today's shielding technology. If sensitive equipment is enclosed within a thin, conductive, spherical shell that is placed in an E-field, as shown in Figure 1.7, it will be shielded because the current setup by the electromagnetic wave is not conducted into the inside of the shell. This is not because the shell has completely absorbed the field, but because the E-field has caused electronic charges of different polarity along the shell. These

charges will, in turn, generate an electrical field that will tend to cancel the original field inside the shell [8,9].

When it comes to H-fields, Faraday's effect will disappear. However, the H-field shielding can be achieved by means of shields made of a soft magnetic material with high permeability, $\mu \gg 1$, and sufficient thickness to attenuate the magnetic field in the shielding shell by providing a low reluctance, as illustrated in Figure 1.8. That is, the spherical shell of magnetic material with good permeability will reduce the H-field intensity inside because the H-field tends to remain in the magnetic material layer as the magnetic material offers a low-reluctance path [8,10]. Alternatively, a thin shield made of a conductive material with low permeability can also provide effective shielding for H-fields at high frequencies. This is because an alternating H-field will induce eddy currents in the shielding screen, assuming that the shield has adequate conductivity, as shown in Figure 1.9. These eddy currents will themselves create an alternating H-field of the opposite orientation inside the shell. The effect will increase as the frequency increases, resulting in high shielding effectiveness at high frequencies [8]. Therefore, it is relatively difficult to shield against low-frequency H-fields. Whereas magnetic absorption shielding typically needs the installation of thick shields constructed of fairly expensive magnetic materials, conductive shields based on the induced current principle maybe reasonably effective at powerline frequencies.

Shielding can be specified in the terms of reduction in magnetic (and electric) field or plane-wave strength caused by shielding. The effectiveness of a shield and its resulting EMI attenuation are based on the frequency, the distance of the shield from

the source, the thickness of the shield, and the shield material. Shielding effectiveness (SE) is normally expressed in decibels (dB) as a function of the logarithm of the ratio of the incident and exit electric (E), magnetic (H), or plane-wave field intensities (F): $SE \text{ (dB)} = 20 \log (E_0/E_1)$, $SE \text{ (dB)} = 20 \log (H_0/H_1)$, or $SE \text{ (dB)} = 20 \log (F_0/F_1)$, respectively. With any kind of electromagnetic interference, there are three mechanisms contributing to the effectiveness of a shield. Part of the incident radiation is reflected from the front surface of the shield, part is absorbed within the shield material, and part is reflected from the shield rear surface to the front where it can aide or hinder the effectiveness of the shield depending on its phase relationship with the incident wave, as shown in Figure 1.10. Therefore, the total shielding effectiveness of a shielding material (SE) equals the sum of the absorption factor (A), the reflection factor (R), and the correction factor to account for multiple reflections in thin shields:

$$SE = R + A + B \quad (1.6)$$

All the terms in Equation 1.6 are expressed in dB. The multiple reflection factor B can be neglected if the absorption loss A is greater than 10 dB. In practical calculation, B can also be neglected for electric fields and plane waves.

1) Absorption Loss

Absorption losses A are a function of the physical characteristics of the shield and are independent of the type of source field. Therefore, the absorption term A is the same for all three waves. When an electronic wave passed through a medium such as a shield, its amplitude decreased exponentially, as shown in Figure 1.11. This

decay or absorption loss occurs because currents induced in the medium produce ohmic losses and heating of the material, and E_1 and H_1 can be expressed as $E_1 = E_0 e^{-t/\delta}$ and $H_1 = H_0 e^{-t/\delta}$. The distance required for the wave to be attenuated to $1/e$ or 37% is defined as the skin depth, d . Therefore, the absorption term A is given by the expression

$$A = 20 \left(\frac{t}{\delta} \right) \log e = 8.69 \left(\frac{t}{\delta} \right) = 131t\sqrt{f\mu\sigma} \quad (1.7)$$

where A is the absorption or penetration loss expressed in decibels, t is the thickness of the shield, f is frequency, μ is relative permeability, σ is conductivity.

2) Reflection Loss

The reflection loss is related to the relative mismatch between the incident wave and the surface impedance of the shield. The computation of reflection losses can be greatly simplified by considering shielding effectiveness for incident electric fields as a separate problem for that of electric, magnetic, or plane waves. The equations for the three principle fields are given by the expression [11]

$$R_E = 321.8 + 10 \log \frac{\sigma}{f^3 r^2 \mu} \quad (1.8)$$

$$R_H = 14.6 + 10 \log \frac{f r^2 \sigma}{\mu} \quad (1.9)$$

$$R_P = 168 - 10 \log \frac{f \mu}{\sigma} \quad (1.10)$$

where R_E , R_H , and R_P are the reflection losses for the electric, magnetic, and plane wave fields, respectively expressed in dB, σ is the relative conductivity, f is the frequency, μ is the relative permeability referred and r is the distance from the source to the shielding in m.

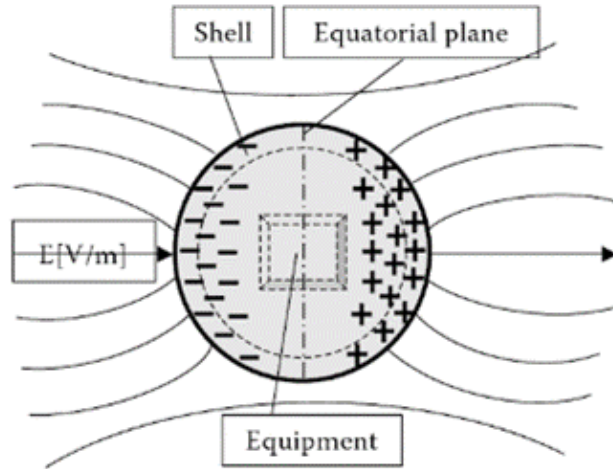


Figure 1. 7. Charge distribution on a spherical conducting shell

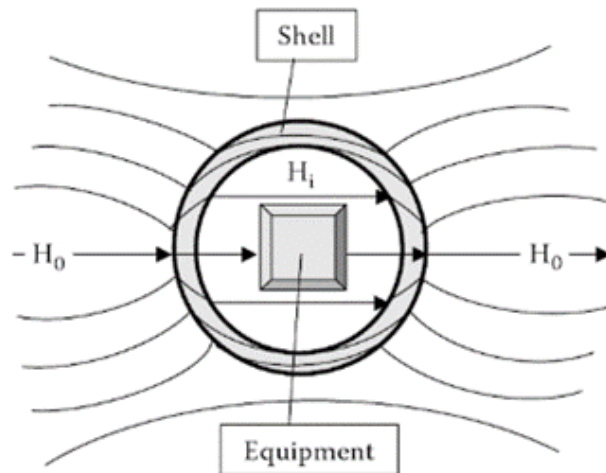


Figure 1. 8. A spherical magnet shell with good permeability will reduce the field strength

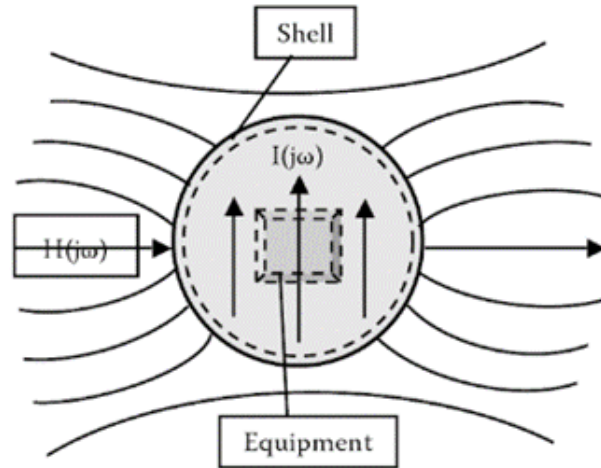


Figure 1. 9. A thin metallic shell with good conductivity will reduce an alternating magnetic field strength

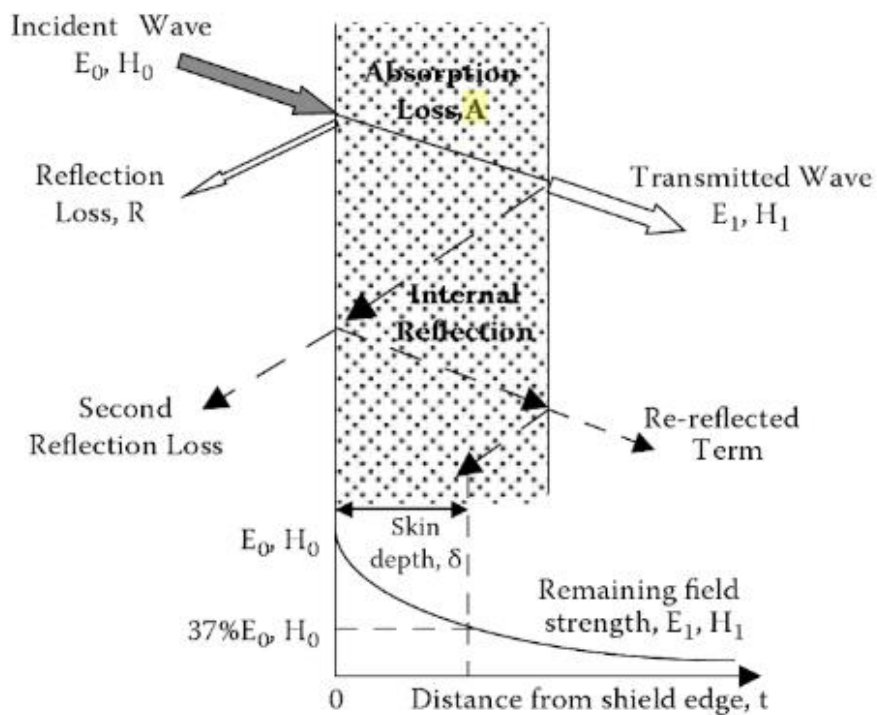


Figure 1. 10. Graphical representation of EMI shielding

1. 2. 3. Gas Barrier Properties

Materials with high barrier properties are widely demanded as package materials of foods, medicine and medical supplies, or industrial supplies. For such materials polymers have suitable features such as ease of process, excellent flexibility, transparency, and low cost. These characteristics are also important for next-generation organic light emitting diode displays since flexible materials should be used as substrates and encapsulates of flexible OLED displays instead of currently used rigid materials such as glass.

However, oxygen permeability of commonly used polymers such as polyethylene (PE) or poly (ethylene terephthalate) (PET) is much higher than that of inorganic materials such as aluminum or silicon oxide. Numerous studies have been conducted to improve barrier properties of such polymers.

Composites containing impermeable agents have different diffusion properties compared with pure materials. Permeants have to detour the impermeable sections and diffusivity decreases owing to tortuous diffusion paths. In the simple two-dimensional model, the filler act as impermeable barriers to the migration of gas molecules. The equation for the model is

$$P_c / P_u = V_{fp} / [1 + (L/2W) V_{fc}] \quad (1. 11)$$

were P_c is the gas permeability of the nanocomposites, P_u is the gas permeability of the pure polymer, V_{fp} is volume fraction of the polymer in the nanocomposites, V_{fc} is the volume fraction of the clay nanoparticles, L is the longest dimension of the filler, and W is the smallest dimension of the filler.

In this model the interaction between the filler and polymer is assumed to be minimal and the fillers are in a perfectly tiled arrangement parallel to the surface of the polymer film. The $L/2W$ term for aspect ratio is derived from the assumption that the morphology of the filler's cross-section is a rectangle.

However, some nanocomposites that exhibit relative gas permeabilities exceed the performance predicted by the tortuous path model. This behavior would indicate that the nanoparticles have altered the fundamental behavior of the polymer. Bell et al. proposed that this effect was important in forming a constrained polymer region around the filler nanoparticles. This region is responsible for deviation from the tortuous path model. Since this was proposed as a conceptual model, the effect of change in the diffusion coefficient and the size of the constrained region were lumped into one correction factor applied to the numerator of the tortuous path equation.

1. 3. Magnetorheological Fluids

Magnetorheological (MR) fluids, which include suspensions of magnetically susceptible fine particles in a magnetically insulating fluid, are a type of smart material because the application of a magnetic field can transform the fluid from a suspension to a solid-like fibril structures in which the fibrils are aligned along the magnetic field direction due to the magnetic polarization among the suspended particles [12-19]. A reverse structural transition occurs as soon as the applied magnetic field is turned off. The structural changes are very fast, on the order of milliseconds. The aligned structural changes formed in response to a magnetic field

tune the rheological properties of the MR fluid over three to four orders of magnitude. The chain-like structure formed under the external magnetic field imparts the suspension with a yield stress as the fluid begins to flow. The rheological properties of those MR fluids can be fine-tuned by varying the magnetic field intensity for use in a variety of applications [13]. Therefore, MR fluids have aroused considerable interest over the last two decades, and their promising features have driven many scientific studies and industrial applications. MR fluid applications are found in automobile devices, such as linear dampers, rotor dampers, rotary brakes, as well as in various other industry products, e.g., directional control valves, hybrid actuators, and the haptic devices [14–16]. MR fluids have been used in medical applications, for example, in new cancer therapeutic procedures. MR fluids can inhibit the blood supply to a tumor or enable drug delivery systems [17]. As an advanced and intelligent polishing technology, MR finishing technology has been applied to various materials possessing various shapes that minimize their surface damages [18]. In the application of crude oil, MR fluid could reduce the shear viscosity of crude oil containing paraffin or asphaltene particles by altering their aggregation under the applied magnetic field [18]. On a larger scale, MR suspension systems are present in China's Dong Ting Lake Bridge to counteract vibrations caused by sudden gusts of wind. The same principle was used to stabilize buildings against earthquakes. More applications can be found in other report [19]

Although MR fluids and devices have made substantial progress in commercialization, the poor long-term stability of MR fluids can limit MR fluid utility in industrial applications. The long-term stability must be improved to avoid

sedimentation of the magnetic particles in MR suspensions due to a mismatch between the densities of the particles and the carrier liquid, the poor redispersibility of settled particles, and the magnetic particle's weak resistance to chemical degradation. Significant efforts have been made to overcome these crucial restriction factors, such as the introduction of polymer coatings or passivation layers onto the magnetic particles, the use of viscoplastic medium as a carrier liquid, the addition of additives, fillers, or surfactants, and the use of nonspherical or bidisperse particles in the MR suspension. A recent study showed that iron nanofiber-based MR fluids are promising to reduce or prevent sedimentation while providing good yield stress. Another common method for stabilizing heavy magnetic particles in a MR suspension is the addition of a thickener to the carrier liquid, which prevents the settling of particle. Unfortunately, these types of systems suffer from the trade-off between the high suspension stability and high resistance to suspension flow. An ideal MR fluid should have a low viscosity that facilitates flow in a device in the absence of an applied magnetic field and fast regeneration of the suspension. So far, the introduction of a light protective coating layer onto the magnetic particles seems to be the most promising for improving the stability of the suspension, because such coatings reduce the particle density, enhance the particle durability, improve the surface free energy of the magnetic particles, and yield superior compatibility (with a higher wettability) with the carrier liquid. Functional two-stage coatings have been shown to be more effective than monolayer coatings comprising a polymer or multiwalled carbon nanotubes. Apart from the approaches described above, effective strategies for reducing the densities of a polymer-coated particles have not yet been

fully developed. The main parameters that affect the rheological properties of MR fluids, such as the yield stress and apparent viscosity, are the volume fraction, size, type, and shape of the dispersed particles, physical properties of the carrier fluid, direction and intensity of the applied magnetic field, and mode of operation. Other parameters seem to be of lesser importance.

1. 4. Research Objectives

The functional properties were given by the filler selection of the composite materials. Among them, the barrier (blocking) properties is an important in various industrial field and daily life. The most common barrier elements are moisture, various gases, etc. Furthermore, the composites that block or shield various external irradiations such as electromagnetic waves and radiation have been developed and studied. There is a need for research on electromagnetic wave and radiation shielding.

The objectives of this research are to fabricate the polymer composites have shielding properties from electromagnetic waves and radiation and improve the shielding efficiency of the composites by novel approaching. Furthermore, enhancing the interfacial adhesion and understanding the adhesion mechanism are another research objective to fabricate the multi-stacked shielding composites. This study consists of three parts. One is radiation shielding composites, investigation the effect of the modification of fillers and multi-layered structure on their gamma-ray and X-ray shielding efficiency. Next, EMI shielding efficiency of the composites using the combination of different type filler, carbon nanotubes and Fe-Si-Al alloys

was investigated. Furthermore, understanding the EMI shielding phenomena by dielectric and magnetic materials and the mechanism of the synergetic effect was performed in this mixed system. Lastly, the investigation of the interfacial fracture phenomena between polymers interfaces. And the fracture mechanism was suggested to describe the change of fracture adhesion value plausibly. In addition, to confirm the suggested mechanism, mass spectroscopy experiment was performed.

Finally, the improvement of sedimentation stability in magnetorheological fluids is the one of the research objectives in this study. In addition, the effect of the modification of magnetic particles (iron-based particle) in MR fluid and the magnetorheological properties are also investigated by using several analyses.

References

- [1] Chung, D. D.; *Composite materials: science and engineering*; Springer, London, United Kingdom, 2010
- [2] Schwartz, M. M.; *Composite materials*; Princeton-Hall, New Jersey, U.S.A., 1997
- [3] Attix, H. F., *Introduction to Radiological Physics and Radiation Dosimetry*; Wiley-VCH, Weinheim, Germany, 1986
- [4] Hallenbeck, W. H.; *Radiation protection*; CRC Press, Florida, U.S.A., 1994
- [5] Butson, M. J.; Peter, K. N.; Cheung, T.; Metcalfe, P.; Radiochromic film for medical radiation dosimetry. *Mater. Sci. Eng. R Rep.*, **2003**, 41, 61-120.
- [6] Uhm, Y. R.; Kim, J.; Lee, S.; Jeon, J.; Rhee, C. K.; In situ fabrication of surface modified lead monoxide nanopowder and its HDPE nanocomposite. *Ind. Eng. Chem. Res.* **2011**, 50(8), 4478-4483.
- [7] Christopoulos, C.; *Principles and Techniques of Electromagnetic Compatibility*; CRC Press, Florida, U.S.A., 1995
- [8] Bjorklof, D.; Shielding for EMC. *Compliance Engineering.*, <http://www.cemag.com/99APG/Bjorklof137.html>, 1999
- [9] Bridges, J. E.; An update on the circuit approach to calculate shielding effectiveness. *IEEE Trans. Electromagn. Compat.*. **1998**, 30(3), 211-221.
- [10] Duffin, W. J.; *Advanced Electricity and Magnetism*; Mcgraw-Hill, London, United Kingdom, 1968
- [11] Ott, H., *Noise Reduction Techniques in Electronic Systems*, 2nd ed.; John Wiley & Sons., New York, U.S.A., 1988
- [12] Chuah, W. H.; Zhang, W. L.; Choi, H. J.; Seo, Y., Magnetorheology of core-shell structured carbonyl iron/polystyrene foam microparticles suspension with enhanced stability. *Macromolecules* **2015**, 48(19), 7311-7319.

- [13] Ghaffari, A.; Hashemabadi, S. H.; Ashtiani, M. A review on the simulation and modeling of magnetorheological fluids. *J. Intell. Mater. Syst. Struct.* **2015**, *26*, 881–904
- [14] Parlak, Z.; Engin, T., Time-dependent CFD and quasi-static analysis of magnetorheological fluid dampers with experimental validation. *Int. J. Mech. Sci.* **2015**, *64*, 22-31.
- [15] Farjoud, A.; Cavey, R.; Ahmadian, M.; Craft, M., Magneto-rheological fluid behavior in squeeze mode. *Smart Mat. Sci.* **2009**, *18*(9), 095001.
- [16] Yang, T. H.; Koo, J. H.; Kim, S. Y.; Kyung, K. U.; Kwon, D. S., Application of magnetorheological fluids for a miniature haptic button: Experimental evaluation. *J. Intell. Mater. Syst. Struct.* **2012**, *23*(9), 1025-1031.
- [17] Bica, I.; Liu, Y.; D.; Choi, H. J., Physical characteristics of magnetorheological suspensions and their applications. *J. Ind. Eng. Chem.* **2013**, *19*(2), 394-406.
- [18] Lee, J. W.; Hong, K. P.; Kwon, S. H.; Choi, H. J.; Cho, M. W., Suspension rheology and magnetorheological finishing characteristics of biopolymer-coated carbonyliron particles. *Ind. Eng. Chem. Res.* **2017**, *56*(9), 2416-2424.
- [19] López-López, M. T.; Kuzhir, P.; Bossis, G.; Mingalyov, P., Preparation of well-dispersed magnetorheological fluids and effect of dispersion on their magnetorheological properties. *Rheol. Acta* **2008**, *47*(7), 787-796.

Chapter 2. Radiation Shielding Properties of Nonlead Metal/Polymer Composites

2. 1. Introduction

In modern society, nuclear power is used effectively in various areas such as nuclear power plants, military equipment, medical and health care industry. Inadvertent exposure to high-energy electromagnetic wave radiation, such as X-rays or γ -rays from those industrial facilities, can be detrimental to human health since prolonged exposure or a high accumulated radiation dosage can lead to various health risks or symptoms, including carcinogenesis, cell mutations, organ failure and other acute radiation symptoms [1-7]. To attenuate or absorb the unwanted radiations, numerous researches have been conducted on a variety of shielding materials. Heavy metals mostly lead, or lead compounds have been used to protect the human body from such exposures [1-4]. Two critical factors for shielding electromagnetic radiations of X-rays or γ -rays are the Z -number (atomic number) and the density. In the nuclear industry, low Z -number materials alone are often unsuccessful in attenuating highly penetrative radiation such as γ -rays. Therefore, lead, the most commonly used shielding material, is superior to all other shielding materials due to its higher Z -number, density, and low cost [7-15]. Lead-based shielding materials, however, are detrimental to worker's health and cause environmental pollution

[9,10,14,15]. Although tungsten is the most effective and promising metal component to replace lead compounds, its specific gravity is higher than lead and its processing is quite difficult to apply for protective equipment or garment fabrication because of its high melting temperature. It is also not flexible enough to be used for radio protective clothing or gears.

In view of the lightness of the equipment and effectiveness for radiation protection, polymer-based composites are currently quite promising candidates, particularly nano- and micro-composites to attenuate/absorb high energy radiation [7,9]. Because of the large surface-to-volume ratio, they have a high potential to absorb high energy radiation and to be easily processed into a structured material with geometric conformability [11-13]. They are also lighter than their metal counterparts for use in effective and durable radiation protective gear applications [11]. However, the metal-polymer composites have problems of lower shielding ability due to pinholes which allow incident photons to penetrate pure polymer regions in the composite materials and no shielding ability of polymer matrix. The shielding ability of metal-polymer composites can be significantly enhanced if we can stop the penetrating photons with a densely packed structure. Hence, the properties of multilayered structures in metal-polymer composites such as metal particle dispersion, density, and laminations are crucial factors to decide the utility of those composites [11]. If the particles are uniformly dispersed in a polymer matrix, the layers of stacked particles would reduce voids for photons penetration and increase the probability of collision between photons and metal atoms [7,14]. Thus, the shielding ability of the metal-polymer

composite can be significantly improved to widen its use in various shielding applications.

Another element of high atomic number besides the tungsten which has attracted attention of researchers recently is the bismuth (Bi) [11,16-24]. Bismuth is the only non-radiating element in nature with a higher atomic number ($Z=83$) than lead. It is also harmless and non-toxic to the human body. Though its density is relatively high (8.98 g/cm^3), it is lower than lead (11.34 g/cm^3). In addition, its atomic mass weight is 208.98 AMU, which means that it can interact with the photons of high energy radiation, such as X-ray or γ -ray emission. All of these features make it possible for bismuth to be a good candidate for a lead substitute. In fact, bismuth oxide (Bi_2O_3) has been intensively investigated because it has a better protective effect than lead oxide [18,20]. Due to its low melting temperature (139°C), it can be easily processed with the polymer matrix in an internal mixer to produce a well-mixed and uniformly dispersed composite. The composite laminates produced were lighter, safer, more flexible and much easier to handle than lead or lead compounds.

In this chapter, we report the effectiveness for X-ray and γ -ray shielding of the multilayer structures and mixed composite laminates. The effects of dispersion of the bismuth-tin alloy, of the alignment of the bismuth-tin alloy impregnated into cotton fabrics, and of laminating it with a tungsten-containing film or a bismuth-tin alloy containing film. The maximum energy of irradiated X-rays was 150 keV, which is higher than the energy range of typical diagnostic X-ray (20~120 keV). And the acceleration voltage of γ -ray was 662 keV. The prepared composite films and sheets

were found to exhibit quite effective electromagnetic radiation shielding. In addition, they are lighter, more flexible, safer, and much easier to handle than lead.

2. 2. Experimental Section

2. 2. 1. Materials

Polyolefin elastomer (POE, LC-170, LG Chem) and poly (ethylene-vinyl acetate) (EVA containing 45% vinyl acetate, LG Chem) were used as the polymer matrix because they can form tough sheets without cracking over long time durations. Tungsten powders with an average particle size of $\sim 140 \mu\text{m}$ were purchased from Intramat Advanced Materials (U.S.A.). The Bismuth-Tin alloy (BiSn, a 58% Bi and 42% tin eutectic alloy) was purchased from Daegutech (Korea). It has a melting temperature of $139 \text{ }^\circ\text{C}$ and a density of $\rho = 8.56 \text{ g/cm}^3$. A tin-silver-copper alloy (99%-0.3%-0.7%, commercially known as SAC0307, with a melting temperature of approx. 220°C) was supplied by Changsung (Korea). Two tungsten plates of different thickness ($W_{0.2}$ (0.2mm) and $W_{0.3}$ (0.3mm)) were purchased from Dongjin Special Metals. Stearic acid (Aldrich) and NAUGARD-445 (Uniroyal) were used as a lubricant and an antioxidant, respectively. In order to ensure good adhesion and better dispersion in the elastomer, the surfaces of the tungsten particles were wrapped with polyethylene molecules via the in-situ polymerization method (the in-situ

Ziegler-Natta polymerization of polyethylene on tungsten nanoparticles with surfaces impregnated by a metallocene catalyst).

2. 2. 2. Sample Preparation

The metallic materials mentioned above were selectively mixed with fixed EVA to POE ratio of 7:3 for 10 minutes in a twin-screw internal mixer (Haake Rheomix model 600p) at 100 °C and 100 rpm. The weight ratio of the metal powder to polymer was fixed at 400 parts per hundred of resin (phr) which means that the weight of metal powder in each sample is 4 times that of the polymer. The mixed samples were pressed at 80 °C with a hot press machine (CARVER AutoFour/30H12) for 5 minutes and then annealed at room temperature for 5 minutes. All the samples prepared with such processes were shaped into thin sheets (5cm x 5cm) of different thickness.

A 400 phr suspension of BiSn in silicone oil was prepared. The suspension was painted onto a cotton fabrics (gauze). After stacking multiple plies of painted cotton gauze together, it was stored on mesh wire for a day to allow the silicone oil to flow out. The stack was pressed for 7 minutes at 135 °C. It was then roll-pressed again for 5 minutes at 130 °C. The pressing temperature was maintained just below the melt temperature of BiSn to prevent the melt from oozing out of the stack. The pressed stack was washed with hexane several times to remove any remaining silicone oil and dried in an oven for 24 hours. The multilayer sheet was later laminated with a

thin film of a premade tungsten-containing film or a BiSn-containing film by pressing for 7 minutes at 135 °C.

The fractured cross sections of the samples were examined with FE-SEM (Hitachi High Technologies America, Inc) to observe the melt phase dispersion.

2. 2. 3. X-Ray Irradiation and Analysis

The X-ray generator (YXLON Y.TU 450-D09) described previously was used to irradiate the samples with photons (Figure 2. 1) [25]. Low-energy photons generated in the X-ray tube were removed with an Al filter to increase the average energy of the photons (beam-hardening) [26]. The applied voltage, current and irradiation time were fixed at 150 keV, 10 mA and 60 s, respectively, for a fixed absorbed dose of 1 Gy (J/kg). A Gafchromic EBT film (International Specialty Products) consisting of two separate active layers between two clear polyester films was used to measure the dose transmitted through the samples [27,28]. When incident photons transmit the film, the monomers in the active layers start polymerizing and take on a darker color. All the samples were irradiated 40 cm below the X-ray tube. In order to exclude scattering, an X-ray shielding lead plate was placed under the Gafchromic film.

The irradiated film undergoes a color change as the energy of the incident photons becomes stronger. The degree of color change was quantified by determining the color of each films with a high-performance color scanner (Epson Expression 10000XL). The color can be converted into an optical density by determining the numerical values of the dots on the scanned image [27,28]. The absorbed dose (the

energy absorbed per unit mass of the absorber medium due to radiation exposure) was then obtained for each sample with a reference dose-optical density curve. Note that such values for the absorbed doses do not include either biological effects of the radiation type or the distribution effects of radioactive materials on human exposure [29]. For instance, alpha particles cause much greater damage to the human body, 20 times stronger than its absorbed dose. Thus, the value for the absorbed dose should in principle be modified by considering the biological effects on the human body due to variation in radiation type and other modifying factors. Electromagnetic radiations, however, don't need modification to account the biological effectiveness because such radiation has the same effects on the human body as the absorbed dose. Therefore, the effectiveness of the X-ray shielding provided by any material can be quantified by using film dosimetry [30]. From the obtained absorbed dose, the ratio (I/I_0) can be calculated as follows:

$$\frac{I}{I_0} = \exp(-\mu x) \quad (2. 1)$$

where I_0 and I are the absorbed dose of the incident (1Gy) and penetrated X-ray radiation respectively and x is the thickness of the shielding sheet [25,30]. The exponent μ (cm^{-1}) is a linear attenuation coefficient, which is another form of the dose ratio that can be used to measure the shielding effectiveness of a material [29]. The shielding effectiveness is sometimes expressed as a mass attenuation coefficient, μ/ρ (cm^2/g , the linear attenuation coefficient divided by the density of the matter) [31]. The mass attenuation coefficient is useful for separating the effects of density on shielding effectiveness from other factors and enables the evaluation of the effects of structural properties, whereas the linear attenuation coefficient and the dose ratio

are appropriate for the evaluation of the overall effectiveness of the specimen in blocking electromagnetic radiations [25,31].

2. 2. 4. γ -ray Irradiation and Analysis

: All γ -ray shielding measurements were done by the Korea Atomic Energy Research Institute. The cesium radiation source was supplied by the Nuclear Safety Research Institute of Korea. Attenuation measurements were performed using a narrow-beam geometry. The experimental set-up was similar to the one used by Singh et al [20,24]. The source and sample systems were mounted on home-made composite stands with adjustable height. A 1.5"x1.5" NaI (TI) crystal having an energy resolution of 12.5% at 662 keV γ -rays from the decay of ^{137}Cs was used for the measurements of radiation attenuation [32-37]. The distance between the ^{137}Cs γ -ray source and the specimen was 129.14 cm and the distance between the specimen and the detector was 5 cm (Figure 2.2). The experimental accuracy was confirmed by measuring the attenuation coefficient of aluminum slab having a thickness of 1cm [38,39]. The experimental set up was tested before and after each set of runs by quantitative estimates of accuracy and stability. The effectiveness of the γ -ray shielding provided by equation (2.1). The shielding efficiency was determined as $\eta = 1 - (I/I_0)$.

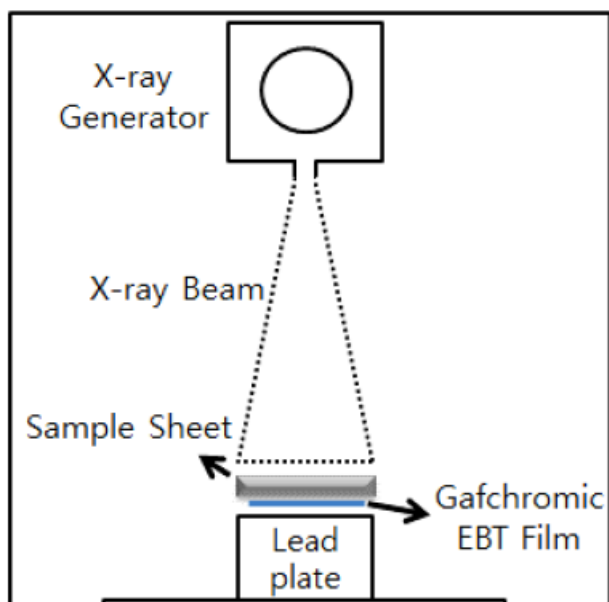


Figure 2. 1. Schematic illustration of X-ray irradiation apparatus

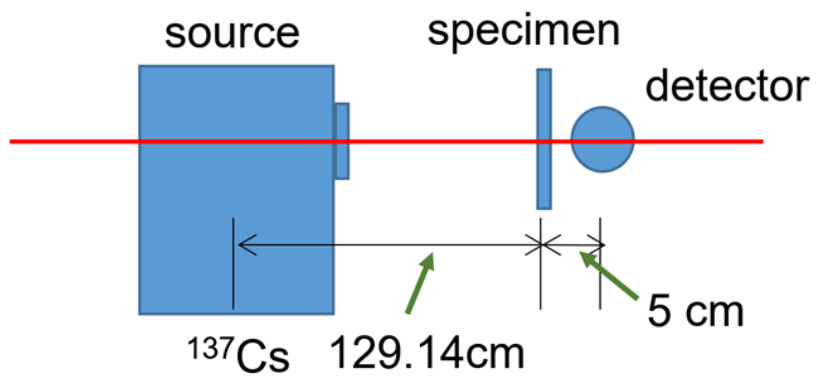


Figure 2. 2. Schematic figure of the experimental set-up for determining incident and transmitted intensities of gamma rays

2. 3. Results and Discussion

2. 3. 1. The effect of metal fillers on X-Ray shielding

As mentioned above, the two critical factors that determine the effectiveness of a material's X-ray shielding are its density and its atomic number, Z . The linear attenuation coefficient is an exponent that is influenced by the critical factors. Therefore, the mass attenuation coefficient is also used to characterize such materials while excluding the effects of density [25].

The shielding effectiveness of each of three different composites (1mm thickness, including 400 phr metal particles) is displayed in Figure 2. 3. Their numerical results are presented in Table 2. 1 for clarification. The shielding effectiveness of Sn particle (SnP) composites or BiSn particle (BiSnP) composites are quite good. The efficiency of the SnP composite is lower than that of the tungsten composite whereas that of the BiSnP composite is comparable to that of tungsten. The attenuation coefficient of the BiSnP composite is larger than that of tungsten, but that of SnP is smaller (Table 2. 1). If we compare their mass attenuation coefficients, that of the BiSnP composite is the largest, then SnP is next, and then that of the tungsten particle (WP) composite is lowest. Thus, the shielding efficiency of SnP is lower than that of tungsten due to its lower density (α phase = 5.769 g/cm³ and β phase = 7.265 g/cm³) than tungsten (19.25 g/cm³) of which density is much higher than lead (11.34 g/cm³).

The mass attenuation coefficient of tin is larger than that of tungsten due to its lower K-edge energy which is the binding energy of the K (innermost) shell electron

of an atom. There is a sudden increase in the attenuation coefficient at a photon energy, just above the binding energy of the K shell electrons of the atoms interacting with the photons. This sudden increase is due to photoelectric absorption of the photons [40]. For this interaction to occur, the photons must have more energy than the binding energy of the K shell electrons (the K-edge energy) [30,40,41]. A photon with an energy just above the binding energy of the electron is more likely to be absorbed than a photon with an energy just below this binding energy. The K-edge energy values of tin, tungsten and bismuth are 29 keV, 69 keV, and 90 keV, respectively [30]. The K-edge energy of bismuth is slightly higher than that of lead. Consequently, tin has a higher mass attenuation coefficient in the photon energy range from 29 keV (the tin K-edge energy) to 69 keV (the tungsten K edge energy), but beyond the K-edge energy of tungsten, its mass attenuation coefficient is lower. As a result, the mass attenuation coefficient of tin is similar to or higher than that of the tungsten in the X-ray photon energy range (150 keV in this study). This implies that tin could be a good substitute for lead for X-ray shielding in the energy range between 29 keV to 88 keV (the K-edge energy of lead) because of lower weight and its higher attenuation coefficient values. By the same token, the higher K-edge energy of bismuth means that it has a higher mass attenuation coefficient above its K-edge energy than tungsten. Since the BiSn alloy is composed of 58% bismuth and 42 % tin, its X-ray shielding effectiveness is better than or close to tungsten for the whole energy range. The dose ratio of SnP is a little bit higher than that of tungsten, but that of BiSn is slightly lower. This result indicates that BiSn is an excellent substitute for lead in the shielding X-ray radiation because of the selective

attenuation by the Sn and Bi component throughout the whole X-ray energy range. Further note that tungsten's shielding effectiveness is mainly due to its high density.

Another merit of the BiSn alloy is that it melts at low-temperature around 139 °C which is lower than the processing temperatures of most polymers. We made use of this peculiar thermal property, to prepare cotton-reinforced composites. Table 2.2 presents the specifications of the prepared composite samples and their performances. With the use of these composites as X-ray shielding aprons or other gears in mind, we limited the number of painted cotton sheets to less than 10, which results in a thickness of approximately 1 mm. The dose ratios of the multilayered sheets decrease progressively with the layer number (Table 2.1). Interestingly, a 10-layer sheet with a thickness of 1 mm exhibits a dose ratio comparable to that of a BiSnP composite with a thickness of 1 mm. Figures 2. 4(a), (b) and (c) are the SEM photographs of virgin gauze, surface and its cross-sectional views of a sheet with 10 layers, respectively. It is clear that some of the BiSn particles have melted and thus been able to impregnate the gauze space (compare Figure 2. 4(a) (virgin gauze), (b), and (c)). As the pressing temperature increases, more agglomerated particles appear (Figures 2. 4(d), (e) and (f)). The flexibility of multilayered sheets was quite good like a rubber sheet which makes them suitable for the fabrication of shielding apparel as long as they can effectively attenuate X-ray radiation.

Although the multilayered structures do shield X-ray radiation, uniform coverage was difficult to achieve. We painted the BiSn particle suspension onto the cotton fabrics. The particles do not cover the whole surface uniformly due to the weave of the cotton gauze (Figure 2.4(a)) and the characteristics of the suspension. The

processing temperature was selected to be close to the melting temperature of the BiSn particles in order to promote adhesion between the layers. It appears that some small particles in adjacent layers melt and adhered together (Figure 2.4(b), (c), (e), and (f)). Pressing the sheets at these temperatures is expected to enable the deformation of the dispersed BiSn particles so that the distribution of BiSn on the cotton sheet becomes more uniform. Three-dimensional and two-dimensional plots of dose ratio for the whole sheet surface are shown in Figures 2. 5(a) and (b), which reveal that there are some high and low dose ratio points.

If the number of layers is increased to produce a thicker sheet, the dose ratio becomes more uniform, although the flexibility will be lost. Hence, we covered the sheet surface with a thin layer either of BiSnP or of WP (0.4 mm thickness, 400 phr particles included). This lamination results in a more uniform dose ratio over the whole sheet area as well as lowering the dose ratio below that of the stacked sheet (Table 2.2, Figure 2.5(c) and (d)). The dose ratio of the sheet with a BiSnP film is more uniform (Figure 2.5(d)) than that of the sheet with a WP film (Figure 2.5(c)), probably because the dispersion of BiSn particles in the matrix polymer is better than that of the tungsten particles (Figure 2.4). Further, the addition of the BiSnP film improves the shielding effectiveness of the composite sheet due to the smearing of melted BiSn.

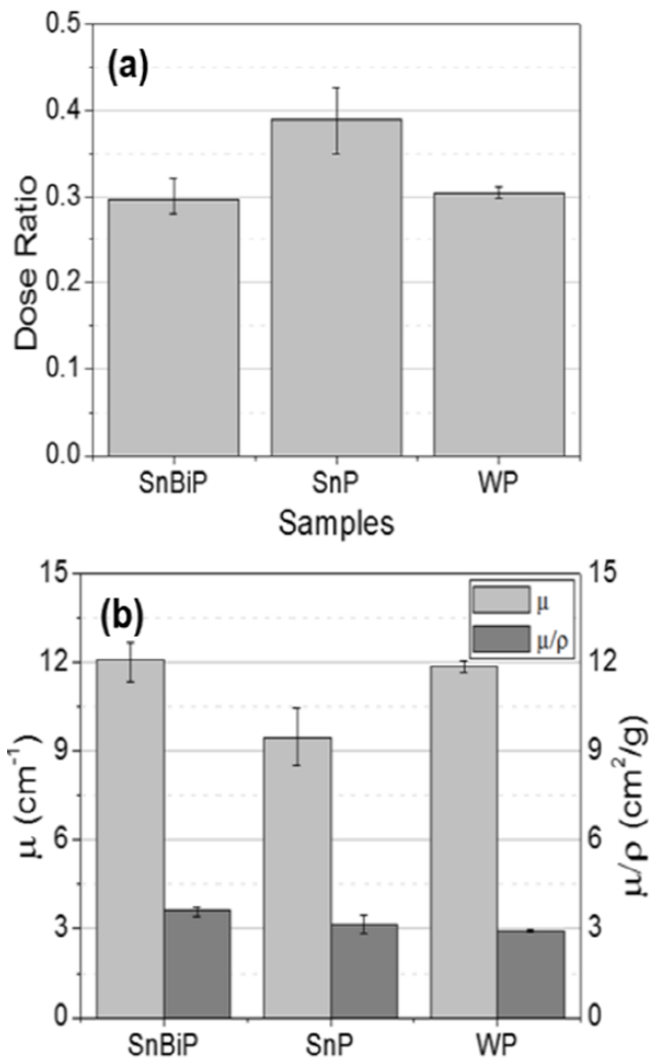


Figure 2. 3. (a) Dose ratios (the ratio of the number of transmitted photons to the total number of incident photons) of X-rays through the three composites (BiSn, Sn and tungsten particles) with a thickness of 1mm, containing 400phr metal particles. (b) The linear attenuation coefficients and mass attenuation coefficients of the three composites.

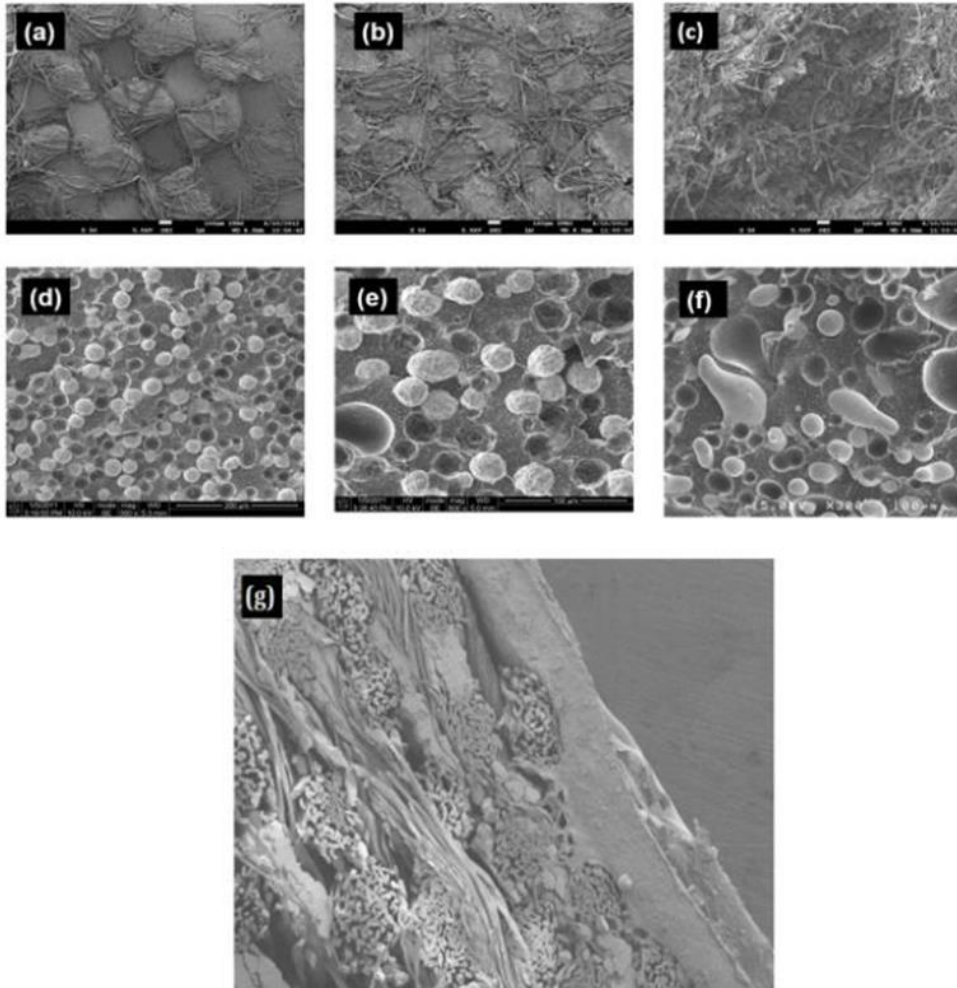


Figure 2. 4. SEM photographs: (a) virgin gauze, (b) the surface of a 10-layer laminated sheet, (c) a cross sectional view of a fractured surface of (b); fractured surfaces of 10-layer sheets pressed at 135 °C (d), 139 °C (e), and at 160 °C (f). Some of the BiSn particles melt at the pressing temperature. (g) Photograph of a cross-section of a BiSnP stacked sheet attached to a 0.4mm WP composite film. Some melted BiSn particles are smeared inside the stacked sheet.

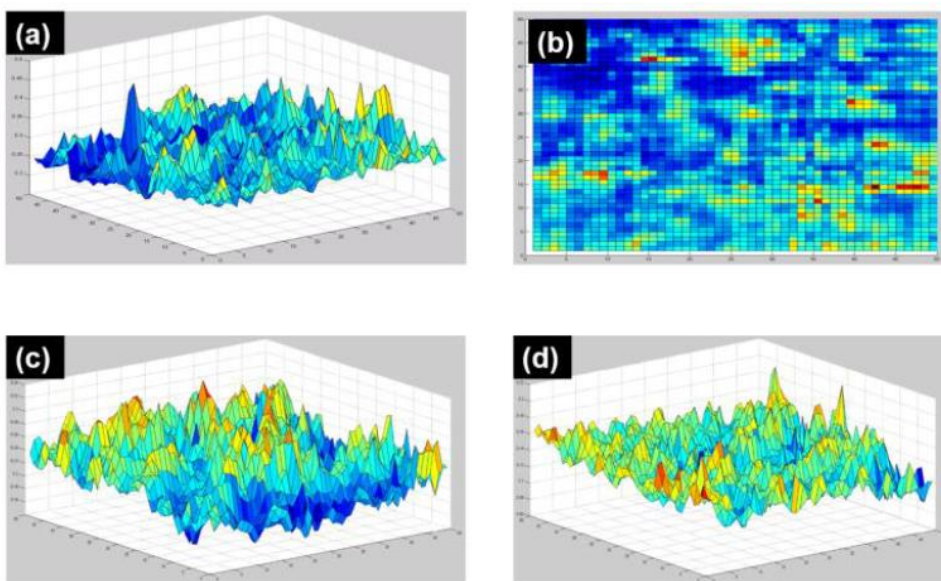


Figure 2. 5. (a) 3D plot of the dose ratio for the BiSnP-impregnated multiple sheets (10), (b) 2D plot of (a), (c) 3D plot of the dose ratio for the BiSnP-impregnated multiple sheets (10) with a 0.4mm WP film, (d) 3D plot of the dose ratio for BiSnP-impregnated multiple sheets (10) with a 0.4mm BiSnP film. The films and stacked sheets were pressed together to ensure good adhesion.

Table 2. 1. Dose ratios, attenuation coefficients, and mass attenuation coefficients of various composites containing 400 phr metal particles with a thickness of 1mm

Particle	D/D ₀	μ	μ/ρ
BiSnP	0.298 \pm 0.02	12.12	3.62
SnP	0.390 \pm 0.04	9.45	3.13
WP	0.305 \pm 0.01	11.88	2.95

Table 2. 2. Dose ratios for BiSnP multilayered sheets and laminates with either a BiSnP 400 phr composite film or a WP 400 phr composite film.

BiSnP impregnated sheet number	5	7	10	10 layers + 0.4mm BiSnP 400 phr film	10 layers + 0.4mm WP 400 phr film
Thickness (mm)	0.63	0.84	1.1	1.2	1.2
Overall Density (g/cm ³)	3.75	3.50	3.79	3.76	4.57
Dose Ratio (D/D ₀)	0.50 ± 0.02	0.35 ± 0.04	0.33 ± 0.03	0.30 ± 0.03	0.26 ± 0.02

2. 3. 3. γ -Ray Shielding Properties

Figure 2. 6 shows the extrudates from the extruder, the SEM photograph of the fractured sectional view of extrudates and the flexibility of the 5 mm thick BiSn/polymer sheet. The extrudate looks like an ordinary elastomeric extrudate, but the BiSn alloy is well mixed and dispersed in the polymer matrix (Figure 2.6(b)). The produced BiSn/polymer sheet is very flexible and can be easily bent (Figure 2.6(c)).

The shielding efficiency of the BiSn alloy/polymer composite was checked first. All results are averages of five measurements for each specimen. Table 2.3 shows the γ -ray shielding rate (The dose rate was 368 mGy/h, the energy before attenuation with 5.5% reliability). As the thickness of the BiSn/polymer sheet increases, the dose ratio decreases which means that the shielding effect also increases. The transmittance shows an exponentially decreasing behavior following the Beer-Lambert law: $I/I_0 = \exp(-0.0308*x)$ where x is the thickness of the composite in mm (Figure 2.7). This expression fits the data with the correlation of 0.9995. According to this correlation, γ -ray shielding of 95 % can be achieved if the BiSn/polymer composite sheet is thicker than 98 mm. The accuracy of this evaluation is confirmed later.

In order to see the shielding characteristics of the tungsten sheet, the dose rate of tungsten sheet was measured separately against the same ^{137}Cs radiation. Combination of 0.2 mm and 0.3 mm tungsten sheets provides the proper thickness variation. The γ -ray transmittance of the tungsten sheet also follows the Beer-

Lambert law (Figure 2.8). The transmittance of the tungsten sheet can be fitted as $(I/I_0)_{\text{Tungsten}} = \exp(-0.23282 \cdot x)$ where x is the thickness of tungsten in mm. The correlation was 0.994. Based on this result, 95 % shielding of the γ -ray can be achieved with the tungsten sheet of 12.9 mm thickness. Compared with the BiSn/polymer composite, which needs a sheet thickness of 98 mm, tungsten sheets shows the same shielding efficiency with 1/7 thickness. This agrees well with the relative ratio between the exponential factors of BiSn/polymer and tungsten, i.e., 0.0308 for (BiSn/polymer)/ 0.23282 for tungsten = $0.1323 \times 98 \text{ mm} = 12.96 \text{ mm}$ which verifies the accuracy of the measurements because both sheets follow the Beer-Lambert law. The linear attenuation coefficient of tungsten is seven times larger than that of the BiSn/polymer composite.

In the case of a multilayered radiation shielding material, the dose ratio and the shielding efficiency of the composite film prepared by the combination of BiSn/polymer composite and tungsten sheet can be predicted by using the separately obtained dose rate fits as long as they follow the Beer-Lambert law. To confirm this preposition, tungsten flakes of different thickness were mounted on the BiSn/polymer composite sheet having a thickness of 10 mm. Figure 2.9 and Table 2.4 show the measured and calculate dose ratios. The measured and calculated values are exactly the same, indicating that these stacked sheets act like a composite of two shielding components, both of which follow the Beer-Lambert law. When the thickness of BiSn/polymer composite sheet is set to 10 mm, a 95% shielding can be achieved if the thickness of the tungsten flakes is 12 mm. This means that the

shielding efficiency of 10 mm thick BiSn/polymer composite is equivalent to less than 2 mm thick tungsten sheet.

There is a sudden increase in the attenuation coefficient at a photon energy just above the binding energy of the K shell electrons of the atoms interacting with the photons, which is due to photoelectric absorption of the photons [38,39]. For this interaction to take place, the photons must have more energy than the binding energy of the K shell electrons (the K-edge energy). The K-edge energy values of tin, tungsten and bismuth are 29 keV, 69 keV, and 90 keV, respectively. The K-edge energy of bismuth is slightly higher than that of lead (88 keV). Consequently, tin has a higher mass attenuation coefficient in the photon energy range from 29 keV (the tin K-edge energy) to 69 keV (the tungsten K-edge energy), but beyond the K-edge energy of tungsten, its mass attenuation coefficient is lower. As a result, the mass attenuation coefficient of tin is similar to or higher than that of the tungsten in the X-ray photon energy range (until 150 keV). This means that tin, because of lower density and its higher attenuation coefficient value, can be a good substitute for lead for X-ray shielding in the energy range between 29 keV to 88 keV (the K-edge energy of lead). However, the mass attenuation coefficient of tin becomes lower than that of the tungsten once the energy level goes beyond that of tungsten (69 keV) whereas the higher K-edge energy of bismuth (90 keV) affords a higher mass attenuation coefficient over the high energy range of ^{137}Cs radiation (665 keV). The X-ray shielding efficiency of the BiSn alloy consisted of 58% bismuth and 42 % tin is, therefore, better than or close to tungsten for the X-ray energy range, but its γ -ray shielding efficiency is lower than tungsten in the γ -ray energy range. Therefore,

thicker plate should be used to achieve such a high shielding effect as lead or tungsten.

Fan et al. investigated Z-graded shielding (laminating of various Z-number materials) for microelectronics in satellite. Though it has been done by computer simulation, the results demonstrate advanced shielding performance of laminated metal sheets. In order to achieve the high attenuation with a thin sheet, laminates of (BiSn/polymer) / tungsten were prepared by attaching the tungsten flakes to (BiSn/polymer) using an adhesive. The shielding effect of multilayered stack of (BiSn/polymer)/tungsten flakes having a thickness of 0.5 mm is presented in Table 2.5. The shielding efficiencies for single stack and double stack are measured values while the triple stack values are calculated from the fitting equation of the single stack and the double stack. As the thickness of the BiSn/polymer sheet increases, the shielding effect also increases, and the dose ratio decreases. If we place the 1mm thick tungsten flake on the 1 mm BiSn/polymer composite sheet, a 95 % shielding can be achieved through the 10 stacks of (BiSn/polymer)/tungsten multilayer, which means total thickness of 20 mm of laminated stack is required (Table 2.6).

Though tungsten flakes are quite efficient to shield the γ -ray of ^{137}Cs (667 keV), it is not easy to be used for the flexible protective garments or gear applications because of its processing difficulty due to its high melting temperature [42]. On the other hand, the BiSn/polymer composite is easy to fabricate and flexible but should be quite thick to shield the γ -ray. Hence, we have devised a strategy to prepare a flexible but high-shielding stack of (BiSn/polymer)/tungsten laminates. Its structure is schematically presented in Figure 2.10. Using an adhesive, a tungsten flake of a

certain shape (rectangle, triangle, or other polygonal or circular shape) having a thickness of 5 mm or less (this thickness is arbitrary, but the thinner is the better for processing) is placed on the BiSn/polymer sheet (Figure 2.10(a)). The tungsten flakes are regularly arranged so that they do not touch each other on the same BiSn/polymer sheet so that a (BiSn/polymer)/tungsten layer can be bent over 90°. The thinner and the smaller is the flake size, the more flexibility it can offer. The single layer can afford full flexibility needed for the gear or garment fabrication [43-45]. However, γ -ray can pass through the space between the tungsten flakes. Then, the second layer of multilayer laminates should be positioned on top of the first layer to cover the empty space between the tungsten flakes on the first layer. This can be accomplished by alternatively arranging the tungsten flakes on different layers such that the center of the second layer tungsten flakes cover the space between the tungsten flakes on the first layer that the γ -ray can pass through (Figure 2.10(b)). Depending on the tungsten flake thickness, the total number of stacking layers and flexibility of laminates are determined.

A concomitant benefit of using (BiSn/polymer)/tungsten laminates is not only the complete shielding of electromagnetic radiation such as X-rays or γ -rays, but also the shielding of the neutron transmission since the polymer (EVA and polyolefin elastomer) contains a lot of hydrogen atoms which are very effective to protect from the neutron particles. According to our previous study on the neutron shielding property of high-density polyethylene (HDPE)/boron filler composite, the pure HDPE sheet with a thickness of 2 cm showed more than 23.5% attenuation of ^{252}Cf (2.1 MeV) neutron transmission. The blend of EVA and polyolefin contains more

hydrogen than HDPE to shield the neutron particles. Further details on the neutron shielding effects of (BiSn/polymer)/tungsten composites are underway and will be reported in the future.

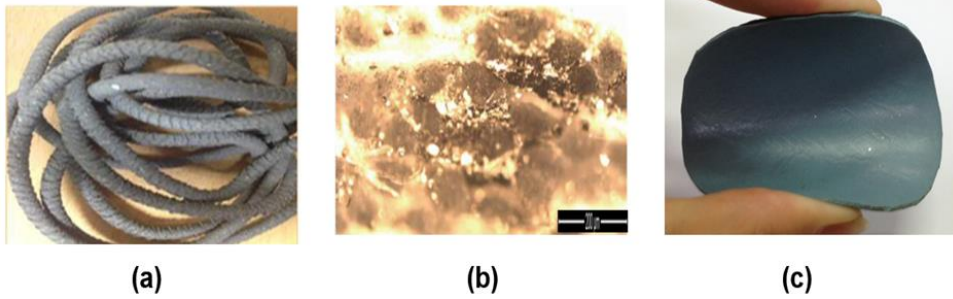


Figure 2. 6. (a) The extrudate of BiSn/polymer, (b) SEM photograph of the fractured sectional view (scale bar is 200 μ m), (c) Bent BiSn/polymer sheet

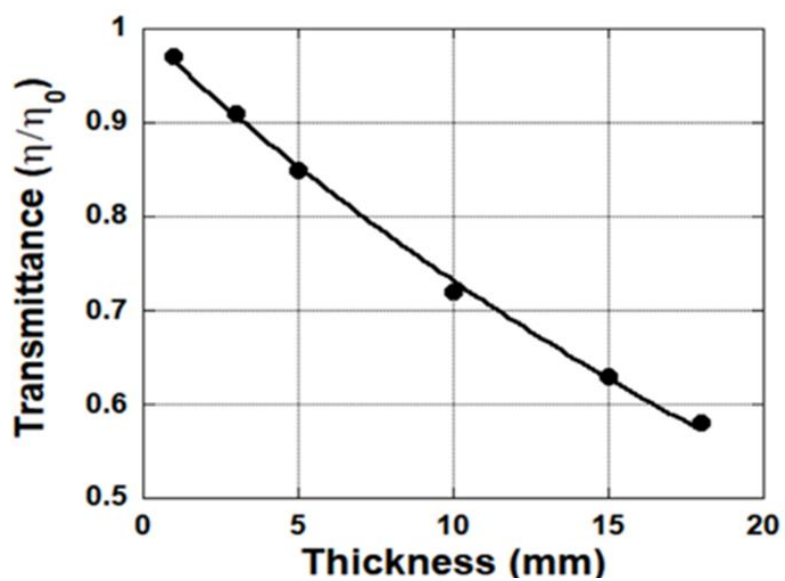


Figure 2. 7. γ -ray transmittance through the BiSn/polymer composite sheet. The line is a fitting of the data using the Beer-Lambert law, $I/I_0 = \exp(-0.0308 \cdot x)$, with a correlation of 0.9995.

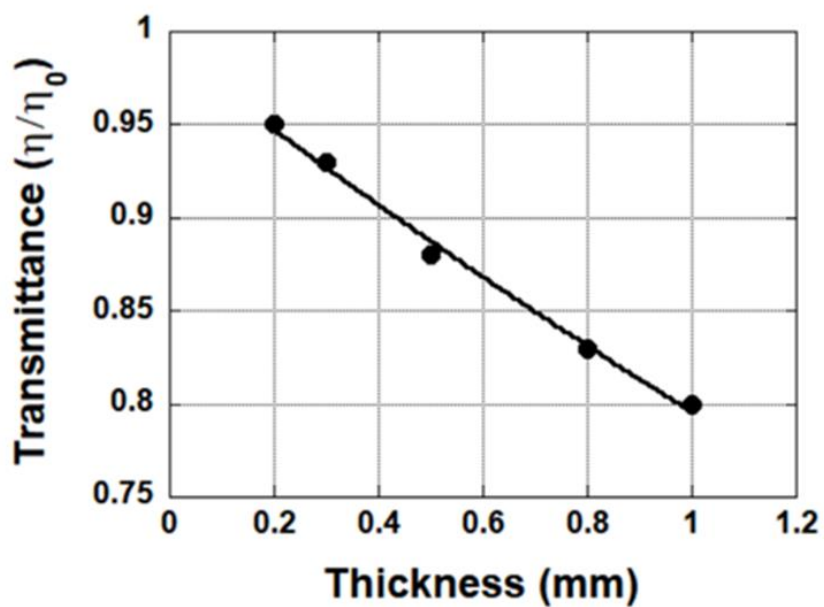


Figure 2. 8. γ -ray transmittance through the tungsten sheet. The line is a fitting of the data using the Beer-Lambert law, $I/I_0 = \exp(-0.23282 \cdot x)$ with a correlation of 0.994.

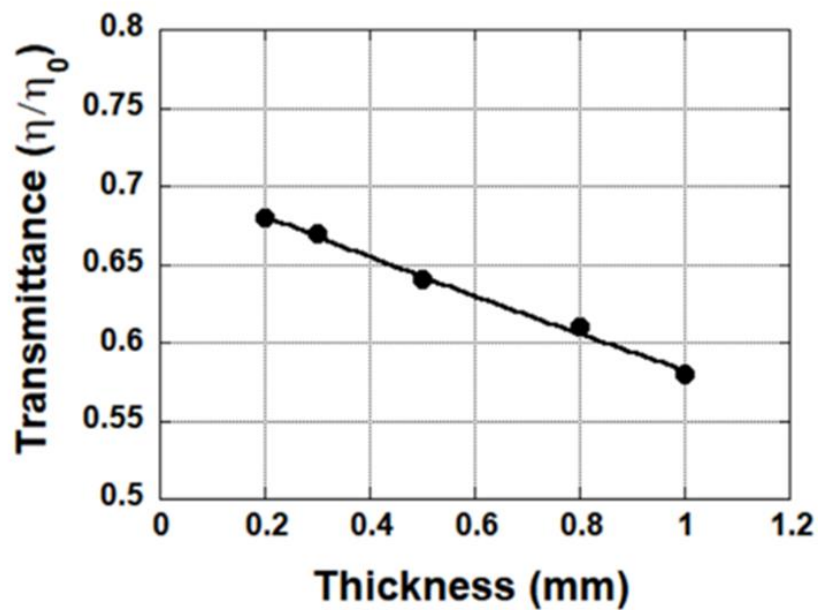


Figure 2. 9. γ -ray transmittance through the (BiSn alloy/polymer composite sheet (10mm) + tungsten sheet). The line is the calculated values using the measurement values of each sheet.

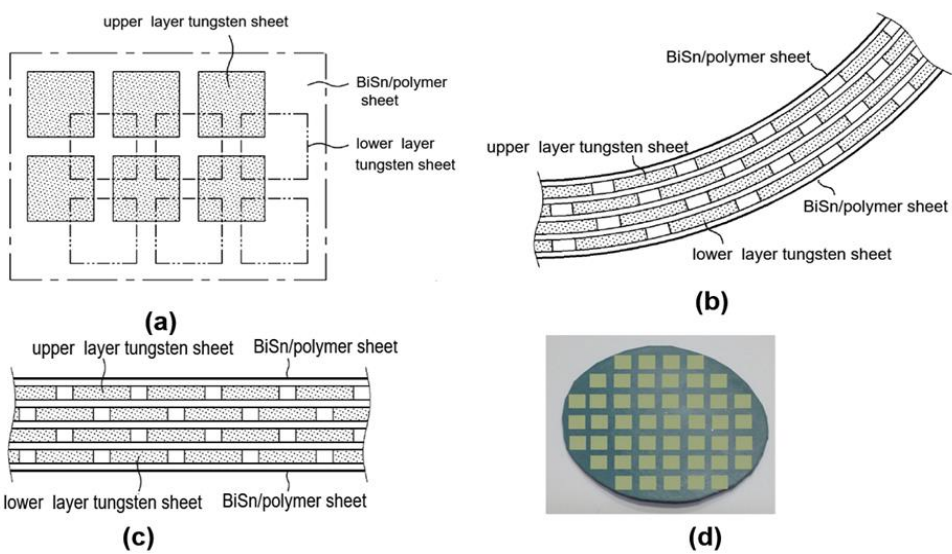


Figure 2. 10. Schematic figure of the multistacked sheet of (BiSn/polymer sheet + tungsten sheet) (a) normal view, (b) flexible bent multilayered sheet, (c) sectional view, (d) photograph of a single layer of BiSn/polymer sheet + tungsten sheet.

Table 2. 3. γ -ray shielding efficiency of the BiSn alloy/polymer composite.

Thickness	1mm	3mm	5mm	10mm	15mm	18mm
Transmittance (measured)	0.97	0.91	0.85	0.73	0.63	0.58
Shielding efficiency (=1-transmittance)	0.03	0.09	0.15	0.27	0.37	0.42

Table 2. 4. γ -ray shielding efficiency of the (BiSn alloy/polymer composite sheet (10mm) + tungsten sheet).

Tungsten plate thickness	0.2mm	0.3mm	0.5mm	0.8mm	1mm
Transmittance	0.68	0.67	0.64	0.61	0.58
Shielding efficiency (measurement)	0.32	0.33	0.36	0.39	0.42
Calculated value from using Table 1 and Table2 values	0.32	0.33	0.36	0.4	0.42

Table 2. 5. Shielding efficiency of multilayer sheets (BiSn/polymer sheet of various thickness + 0.5mm tungsten sheet)

BiSn/Polymer sheet thickness	1mm	3mm	5mm	10mm	15mm	18mm
Single layer (measured)	0.15	0.2	0.25	0.37	0.45	0.49
double layer (measured)	0.27	0.36	0.44	0.6	0.69	0.74
Triple layer (calculated)	0.38	0.49	0.58	0.75	0.83	0.87

Table 2. 6. Calculated shielding efficiency of multistacked (1mm thick BiSn/polymer + 1mm thick tungsten plate) sheet.

No. of stacked layers	1	2	3	4	5	6
Shielding efficiency of multilayer sheet (calculated)	0.15	0.20	0.25	0.37	0.45	0.49

2. 4. Conclusions

To test the feasibility of substitutes for lead in X-ray radiation shielding applications, three different non-lead metals (tungsten, tin and bismuth-tin alloy (BiSn)) were used to prepare metal-polymer composites. Tin exhibits a shielding efficiency that is comparable to that of tungsten between 29 keV (the K-edge energy of tin) and 69 keV (the K-edge energy of tungsten). Considering the lightness of tin, it can be used to shield low energy X-ray radiation. BiSn exhibits much better shielding (a low dose ratio) than tin, and the shielding was comparable to that of tungsten for all X-ray energy ranges. It is composed of 42% tin and 58% bismuth, so it effectively shields low energy X-ray radiation due to its tin component and high energy level radiation due to its bismuth component; the K-edge energy (90 keV) is much higher than that of tungsten. Thus, we have demonstrated that BiSn exhibits better performance than tungsten and is a suitable candidate for X-ray shielding applications.

Based on this result, we pressed a multilayered sheet of gauze on which BiSn suspension was painted. The sheet was found to exhibit good X-ray shielding but also non-uniformity in the dispersed metal phase. The lamination of the stacked sheet with a WP film or a BiSnP film was found to improve the non-uniform dose ratio over the whole surface. The melting and agglomeration of the BiSn particles mean that the sheet laminated with a BiSnP film exhibits a more uniform dose ratio than the sheet laminated with a WP film. An important feature of the BiSn alloy is its absorption of high-energy photons by its high atomic number component (bismuth)

and low-energy photons by its low atomic number component (tin), which means that its X-ray radiation shielding is very effective.

The BiSn alloy promises to be useful in the manufacturing of X-ray radiation shielding apparels because of its excellent shielding, nontoxicity and low density. Further, it can be processed with typical polymer processing equipment. These results suggest that the use of non-lead metal (BiSn)/polymer composites as a substitute for the harmful lead currently widely used in X-ray shielding plates and medical gowns is feasible.

In order to test the feasibility of substitutes for the lead in the shielding equipment against high energy radiation of γ -ray (667 keV from ^{137}Cs source), multilayer composites of (BiSn/polymer)/tungsten were fabricated. All prepared composite sheets show a fairly good shielding ability against the high energy γ -ray radiation. Both the BiSn (400phr)/polymer sheet and tungsten flakes showed the shielding efficiency following the Beer-Lambert law. The transmittance of the tungsten sheet is expressed as $(I/I_0)_{\text{Tungsten}} = \exp(-0.23282 \cdot x)$ while that of the BiSn/polymer composite follows the fitting equation of $(I/I_0)_{\text{BiSn/polymer}} = \exp(-0.0308 \cdot x)$ where x is the thickness of the composite material in mm. Therefore, tungsten sheet exhibits the 7 times shielding efficiency than the BiSn (400phr)/polymer composite sheet of the same thickness. When the BiSn/polymer composite sheet and tungsten sheet are combined to form multilayered laminates, a synergistic effect was observed such that 12 mm thick tungsten sheet show the same 95% shielding efficiency once it is adhered on the 10 mm thick BiSn/polymer

References

- [1] Shaheen Dewji, S.; Hertel, N. E. (Eds), *Advanced Radiation Protection Dosimetry*; Taylor & Francis Inc, Portland, United States,2019, Chapt. 1-3
- [2] Martin, A.; Harbison, S.; Beach, K.; Cole, P.; *An Introduction to Radiation Protection*; Taylor & Francis, London, United Kingdom, 2018, Chapt. 1-7.
- [3] Statkiewicz-Sherer, M. A.; Visconti, P. J.; Ritenour, E. R.; Haynes, K.; *Radiation Protection in Medical Radiography*; Elsevier, St. Louis, U.S.A., 2017; Chapt. 1-3
- [4] Seeram, E.; Brennan, P. C.; *Radiation Protection in Diagnostic X-Ray Imaging*; Jones and Bartlett Publishers, Sudbury, U.S.A. 2016; Chapt.1-3
- [5] Stabin, M.G.; *Radiation Protection and Dosimetry: An Introduction to Health Physics*; Springer-Verlag New York Inc., N.Y. U.S.A., 2010; Chapt. 1-6
- [6] Martin, J. E.; *Physics for Radiation Protection*; Wiley-VCH Verlag GmbH, Weinheim, Germany. 2013, Chapt. 8-10
- [7] Yeow, J. T. W.; Nambiar, S. Polymer-Composite Materials for Radiation Protection, *ACS Appl. Mater. Interf.* **2012**, 4, 5717–5726
- (8) William, H. H. Radiation Protection, 1st ed., LEWIS PUBLISHERS, U.S.A, 1994.
- [9] Harish, V.; Nagaiah, N.; Prabhu, N.; Varughese, K. T. Preparation and Characterization of Lead Monoxide Filled Unsaturated Polyester Based Polymer Composites for Gamma Radiation Shielding Applications. *J. Appl. Polym. Sci.* **2009**, 112, 1503.
- [10] Yue, K.; Luo, W.; Dong, X.; Wang, C.; Wu, G.; Jiang, M.; Zha, Y.; Radiation: A New Lead-Free Radiation Shielding Material for Radiotherapy. *Prot. Dosimetry.* **2009**, 133, 256.

- [11] Kim, Y.; Park, S.; Seo, Y., Enhanced X-ray Shielding Ability of Polymer-Nonleaded Metal Composites by Multilayer Structuring, *Ind. Eng. Chem. Res.*, **2015**, 5968-5973.
- [12] Uhm, Y. R.; Kim, J.; Lee, S.; Jeon, J.; Rhee, C. K. In Situ Fabrication of Surface Modified Lead Monoxide Nanopowder and Its HDPE Nanocomposite. *Ind. Eng. Chem. Res.* **2011**, 50, 4478.
- [13] Harish, V.; Nagaiah, N.; Prabhu, N.; Varughese, K. T. Thermo-mechanical Analysis of Lead Monoxide Filled Unsaturated Polyester Based Polymer Composite Radiation Shields. *J. Appl. Polymer Sci.* **2010**, 117, 3623.
- [14] Yue, K.; Luo, W.; Dong, X.; Wang, C.; Wu, G.; Jiang, M.; Zha, Y., A New Lead-Free Radiation Shielding Material for Radiotherapy, *Radiat. Protect. Dosim.* **2009**, 133, 256–260
- [15] Mudahar, G. S.; Sahota, H. S. Soil: A Radiation Shielding Material. *Appl. Radiat. Isotopes.* **1988**, 39, 21.
- [16] Fricke, B. L.; Donnelly, L. F.; Frush, D. P.; Yoshizumi, T.; Varchena, V.; Poe, S. A.; Lucaya, J., In-Plane Bismuth Breast Shields for Pediatric CT: Effects on Radiation Dose and Image Quality Using Experimental and Clinical Data *Am. J. Roentgen.*, **2003**, 180, 407–411
- [17] Biswas, R.; Sahadath, H.; Mollah, A. S.; Huq, F., Calculation of gamma-ray attenuation parameters for locally developed shielding material: Polyboron *J. Radiat. Res. Appl. Sci.* **2016**, 9, 26-34
- [18] Singh, H.; Singh, K.; Gerward, L.; Singh, K.; Singh, H.; Nathuram, S.R., ZnO–PbO–B₂O₃ glasses as gamma-ray shielding materials, *Nucl. Instru. Method. Phys. Res. B* **2003**, 207, 257–262
- [19] Singh, K. J.; Singh, N.; Kaundal, R. S.; Singh, K., Gamma-ray shielding and structural properties of PbO–SiO₂ glasses, *Nucl. Instru. Method. Phys. Res. B* **2008**, 266, 944–948

- [20] Akkurt, I.; Akyildirim, H.; Mavi, B.; Kilincarslan, S.; Basyigit, C., Gamma-ray shielding properties of concrete including barite at different energies, *Progr. Nucl. Energ.*, **2010**, 52, 620-623
- [21] Kaçal, M.R.; Akman, F.; Sayyed, M.I.; Akman, F., Evaluation of gamma-ray and neutron attenuation properties of some polymers, *Nucl. Eng. and Tech.* **2019**, 51, 818-824
- [22] Azman, N. Z. N.; Siddiqui, S.A.; Haroosh, H. J.; Albetran, H. M. M.; Johannessen, B.; Yu Donge, Y.; Lova, I. M. Characteristics of X-ray attenuation in electrospun bismuth oxide/polylactic acid nanofibre mats, *J. Synchrotron Rad.* **2013**, 20, 741–748
- [23] Park, S.; Kim, H.; Kim, Y.; Kim, E.; Seo, Y., Enhanced X-ray Shielding Ability of Polymer/Nonleaded Metal Composites by Multilayer Structuring, *MRS Adv.* **2018**, 3, 1789-1797
- [24] Chinthima, N.; Kaewkhao, J.; Kedakew, C.; Chewpraditkul, W.; Pokaipisit, A.; Limsungwan, P.; Study on Interaction of Bi₂O₃, PbO and BaO in Silicate Glass System at 662 keV for Development of Gamma-Rays Shielding Materials, *Prog. Nucl. Sci. Tech.* **2011**, 1, 106-109
- [25] Plionis, A.; Garcia, S.; Gonzales, E.; Porterfield, D.; Peterson, D., Replacement of lead bricks with non-hazardous polymer-bismuth for low-energy gamma shielding. *J. Radioanal. Nucl. Chem.* **2009**, 282(1), 239-242
- [26] Jennings, R. J., A method for comparing beam-hardening filter materials for diagnostic radiology. *Med. phys.* **1988**, 15(4), 588-599.
- [27] Ju, S. G.; Ahn, Y. C.; Huh, S. J.; Yeo, I. J., Film dosimetry for intensity modulated radiation therapy: dosimetric evaluation. *Med. phys.* **2002**, 29(3), 351-355.
- [28] Robar, J. L.; Clark, B. G., The use of radiographic film for linear accelerator stereotactic radiosurgical dosimetry. *Med. phys.* **1999**, 26(10), 2144-2150.

- [29] Martin, A.; Harbison, S.; Beach, K.; Cole, P.; An Introduction to Radiation Protection; Taylor & Francis, London, United Kingdom, 2018, Chapt. 12.
- [30] Schnohr, C. S.; Ridgway, M. C., *X-ray absorption spectroscopy of semiconductors*. Springer Berlin, Heidelberg, Germany, 2015.
- [31] Turner, J. E., *Atoms, radiation, and radiation protection*. John Wiley & Sons., New York, U.S.A., 2008, Chapt. 1.
- [32] Singh, N.; Singh, K. J.; Singh, K.; Singh, H., Comparative study of lead borate and bismuth lead borate glass systems as gamma-radiation shielding materials, *Nucl. Instrum. Meth. Phys. Res. B* **2004**, 225, 305–309
- [33] Kaur, K.; Singh, K.J.; Anand, V., Structural properties of Bi₂O₃–B₂O₃–SiO₂–Na₂O glasses for gamma ray shielding applications, *Radiat. Phys. Chem.* **2016**, 120, 63–72
- [34] Hopper, K.D.; King, S. H.; Lobe, M.E.; TenHave, T. R.; Weaver, J. S., The Breast: In-plane X-ray Protection during Diagnostic Thoracic CT-Shielding with Bismuth Radioprotective Garments, *Radiology* **1997**, 205, 853-858
- [35] Agar, O.; Sayyed, M. I.; Akman, F.; Tekin, H.O.; Kaçal, M.R., An extensive investigation on gamma ray shielding features of Pd/Agbased alloys, *Nucl. Eng. Tech* **2019**, 51, 853-859
- [36] Sayyed, M. I.; Akman, F.; Kaçal, M.R.; Kumar, A., Radiation protective qualities of some selected lead and bismuth salts in the wide gamma energy region, *Nucl. Eng.Tech.* **2019**, 51, 860-866
- [37] Turner, J. E., *Atoms, radiation, and radiation protection*. John Wiley & Sons., New York, U.S.A., 2008, Chapt. 3-5.
- [38] Waly, E. A.; Fusco, M. A.; Bourham, M. A., Gamma-ray mass attenuation coefficient and half value layer factor of some oxide glass shielding materials, *Ann. Nucl. Energy* **2016**, 96, 26–30
- [39] Hubbell, J. H. ; Seltzer, S. M. X-Ray Mass Attenuation Coefficients, Tables of X-Ray Mass Attenuation Coefficients and Mass Energy-Absorption Coefficients

from 1 keV to 20 MeV for Elements $Z = 1$ to 92 and 48 Additional Substances of Dosimetric Interest, *NIST Standard Reference Database 126*, 2004, DOI: <https://dx.doi.org/10.18434/T4D01F>

[40] <http://www.kayelaby.npl.co.uk/atomic-and-nuclearphysics/4-2/4-2-1.html> (accessed 6 June 2019)

[41] Wang, X.; Gong, R.; Li, P.; Liu, L.; Cheng, W., Effects of aspect ratio and particle size on the microwave properties of Fe–Cr–Si–Al alloy flakes., *Mater. Sci. Eng. A* **2007**, 466(1-2), 178-182.

[42] Schnohr, C. S.; Ridgway, M. C., *X-ray absorption spectroscopy of semiconductors.*, Springer Berlin Heidelberg, Germany, 2015

[43] Fan, W. C.; Drumm, C. R.; Roeske, S. B.; Scrivner, G. J. Shielding Considerations for Satellite Microelectronics. *IEEE Trans. Nucl. Sci.* **1996**, 43, 2790.

[44] Pulford, S.; Macarthur Fergusson, M., A textile platform for non-lead radiation shielding apparel, *J. Text.Inst.* **2016**, 107, 1610–1616

[45] Maghrabi, H. A.; Vijayan, A.; Deb, P.; Wang, L., Bismuth oxide-coated fabrics for X-ray shielding, *Text. Res. J.* **2016**, 86, 649–658

Chapter 3. Microwave Absorption and Shielding

Property of Fe-Si-Al Alloy/MWCNT/Polymer

Nanocomposites

3. 1. Introduction

The recent development of electronic and information technology has led to a surprisingly strong change in performance. Electronic devices, such as personal computers and mobile phones, have become more integrated, miniaturized, and lighter. This rapid progress of high-speed processing electronics has necessarily increased the operating frequency of electronics from MHz to GHz or tens of GHz frequency bands [1]. This high-frequency microwave generates unwanted electromagnetic noise, which not only affects the performance of electric devices but also is harmful to humans by raising the temperatures of living tissues and weakening immune functions [2-4]. For these reasons, there is a high demand for electromagnetic interference (EMI) shielding in the GHz range.

Electromagnetic wave shielding materials can be classified into three groups: conductive absorbers, dielectric absorbers, and magnetic absorbers. When an electromagnetic wave is incident on the shielding material, it can be transmitted, reflected, or absorbed. The EMI shielding is done by reflection or absorption of the wave energy [1,5]. Part of the electromagnetic radiation is reflected from the surface

of the conductor, which means that internal fields remain inside, and external fields stay outside [5]. In the magnetic absorbers, varying magnetic fields generate eddy currents that cancel the applied magnetic field. When incident electromagnetic waves are transmitted into magnetic absorbing materials, an induced current is generated, which causes charge displacement in the conductor, thereby relieving the applied field inside to stop the current. Subsequently, the absorbed energy of the incident electromagnetic wave is converted into resistant heat and emitted. The soft magnetic metal powder composite materials have been used for EMI shielding because of their excellent magnetic properties such as large permeability and saturation magnetization [6-10]. However, there are some obstacles that disrupt the magnetization. Especially, the drastic decrease of permeability in the high-frequency range (above 1 GHz) is a barrier to overcome due to Snoek's limitation rule [11]. One way to overcome Snoek's limit is to introduce additional magnetic anisotropies, including shape anisotropy or strain-induced anisotropy [10]. Several studies on the effect of anisotropic morphologies on EMI absorption performance have been reported [12,13]. The ferromagnetic metal particles can be easily flattened into thin flakes by a facile mechanical milling process. Recently, we have fabricated composites with high EMI shielding efficiency in the GHz region using a flat flake-type Fe-Si-Al alloy [10].

To improve the performance of magnetic absorbers, carbonaceous materials were used as dielectric additives to fabricate the hybrid EMI absorbing materials. In particular, carbon nanotubes (CNTs) have attracted a lot of attention because they are conductive fillers with a high aspect ratio and low density and they show a high

dielectric loss [2,9,14]. Several reports have been published on the EMI shielding efficiency of composite materials consisting of magnetic fillers and CNTs [15-18]. Huang et al. investigated the effect of the good impedance matching and strong EM wave attenuation capability in the FeSiAl/MWCNT (2 wt %) composite, which contributes to the excellent microwave absorbing performance of the composite, whereas the composite with excessive addition of MWCNTs (10 wt %) showed much poorer absorbing capability [17].

In our previous study, we have shown that addition of the micro-forged Sendust flakes as the absorbent fillers in the SEBS/PP matrix can significantly increase the EMI shielding efficiency compared to that of Sendust bulk particle composites in the near-field region [10]. In this study, we have designed and manufactured an EM absorber, which combines anisotropic Sendust (magnetic absorption material) and MWCNTs (dielectric absorption material) for shielding effectiveness (SE) enhancement. The hybrid composites are light but exhibit a high SE in a wide frequency range. Contrary to Huang et al.'s results, the effect of MWCNT on the dielectric loss of the composite increases with the MWCNT amount until it reaches 15 phr [17].

3. 2. Experimental Section

3. 2. 1. Materials

Polyolefin elastomer (POE, LC-170 from LG Chemical) and ethyl vinyl acetate (EVA of 45% of vinyl acetate) were used as a polymer matrix. Flake-type Sendust provided by Changsung Co. (Korea) was used for the ferromagnetic metal powder. A multiwalled carbon nanotube (MWCNT, HANOS CM-250, 95 wt % purity from Hanhwa Chem) was selected as the conductive filler. Stearic acid (Aldrich) and NAUGARD-445 (Uniroyal) were used as a lubricant and an antioxidant, respectively. p-Xylene (Daejung Chem) was used as an organic solvent to make the Sendust/MWCNT/polymer suspension, and ethanol (Daejung Chem) was used as an organic solvent to precipitate the Sendust/MWCNT/polymer suspension.

3. 2. 2. Preparation of Sendust/Polymer Composites

Two mixed polymer resins (EVA and POE in the 3:7 ratio) were mixed for 10 min at 100 rpm with flake-shaped Sendust in a twin-screw internal mixer (Haake Rheomix model 600 p) heated to 100 °C. The mixed composite was further processed at 90 °C for 10 min by a roll-milling machine to make the Sendust particles be aligned in the same direction. Finally, the mixed samples were processed for 3 min at 80 °C on a laboratory-scale hot press machine and annealed for 3 min at room temperature.

3. 2. 3. Fabrication of Sendust/MWCNT/Polymer Composites

MWCNTs were first suspended in p-xylene and then sonicated for an hour at 60 °C. The content of MWCNTs was fixed at 0.5 wt %. After stirring for an hour, the MWCNT suspension was poured into a p-xylene/polymer solution (EVA and POE in the ratio 3:7). The mixture was sonicated for 1 h at 60 °C and then stirred for 1 h. Ethanol was added dropwise to the mixture with constant stirring at room temperature. The precipitates were filtered and dried at 80 °C for 24 h in a vacuum oven. The material was then mixed with the flaky Sendust for 10 min in a twin-screw internal mixer preheated to 100 °C at 100 rpm, processed by a roll-milling machine, and pressed and annealed under the same condition as the Sendust/polymer composites. The contents of flaky Sendust particles were fixed at 100 phr (parts per hundred rubber), and the contents of MWCNTs were changed to 5, 10, and 15 phr.

3. 2. 4. Characterization

To measure the near-field power loss, the 50 mm × 50 mm × 1 mm size sample was attached to a microstrip line sample holder, and the holder was connected to a vector network analyzer (VNA, Agilent E8364A) in a frequency range from 45 MHz to 6 GHz. The reflection loss (RL) of the composite was evaluated by the following well-known equations with measured complex permeability and permittivity [10,17],

$$RL \text{ (dB)} = 20 \log_{10} \left| \frac{Z_{in} - Z_0}{Z_{in} + Z_0} \right| \quad (3. 1)$$

$$Z_{in} = Z_0 \sqrt{\frac{\mu_r}{\epsilon_r}} \tanh \left(j \frac{2\pi f d}{c} \sqrt{\mu_r \epsilon_r} \right) \quad (3. 2)$$

where Z_{in} is the absorber input impedance, Z_0 is the impedance of free space, f is the input frequency, d is the thickness of the absorber, μ_r and ϵ_r are the complex

permeability and permittivity of the composites, respectively, j denotes -1 , and c is the velocity of electromagnetic wave in free space. The transmission power loss is determined using the following equation,

$$\text{Power Loss} = \left(\frac{P_{\text{loss}}}{P_{\text{in}}} \right) = \left(\frac{P_{\text{in}} - P_{\text{trans}}}{P_{\text{loss}}} \right) = 1 - (|S_{11}|^2 + |S_{21}|^2) \quad (3.3)$$

where P_{in} is the incident power, P_{loss} is the absorbed power, P_{trans} is the transmitted power, $|S_{11}|^2$ is the reflection coefficient (R), and $|S_{21}|^2$ is the transmission coefficient (T). The power loss corresponding to the electromagnetic absorption loss is proportional to the thickness as follows,

$$\text{Power Loss} \propto d\sqrt{\mu_{\text{re}}f\sigma} \quad (3.4)$$

where μ_{re} is the relative permeability, f is the frequency, d is the thickness of the sample, and σ is the conductivity [19].

On the other hand, the electromagnetic interference shielding performance (SE) in the far-field region was measured by using the coaxial cell method. Complex permeability and complex permittivity were evaluated by measuring the reflection coefficient ($|S_{11}|^2$) and the transmission coefficient ($|S_{21}|^2$) of the specimen backed by a copper strip in a frequency range from 100 MHz to 6 GHz using a vector network analyzer (VNA, Agilent E8364A) [20]. The values of total shielding effectiveness (SE_{total}), absorption SE (SE_{abs}), and reflection SE (SE_{ref}) were determined based on the measured S parameters as follows,

$$R = |S_{11}|^2, \quad T = |S_{21}|^2, \quad A = 1 - R - T \quad (3.5)$$

$$SE_{\text{ref}} \text{ (dB)} = -10 \log_{10}(1 - R), \quad SE_{\text{abs}} \text{ (dB)} = -10 \log_{10}(T/(1 - R)) \quad (3.6)$$

$$SE_{\text{total}} \text{ (dB)} = 10 \log_{10}(P_{\text{in}}/P_{\text{trans}}) = SE_{\text{ref}} \text{ (dB)} + SE_{\text{abs}} \text{ (dB)} \quad (3.7)$$

where R is the reflection coefficient, T is the transmission coefficient, A is the absorption coefficient, P_{in} is the incident power, and P_{trans} is the transmitted power. The morphologies of the samples were observed by scanning electron microscopy (SEM, Jeol JSM-7600F). The fractured sample in the liquid nitrogen was coated with Pt prior to SEM observation.

3. 3. Results and Discussion

3. 3. 1. Morphology of Sendust/MWCNT/polymer composites

As shown in Figure 3. 1, the ball milling process was efficient to convert the bulk-shaped filler into a flake form having a thickness of $\sim 2 \mu\text{m}$ and an average aspect ratio of ~ 80 . Figure 3. 2 shows the morphology of the flake Sendust/MWCNT/polymer composite after roll milling. The flakes were aligned along the roll-milling direction without any free space (Figure 3. 2 (a)). At high magnification (Figure 3. 2 (b)), well-dispersed MWCNTs are observed in the polymer matrix, which are shown as bright thin wire lines.

3. 3. 2. Dielectric Properties

Figure 3. 3 and Figure 3. 4 show the complex permeability and permittivity behaviors of the hybrid composites. Since the MWCNTs have no magnetic property at all, the permeability of the composites was not significantly affected by the addition of MWCNTs but slightly decreased due to the dilution effect, whereas the complex permittivity of the composites was significantly enhanced by the incorporation of MWCNTs because of the high permittivity of MWCNTs. When the content of MWCNTs was 15 phr, the complex permittivity abruptly increased, and the value was two times higher than that of MWCNT 15 phr composites in the entire frequency range (dot line). This improvement in the complex permittivity of the

composites could be explained by Debye's theory. According to Debye's theory [21,22], the imaginary permittivity, ϵ'' , is represented as follows

$$\epsilon'' = \epsilon_p'' + \epsilon_c'' = (\epsilon_s - \epsilon_\infty) \frac{\omega\tau}{1+\omega^2\tau^2} + \frac{\sigma}{\epsilon_0\omega} \quad (3.8)$$

where σ is the electrical conductivity, ω is the angular frequency, τ is the relaxation time, and ϵ_s and ϵ_∞ are the static permittivity and the relative permittivity, respectively [19]. The imaginary part of the complex permittivity comes from contributions of both the relaxation (ϵ_p'') and the conductance (ϵ_c'') [22].

As shown in the electrical conductivity results the addition of MWCNTs formed a local conductive network of the composites once it is higher than the threshold concentration. The increased conductivity of the composite suitably improves the conductive loss. Furthermore, the maximum value (a new resonant peak) appears at near 4.5 GHz for the 15 phr MWCNT added composite, which is ascribed to enhanced interfacial polarization with the addition of MWCNTs [8, 23].

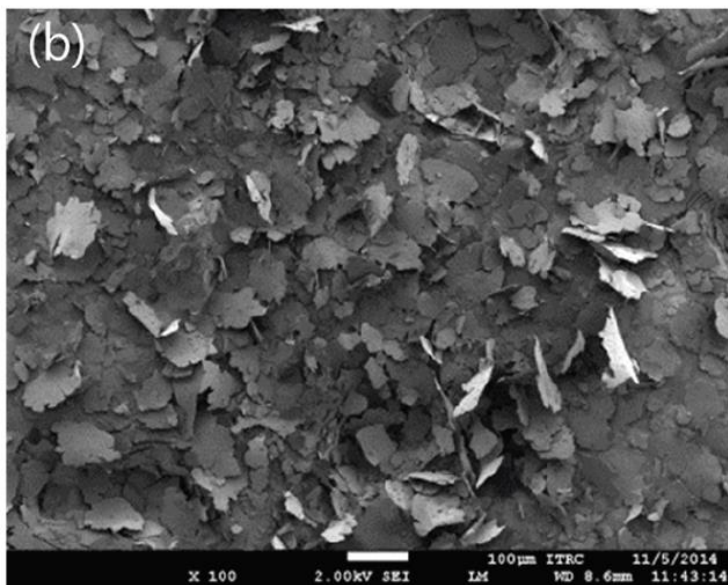
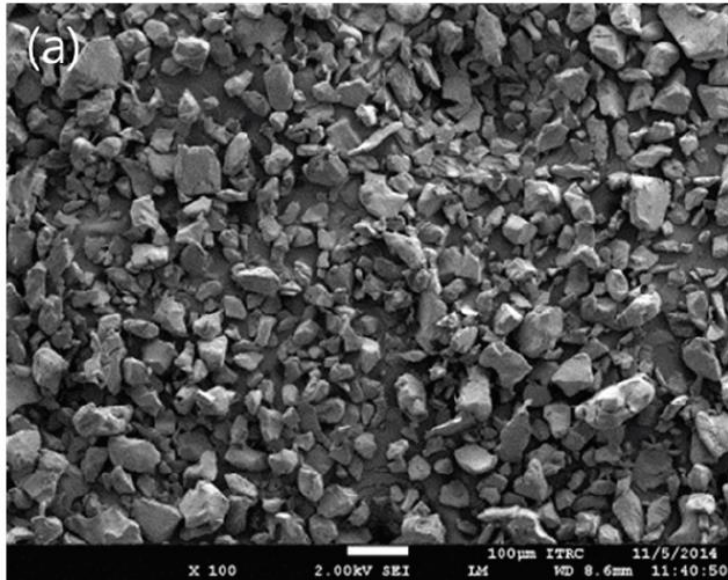


Figure 3. 1. SEM photographs of (a) bulk Sendust (x100 magnification) and (b) micro-forged Sendust (x100 magnification)

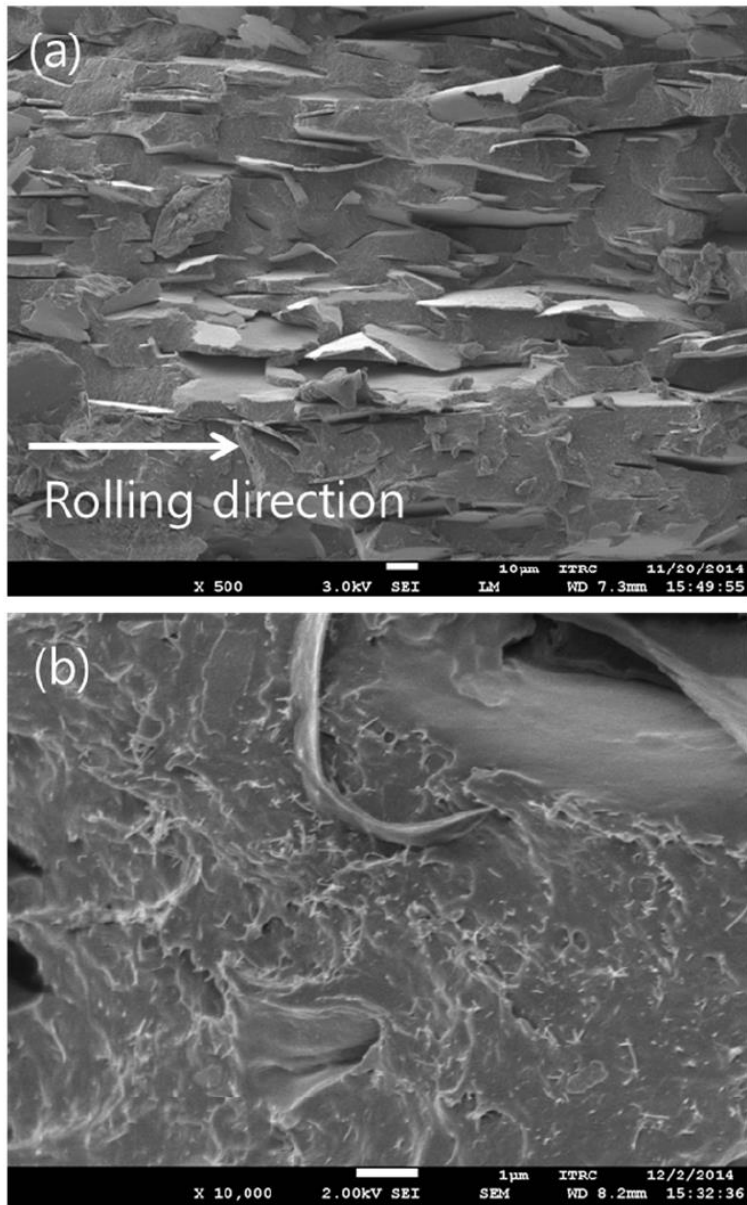


Figure 3. 2. SEM photographs of (a) fractured surface of the composite after roll milling (x500 magnification) and (b) x10000 magnification

3. 3. 3. Microwave Absorption and EMI Shielding Properties

Figure 3. 5 shows the reflection loss (RL) and the power loss of the Sendust/MWCNT/polymer composite in the frequency range from 100 MHz to 6 GHz. The minimum reflection loss value of the Sendust/MWCNT/polymer composite was -17 dB at 4.6 GHz containing 5 phr MWCNTs, whereas the minimum value of composites with 10 phr of MWCNTs at 4.3 GHz was -7 dB and that of 15 phr MWCNTs including the composite at 2.5 GHz was -4.0 dB (Figure 3. 5 (a)). As the content of MWCNT increases, the frequency of the minimum reflection loss shifts to a lower frequency, whereas the reflection loss value decreases. The highest permittivity of composites with 15 phr MWCNTs (largest amount) indicates superior absorbing properties through dissipation of the EM energy into heat (dielectric loss). In contrast to the result of the complex permittivity, the lower the MWCNT content, the better the reflection loss performance. To explain this behavior, we need to consider impedance matching, which plays an important role in determining the EMI absorption properties of materials [12-17]. When an electromagnetic wave encounters a discontinuity (boundary surface of the shielding material), it may be reflected or absorbed depending on the impedance difference at the boundary. If the air impedance differs greatly from the intrinsic impedance of the shielding material, most of the electromagnetic wave is reflected, and very little is transmitted across the boundary [9,25-27]. For microwave absorbers, the relationship between matching thickness and matching frequency is given by [18]

$$f = c (1 + \tan^2 \delta_\mu / 8) / (4d\sqrt{\mu_r \epsilon_r}) \quad (3. 9)$$

where μ_r and ϵ_r are the complex permeability and permittivity, respectively, f is the frequency, d is the thickness of composites, c is the velocity of electromagnetic waves in free space, and $\tan \delta_\mu$ is the magnetic loss tangent. As shown in eq 3.9, the impedance matching condition could be altered by variation of the permeability and the permittivity of composites. Since the thickness of the composites was constant (~ 1 mm), the matching frequency decreased by increasing the complex permittivity. The complex permittivity for impedance matching could be calculated if the values of the complex permeability in each frequency range are known. By using an electromagnetic characteristic parameter map generated in earlier studies, we were able to find the best condition corresponding to zero reflection [28]. The composite containing 100 phr Sendust and 5 phr MWCNTs was close to meet the necessary conditions for zero reflection. Sendust/MWCNT/polymer composites with 10 or 15 phr MWCNTs failed to satisfy the zero-reflection condition. Thus, a stronger reflection of the incident microwaves occurred at the interface of the composite containing 5 phr MWCNTs. Under general conditions, however, more dipoles are formed as the amount of MWCNTs increases. The increase of the dipoles thus contributes to increasing the dielectric loss [29,30]. Similar behavior of the reflection loss was reported when a conductive material was mixed with a magnetic absorber [6,17,18]. Therefore, the electromagnetic wave attenuation efficiency at the measured frequency range can be increased with the MWCNT amount.

The power loss in Figure 3. 5 (b) corresponding to electromagnetic absorption loss is proportionate to permeability and conductivity. As the addition of mixed MWCNTs in the composite increases the permittivity (Figure 3. 4), so does the

power loss. The specimen containing 100 phr Sendust and 5 phr MWCNTs lost 30 % power at 1 GHz, and composites containing 10 and 15 phr MWCNTs lost 40 and 60 % of power at the same frequency. These power loss values of the ternary (Sendust/MWCNT/polymer) composites are higher than that of the one containing Sendust only. The power loss value at 1 GHz and the density of composites containing different types of EMI absorbers are summarized in Table 3. 1. The density of the specimen containing 100 phr Sendust was 1.51 g/cm^3 , which managed to absorb 26 % of the energy at 1 GHz. The density of 15 phr MWCNTs was 1.05 g/cm^3 , and this filler could absorb 30% of the energy at 1 GHz. Though the density of the Sendust/MWCNT/polymer composite containing 100 phr of Sendust flakes and 15 phr of MWCNTs was only 1.75 g/cm^3 , it was surprisingly able to absorb 60 % energy over the same frequency range. The specific power loss (SPL), which is the power loss value divided by the material density, is evaluated to compare the overall absorbing attenuation of different materials. The ternary hybrid composite shows a higher SPL value than the other two composites containing MWCNT only and Sendust only. This means that a composite lighter than the one containing only Sendust but highly effective and better than that containing only MWCNT can be made by uniformly mixing Sendust and MWCNT with the polymer matrix. The power loss of Sendust plus 15 phr MWCNTs containing the specimen is similar to that of the one containing 400 phr flaky Sendust [10]. Thus, it is possible to produce a composite that is lightweight but has excellent electromagnetic wave absorption characteristics in the near field region.

The performance of a microwave absorber containing MWCNTs in the far-field can be evaluated by the EMI SE. Figure 3. 6 shows the EMI shielding effectiveness (EMI SE). The ternary composites (Sendust/MWCNT/polymer) showed better shielding effectiveness than that of the composite containing Sendust only, and the EMI SE improved with the amount of MWCNTs in the composite. The total SE could be represented by the sum of absorption loss and reflection loss (eq 3.7). Though the reflection loss of the hybrid composites decreased with the amount of MWCNTs due to the frequency mismatch, the addition of MWCNTs in the hybrid composites was effective to increase the overall EMI shielding performance because of the enhanced dielectric loss contribution by the high permittivity of the composites.

Huang et al. prepared flaky Fe–Si–Al alloy/MWCNT composites without the roll-milling process. The composite containing 2 wt % of MWCNTs achieved the minimum RL value of -42.8 dB at 12.3 GHz at a film thickness of 1.9 mm. When the MWCNT content was increased to 10 wt %, the minimum RL value was -6 dB at 5.2 GHz. The current result of the minimum RL value for the 10 phr MWCNT specimen is -7.5 dB at 5.5 GHz. The difference can be attributed to the difference in anisotropy of magnetic fillers and the additional roll-milling process. Our magnetic fillers have 4 times larger aspect ratio than theirs (aspect ratio ~ 20) [17]. In addition, the magnetic filler could be aligned by the roll-milling process along the milling direction without voids. The well-dispersed MWCNTs located between the magnetic fillers could construct the conductive network more easily [17,18]. A comparison of our complex permittivity data with Huang et al.'s evidently demonstrates that the

longer flake has superior permittivity: the maximum complex permittivity of composites is about 4 times higher than Huang et al.'s. Although less MWCNT (2 wt %) was used in Huang et al.'s study and higher reflection loss at high frequency (-42.8 dB at 12.3 GHz) was recorded, its reflection loss at the frequency between 1 and 6 GHz was much less than that in the current study, and their film thickness was 1.9 mm, twice thicker than the current film.

All these results illustrate the importance of the proper amount of MWCNT, which should be decided depending on the operating (or electromagnetic interference shielding) frequency range of the device. However, the current study evidently demonstrates that the ternary EMI shielding film is useful for electromagnetic wave absorption and EMI shielding. It also provides a viable method to prepare an efficient multilayer EMI shielding film in which a layer containing a small amount of MWCNT, for example, 2 wt %, for the optimum RL loss at high frequency and a layer containing an appropriate amount of flaky Sendust and MWCNTs for the optimum power loss are alternatively laminated [31-33]. This is currently under way and will be reported in the future.

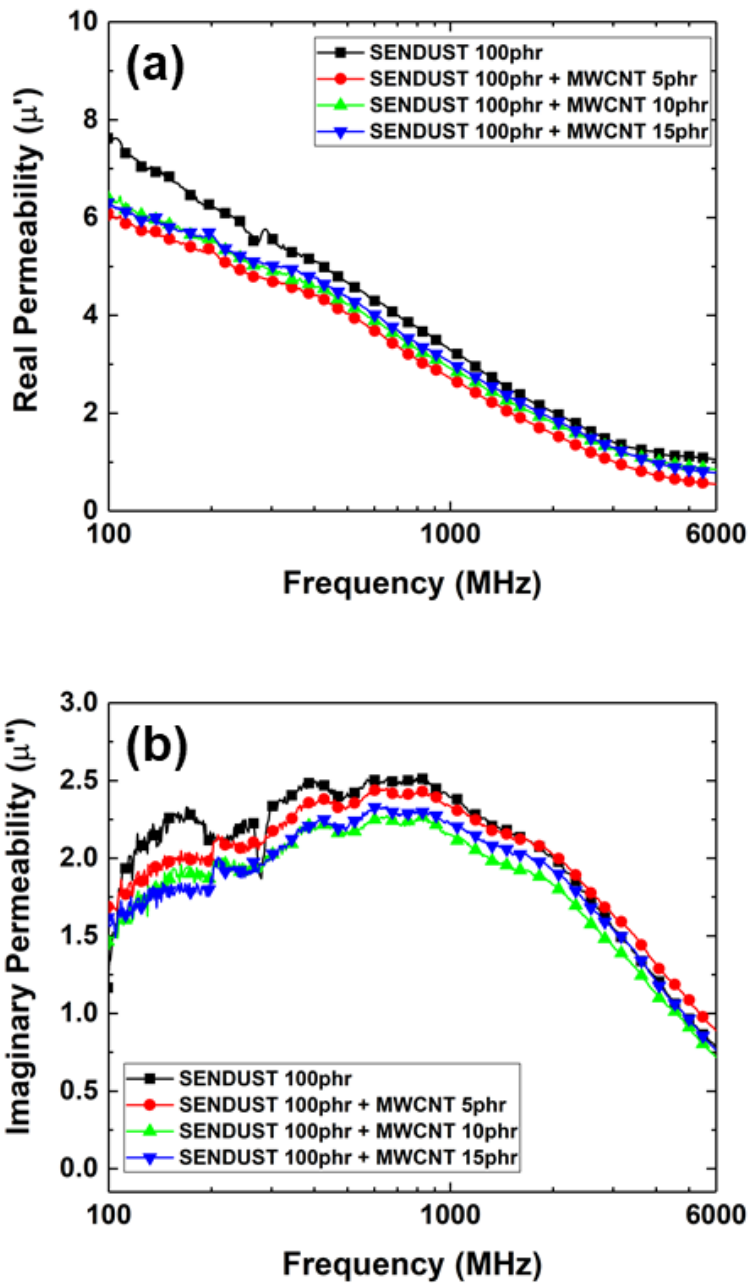


Figure 3. 3. Complex permeability of Sendust/MWCNT/polymer composites: (a) real permeability and (b) imaginary permeability

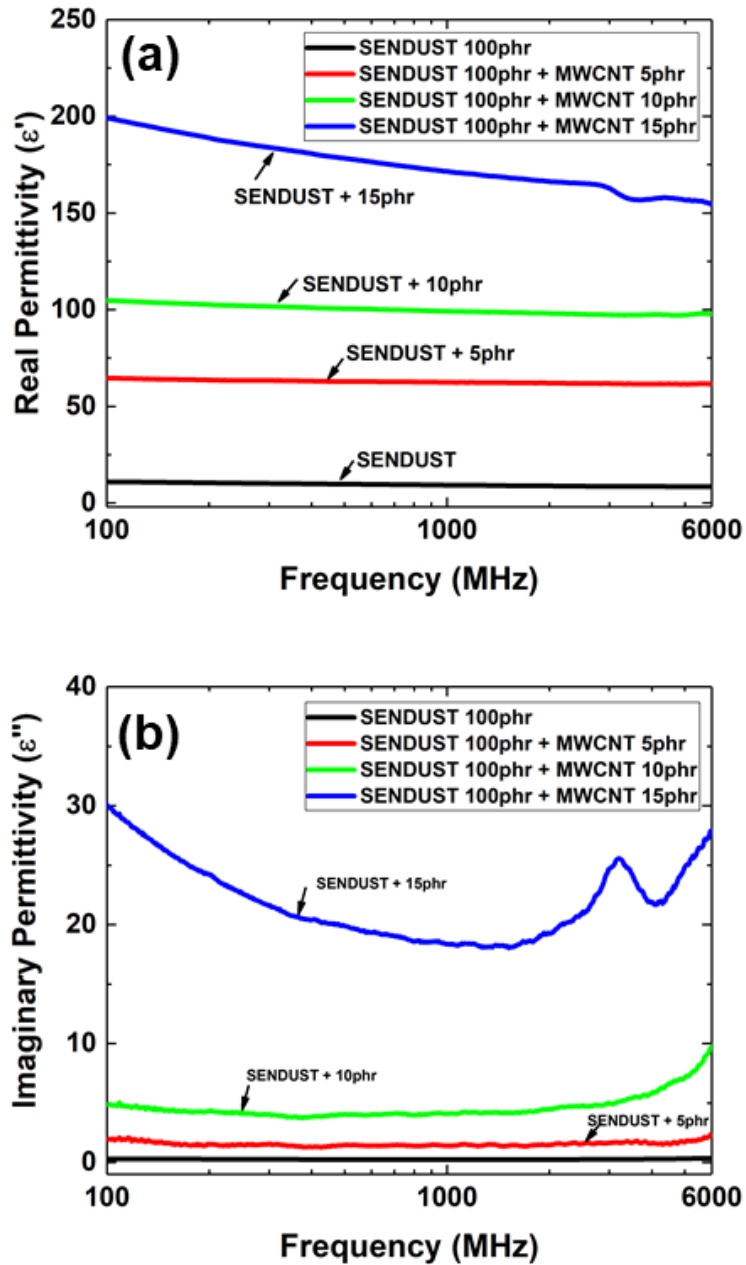


Figure 3. 4. Complex permittivity of Sendust/MWCNT/polymer composites: (a) real permittivity and (b) imaginary permittivity

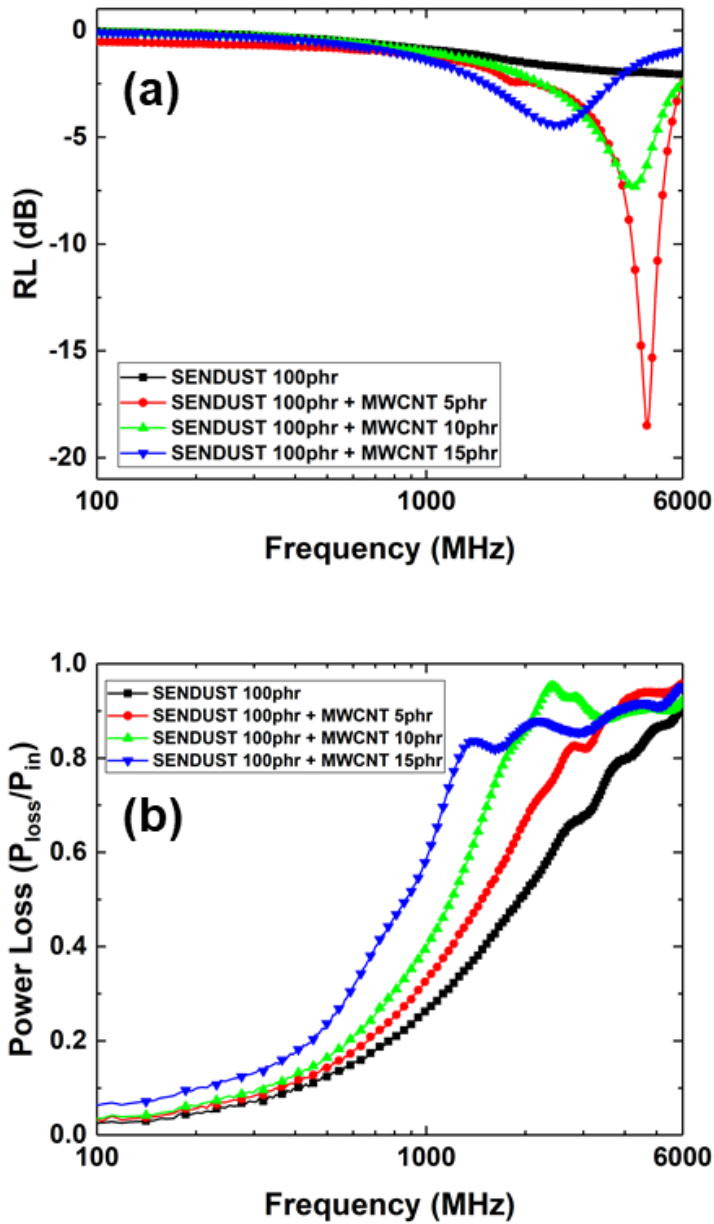


Figure 3. 5. Electromagnetic absorption performance of Sendust/MWCNT/polymer composites: (a) reflection loss and (b) power loss

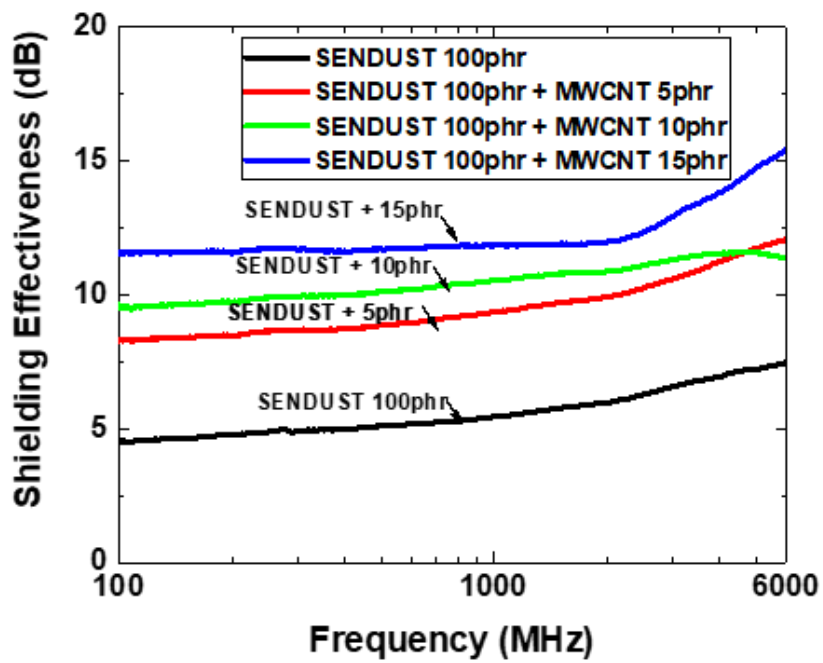


Figure 3. 6. EMI shielding effectiveness (SE) of the Sendust/MWCNT/polymer composites

Table 3. 1. Power Loss, Density, and Specific Power Loss of Magnetic, Dielectric, and Hybrid Composites

Sample	Density (g/cm ³)	Power Loss (@ 1 GHz)	Specific Power Loss (cm ³ /g)
Flake Sendust 100 phr	1.51	0.265	0.175
MWCNT 15 phr	1.05	0.305	0.290
Flake Sendust 100 phr + MWCNT 15 phr	1.75	0.596	0.340

3. 4. Conclusions

Sendust/MWCNT/polymer composites were prepared by applying a solution blending method and using an internal mixer. The incorporation of MWCNTs with micro-forged Sendust could significantly improve the electromagnetic wave absorption and EMI shielding efficiency compared to Sendust/polymer composites. The loss mechanism of the Sendust/MWCNT/polymer composites consists of both magnetic loss and dielectric loss. Added MWCNTs could improve the permittivity of composites, causing a large increase in dielectric loss. The composite containing 100 phr Sendust and 15 phr MWCNTs absorbed 60 % of the energy at 1 GHz and demonstrates a wide shielding frequency range. On the other hand, the reflection loss value reached -17 dB at 4.6 GHz in the composite containing 5 phr MWCNTs. The total SE value increased with the amount of MWCNT due to the enhanced dielectric loss caused by increased permittivity and improvement in conductivity of the ternary composites. In addition, the composite produced by this approach has the practical advantage of being able to produce light and thin microwave absorption materials with excellent EMI shielding efficiency in a wide frequency range.

References

- [1] Geetha, S.; Satheesh Kumar, K.; Rao, C. R.; Vijayan, M.; Trivedi, D., EMI shielding: Methods and materials—A review. *J. Appl. Polym. Sci.* **2009**, 112 (4), 2073-2086.
- [2] Park, D. H.; Lee, Y. K.; Park, S. S.; Lee, C. S.; Kim, S. H.; Kim, W. N., Effects of hybrid fillers on the electrical conductivity and EMI shielding efficiency of polypropylene/conductive filler composites. *Macromol. Res.* **2013**, 21 (8), 905-910.
- [3] Shen, B.; Zhai, W.; Tao, M.; Ling, J.; Zheng, W., Lightweight, multifunctional polyetherimide/graphene@ Fe₃O₄ composite foams for shielding of electromagnetic pollution. *ACS Appl. Mater. Interfaces* **2013**, 5 (21), 11383-11391.
- [4] Joseph, N.; Singh, S. K.; Sirugudu, R. K.; Murthy, V. R. K.; Ananthakumar, S.; Sebastian, M. T., Effect of silver incorporation into PVDF-barium titanate composites for EMI shielding applications. *Mater. Res. Bull.* **2013**, 48 (4), 1681-1687.
- [5] Cho, H.; Kim, A.; Kim, S.; Namgung, J.; Kim, M.; Lee, G., Study of electromagnetic wave-absorbing materials made by a melt-dragging process. *Phys. Status Solidi A* **2004**, 201 (8), 1942-1945.
- [6] Lee, B. Y.; Lee, J. W.; Yun, Y. C.; Jeong, I. B.; Moon, J. H. In Electromagnetic properties of silver coated iron-based alloy powders prepared by chemical reduction method, Materials science forum, *Trans Tech Publ.* **2007**; pp 1449-1452.

- [7] Liu, X.; Guo, H.; Xie, Q.; Luo, Q.; Wang, L.-S.; Peng, D.-L., Enhanced microwave absorption properties in GHz range of Fe₃O₄/C composite materials. *J. Alloys Compd.* **2015**, 649, 537-543.
- [8] Han, M.; Yin, X.; Ren, S.; Duan W.; Zhang, L.; Cheng, L. Core/shell structured C/ZnO nanoparticles composites for effective electromagnetic wave absorption, *RSC Adv.* **2016**, 6, 6467-6476
- [9] Li, N.; Huang, Y.; Du, F.; He, X.; Lin, X.; Gao, H.; Ma, Y.; Li, F.; Chen, Y.; Eklund, P. C., Electromagnetic interference (EMI) shielding of single-walled carbon nanotube epoxy composites. *Nano Lett.* **2006**, 6 (6), 1141-1145.
- [10] Oh, K.; Hong, S. M.; Seo, Y., Effect of crosslinking reaction on the electromagnetic interference shielding of a Fe–Si–Al alloy (Sendust)/polymer composite at high frequency. *Polym. Adv. Technol.* **2014**, 25 (11), 1366-1370.
- [11] Dionne, G. F., Magnetic relaxation and anisotropy effects on high-frequency permeability. *IEEE Trans. Magn.* **2003**, 39 (5), 3121-3126.
- [12] Wang, X.; Gong, R.; Li, P.; Liu, L.; Cheng, W., Effects of aspect ratio and particle size on the microwave properties of Fe–Cr–Si–Al alloy flakes. *Mater. Sci. Eng. A.* **2007**, 466 (1), 178-182.
- [13] Qiao, L.; Wen, F.; Wei, J.; Wang, J.; Li, F., Microwave permeability spectra of flake-shaped FeCuNbSiB particle composites. *J. Appl. Phys.* **2008**, 103 (6), 063903.
- [14] Cao, M. S.; Song W. L.; Hou, Z. L.; Wen, B.; Yuan, J. The effects of temperature and frequency on the dielectric properties, electromagnetic interference

shielding and microwave-absorption of short carbon fiber/silica composites. *Carbon* **2010**, 48, 788-796

[15] Che, R.; Peng, L. M.; Duan, X. F.; Chen, Q.; Liang, X., Microwave absorption enhancement and complex permittivity and permeability of Fe encapsulated within carbon nanotubes. *Adv. Mater.* **2004**, 16 (5), 401-405.

[16] Yang, Q.; Liu, L.; Hui, D.; Chipara, M., Microstructure, electrical conductivity and microwave absorption properties of γ -FeNi decorated carbon nanotube composites. *Composites Part B* **2016**, 87, 256-262.

[17] Huang, L.; Liu, X.; Chuai, D.; Chen, Y.; Yu, R., Flaky FeSiAl alloy-carbon nanotube composite with tunable electromagnetic properties for microwave absorption. *Sci. Rep.* **2016**, 6, 35377.

[18] Zhang, W.; Xu, Y.; Yuan, L.; Cai, J.; Zhang, D., Microwave absorption and shielding property of composites with FeSiAl and carbonous materials as filler. *J. Mater. Sci. Technol.* **2012**, 28 (10), 913-919.

[19] Nicolson, A. M.; Ross, G. F., Measurement of the intrinsic properties of materials by time-domain techniques. *IEEE Trans. Instrum. Meas.* **1970**, 19 (4), 377-382.

[20] Wen, B.; Cao, M.; Lu, M.; Cao, W.; Shi, H.; Liu, J.; Wang, X.; Jin, H.; Fang, X.; Wang, W.; Yuan, J. Reduced Graphene Oxides: Light-Weight and High-Efficiency Electromagnetic Interference Shielding at Elevated Temperature. *Adv. Mater.* **2014**, 26, 3484-3489.

[21] Wen, B.; Cao, M.-S.; Hou, Z.-L.; Song, W.-L.; Zhang, L.; Lu, M.-M.; Jin, H.-B.; Fang, X.-Y.; Wang, W.-Z.; Yuan, J., Temperature dependent microwave

attenuation behavior for carbon-nanotube/silica composites. *Carbon* **2013**, 65, 124-139.

[22] Cao, W.-Q.; Wang, X.-X.; Yuan, J.; Wang, W.-Z.; Cao, M.-S., Temperature dependent microwave absorption of ultrathin graphene composites. *J. Mater. Chem. C* **2015**, 3 (38), 10017-10022.

[23] Yang, R. B.; Kuo, W. S.; Lai, H. C., Effect of carbon nanotube dispersion on the complex permittivity and absorption of nanocomposites in 2–18 GHz ranges. *J. Appl. Polym. Sci.* **2014**, 131 (21), 40963.

[24] Kim, J.; Kwak, S.; Hong, S. M., Lee, J. R.; Takahara A.; Seo, Y. Nonisothermal Crystallization Behaviors of Nanocomposites Prepared by In Situ Polymerization of High-Density Polyethylene on Multiwalled Carbon Nanotubes. *Macromolecule* **2010**, 43, 10545-10553

[25] Kim, S. W.; Yoon, Y. W.; Lee, S. J.; Kim, G. Y.; Kim, Y. B.; Chun, Y. Y.; Lee, K. S., Electromagnetic shielding properties of soft magnetic powder–polymer composite films for the application to suppress noise in the radio frequency range. *J. Magn. Magn. Mater.* **2007**, 316 (2), 472-474.

[26] Lim, K.; Kim, M.; Lee, K.; Park, C., Electromagnetic wave absorption properties of amorphous alloy-ferrite-epoxy composites in quasi-microwave band. *IEEE Trans. Magn.* **2003**, 39 (3), 1836-1841.

[27] Kim, S.-S.; Kim, S.-T.; Yoon, Y.-C.; Lee, K.-S., Magnetic, dielectric, and microwave absorbing properties of iron particles dispersed in rubber matrix in gigahertz frequencies. *J. Appl. Phys.* **2005**, 97 (10), 10F905.

- [28] Musal, H.; Hahn, H., Thin-layer electromagnetic absorber design. *IEEE Trans. Magn.* **1989**, 25 (5), 3851-3853.
- [29] Al-Saleh, M. H.; Sundararaj, U., Electromagnetic interference shielding mechanisms of CNT/polymer composites. *Carbon* **2009**, 47 (7), 1738-1746.
- [30] Feng, Y.; Qiu, T.; Shen, C., Absorbing properties and structural design of microwave absorbers based on carbonyl iron and barium ferrite. *J. Magn. Magn. Mater.* **2007**, 318 (1), 8-13.
- [31] Micheli, D.; Vricella, A.; Pastore, R.; Marchetti, M. Synthesis and electromagnetic characterization of frequency selective radar absorbing materials using carbon nanopowders. *Carbon* **2014**, 77, 756-774
- [32] Ye, F.; Zhang, L.; Yin, X.; Liu, Y.; Cheng, L.; The improvement of wave-absorbing ability of silicon carbide fibers by depositing boron nitride coating. *Appl. Surf. Sci.* **2013**, 611-616
- [33] Zhang, L.; Yang, B.; Teng, J.; Lei, J.; Tan, D.; Zhong, G.; Li, Z. Tunable electromagnetic interference shielding effectiveness via multilayer assembly of regenerated cellulose as a supporting substrate and carbon nanotubes/polymer as a functional layer. *J. Mater. Chem. C* **2017**, 5, 3130-3138

Chapter 4. Enhancement of Interfacial Adhesion between Polymer Pairs and Fracture Mechanism

4. 1. Introduction

The adhesion at heterogeneous polymer–polymer interfaces plays a key role in the mechanical properties of polymer lamination, coatings, welding, composite adhesion, and particle sintering [1-9]. Since most polymer pairs are thermodynamically immiscible, the interdiffusion of molecules at their interface is insufficient to create entanglements with the interfacial chains [4-6]. As a result, the interfacial adhesion strength is quite weak. A useful method for the strengthening of weak interfaces is the addition of a graft or block copolymer that enables entanglements of the interfacial polymer chains [7-10]. Diblock copolymers are quite effective entanglement agents, but random copolymers or graft copolymers that make multiple excursions across the interface can also be effective [11-14]. Another useful method for improving the adhesion strength is to use a reactive compound that can generate in situ graft or block copolymers at the interface [1,15,16]. Produced in situ block or graft copolymers at the interface during the annealing form entanglements with other matrix molecules on both sides. This approach provides an alternative to costly block copolymer synthesis, which is not possible for some immiscible polymer pairs [5,7].

In a reactive compound-added system, the interfacial adhesion strength depends

on many parameters [7-16]. It has been found that the adhesion strength (fracture toughness) between two heterogeneous (immiscible) polymers whose interface is reinforced by in situ block or graft copolymers increases with the annealing (bonding) time, passes through a peak, and then reaches a plateau [1,5]. The annealing temperature dependence is similar to time dependence in that the adhesion strength passes through a maximum at a particular temperature [7,15]. The appearance of a maximum in the fracture toughness does not arise because of variation in the amount of the copolymer formed at the interface or because of the hindrance of diffusion of the functionalized polymer to the interface [16-18]. The ion-beam irradiation of surface molecules under oxygen environment has been found to produce some functional groups down to a shallow depth of an amorphous polystyrene surface or a semi-crystalline polypropylene surface [18-20]. The resulting surface functional groups were found to react with the amine end groups of the polyamide (nylon 6) [15,21,22]. The fracture toughness of these systems was found to follow a similar track: it increased with the bonding time, peaked at a particular time and temperature, then decreased to reach a steady plateau. This dependence on the annealing (bonding) time and/or temperature seems to be a common feature of such systems regardless of the polymer structure (crystalline or amorphous) [15]. As long as the molar mass of the reacted copolymer is sufficiently high to form entanglements with both matrix polymers and the number density of the copolymer is sufficiently high, the fracture mechanisms will have these typical features that are independent of the crystallinity of the polymer.

Such variations in the fracture toughness with the bonding time and temperature

have been attributed to the presence of two different failure mechanisms in these systems; adhesive failure at the interface and cohesive failure in the bulk beneath the interface due to chain disengagement [1,7]. These failure mechanisms become relevant under different conditions, as follows. When the annealing reaction starts, the concentration of the in situ graft copolymers increases to enhance the adhesion strength with the annealing time and temperature. At the same time, nonfunctionalized molecules leave the highly energetic interface [1,4]. This molecular diffusion leads to chain disengagements with other copolymer chains generated in situ at the interface [22,23]. The cohesive strength then decreases with the annealing time because of reduced engagements between chains; this effect occurs more rapidly at a higher bonding temperature. Although this explanation is very convincing, it has not been experimentally proved so far. Here, we provide direct experimental evidence for the diffusion of nonfunctionalized molecules from the interface into the bulk of the matrix, which causes the cohesive failure in the polymer having lower strength.

4. 2. Experimental Section

4. 2. 1. Materials

The materials used in this experiment were a commercial polyamide 6 (Nylon 6, PA6) and polystyrene (PS). The polyamide was supplied by Kolon, KN171. The

weight average molecular weight, M_w , was 8.5×10^5 g/mol, and the polydispersity index was 3.5. The polystyrene was GPPS-150K from Kumho petrochemicals. The weight average molecular weight, M_w , was 2.8×10^5 g/mol, and the PDI index of PS was 2.4. The poly(styrene-co-maleic anhydride (PSMA)) contained 7 wt% maleic anhydride group, which was supplied by Aldrich in pellet form without any additives. The weight average molecular weight of the PSMA was 2.24×10^5 g/mol. The physical properties of the materials used in this study are listed in Table 4.1.

Blending of PS and PSMA was performed in an internal mixer at 200 °C. DSC thermograms showed that the PSMA and PS/PSMA blend had almost the same melting behavior as pure PS. Therefore, we believe that phase separation between PS and PSMA didn't occur in PS/PSMA blend. The strips had predetermined dimensions were made by compression molding at 180 °C and at 240 °C for PS (PS/PSMA), PA6, respectively.

4. 2. 2. Ion beam irradiation and plasma treatment

The system for surface treatment consists of a conventional plasma treatment system and a low energy ion beam irradiation system with reactive gas feeding system. In this system, surface was irradiated by low energy ion beam and plasma, simultaneously. The first process was that low energy Ar^+ ion beam irradiation on the surface of PS strips with reactive O_2 gas. The flow rate of Ar gas was 2 sccm, and O_2 gas was 3 sccm. The irradiation process was performed under 10^{-4} torr. For the second process, we treated O_2 plasma on the specimens. A radio frequency

(13.56MHz) plasma was generated by RF power source (RF5S-PF power products Inc.) and the plasma power was 100W. The O₂ gas flow rate was fixed at 10 sccm. And in the third process, we combined two processes, ion beam treatment and plasma treatment. First, the PS samples were irradiated by low energy Ar⁺ ion beam without reactive gas and then irradiated PS samples were treated by O₂ plasma immediately. Pre-ion beam irradiation time was 180 seconds and treatment time of plasma was between 60sec, 600sec to check how the treatment time affected the extent of functionalization.

4. 2. 3. Adhesion Process

The modified PS strips (or the blended PS strip) was combined with PA 6 strips in an airtight mold. And the mold was heated in the compression molder under slight pressure. The temperature was varied between 180 °C and 230 °C and bonding time was from 30 min to 120 min. The mold was cooled down to room temperature in the air. All bonded samples were stored in a desiccator for 24 hours before measuring the fracture toughness.

4. 2. 4. Measurement of Fracture Toughness

The fracture toughness of bonded samples was measured by using an asymmetric double cantilever beam test. This test has been shown to be quite reliable measurement for the fracture toughness of a polymer interface. Details of this test

are shown in Figure 4. 1.

The following equation derived by Boucher et al. based on calculations by Kanninen, whose assumption was that the finite elasticity of the materials ahead of the crack tip required correction factors for small crack length was used, [11]

$$G_c = \frac{3\Delta^2}{8a^4} \frac{E_{PS}h_{PS}^3 E_{PA6}h_{PS}^3}{E_{PS}h_{PS}^3 \alpha_{PA6}^2 + E_{PA6}h_{PA6}^2 \alpha_{PS}^2} \quad (4. 1)$$

where E and h denotes the elastic modulus and the thickness of materials, respectively, and Δ is the thickness of the blade (0.25mm), α_i , is the correction factor for material and is given by

$$\alpha_i = \left\{ 1 + 1.92 \left(\frac{h_i}{a} \right) + 1.22 \left(\frac{h_i}{a} \right)^2 + 0.39 \left(\frac{h_i}{a} \right)^3 \right\} / \left\{ 1 + 0.64 \left(\frac{h_i}{a} \right) \right\} \quad (4. 2)$$

To minimize the effect of G_{ii} mode in the fracture toughness, we fabricated all our samples with a predetermined thickness ratio, h_{PS}/h_{tot} of 2/3. The ADCB test yields reliable values if two precautions are taken. Asymmetric conditions of samples and critical energy release rate must be calculated in the proper limit. The former case, it is known that varying the ratio of thicknesses changes the amount of G_{ii} component in the fracture process. In PP and PA6 system, the energy release rate is much larger than the observed minimum obtained for h_{PP}/h_{tot} of 0.62. In PS and PA6 system, the thickness ratio of 0.67 shows the maximum fracture toughness value in ADCB test, we chose the thickness ratio of h_{PS}/h_{tot} is 2/3. The crack length a was measured by optical microscope (Olympus).

4. 2. 5. Characterization

The chemical components of modified PS were analyzed by using X-ray photoelectron spectroscopy (XPS). The XPS spectra were recorded Kratos AXIS spectrometer ($h\nu = 1.5\text{keV}$). Base pressure is 5×10^{-10} torr, take-off angle is 90 degree and irradiation time is about 30min to 1hours. The spectra were referenced to the main components of the C1s peaks of PS at a binding energy of 285eV. The O1s peaks was referenced to the C=O peak at 531.9eV, the C-O peak at 533.1eV and the COO peak at 533.3eV. The peak deconvolution process was operated by using the software (Origin)

Tri-layer films were prepared for the diffusion measurements by solution spin-coating and floating methods. The thickness of each layer is shown in Figure 1. Real-space depth profiles were recorded by using dynamic secondary-ion mass spectrometry (DSIMS, ATOMIKA SIMS 4000 spectrometer) [23]. An incident 4 keV, 30 mA beam of oxygen ions was focused onto a $200 \mu\text{m} \times 200 \mu\text{m}$ area for the detection of negative secondary ions. The angle of incidence was 45° . To ensure stable sputtering during the measurements, a PS buffer layer was laminated onto the d-PS/PSMA mixed layer by using the floating technique [24-26]. A gold layer with a thickness of 20 nm was sputter-coated onto the tri-layer surface to prevent charging the specimen during the DSIMS measurements [26].

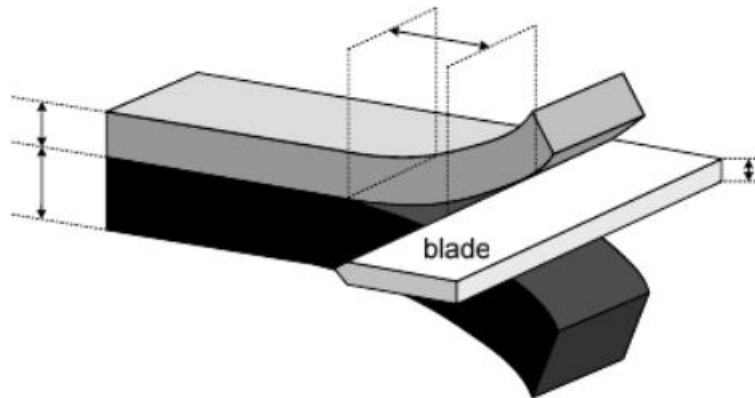
4. 2. 6. Lamination with Aluminum film and barrier properties

By using surface modification method of the polymer, we fabricated aluminum film laminated clay/polymer film to examine the potential for the gas barrier film. In general, the gas barrier film was fabricated by deposition of aluminum oxide or silicon oxide. In this experiment, poly(m-xylylene adipamide) (MXD6) was used as polymer matrix, Cloisite 93A was used as the filler. The filler content was fixed at 5 wt%, and the thickness of the composites film was about 70 μm and the size were 10 cm x 10 cm.

The surface treatment was performed using oxygen plasma, the power was 120 W and treatment time was 10 minutes. After surface treatment of clay/MXD6 nanocomposites, the modified nanocomposites were combined with aluminum film (6 μm , 12 μm). Then, clay/MXD6 film and aluminum film were laminated at 150 °C using a compression mold. The water vapor permeability was measured according to ASTM F2622 standard. The permeation values were recorded at 23 °C and 50 % relative humidity by a Mocon Permatran-W 3/33 (Minneapolis, USA).

Table 4. 1. Various properties of polymeric materials

Materials	Properties	ASTM	Value
Polystyrene	Tensile Strength	D638	540 kg/cm ²
	Tensile Modulus	D638	1.5 GPa
	Elongation at Break	D638	3.5 %
	Flexural Strength	D790	890 kg/cm ²
	Flexural Modulus	D790	33000 kg/cm ²
	Impact Strength (IZOD)	D256	14.7 J/m
	T _g		104.5 °C
Polyamide 6	Tensile Strength	D638	820 kg/cm ²
	Tensile Modulus	D638	2.05 GPa
	Elongation at Break	D638	150 %
	Flexural Strength	D790	1300 kg/cm ²
	Flexural Modulus	D790	30000 kg/cm ²
	Impact Strength (IZOD)	D256	74 J/m
	T _m		220 °C
PS-g-MA	Impact Strength (IZOD)	D256	11.0 J/m
	Hardness	D785	108
	Softening Point	D1525	118 °C
	T _g		120 °C
	Density		1.1 g/cm ³



Δ : thickness of blade

a : crack length ahead of the blade

h_A : thickness of material A

h_B : thickness of material B

Figure 4. 1. Schematic illustration of asymmetric double cantilever beam (ADCB) test [11].

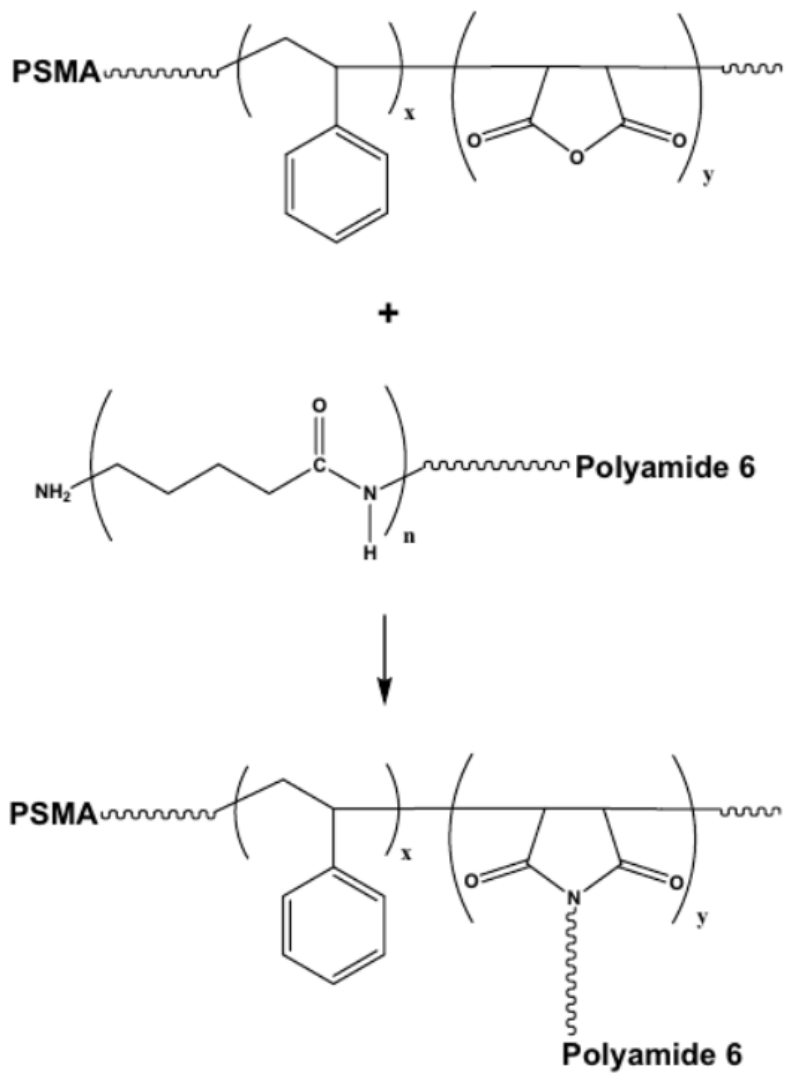


Figure 4. 2. Schematic representations of structures and reaction between PSMA and PA6

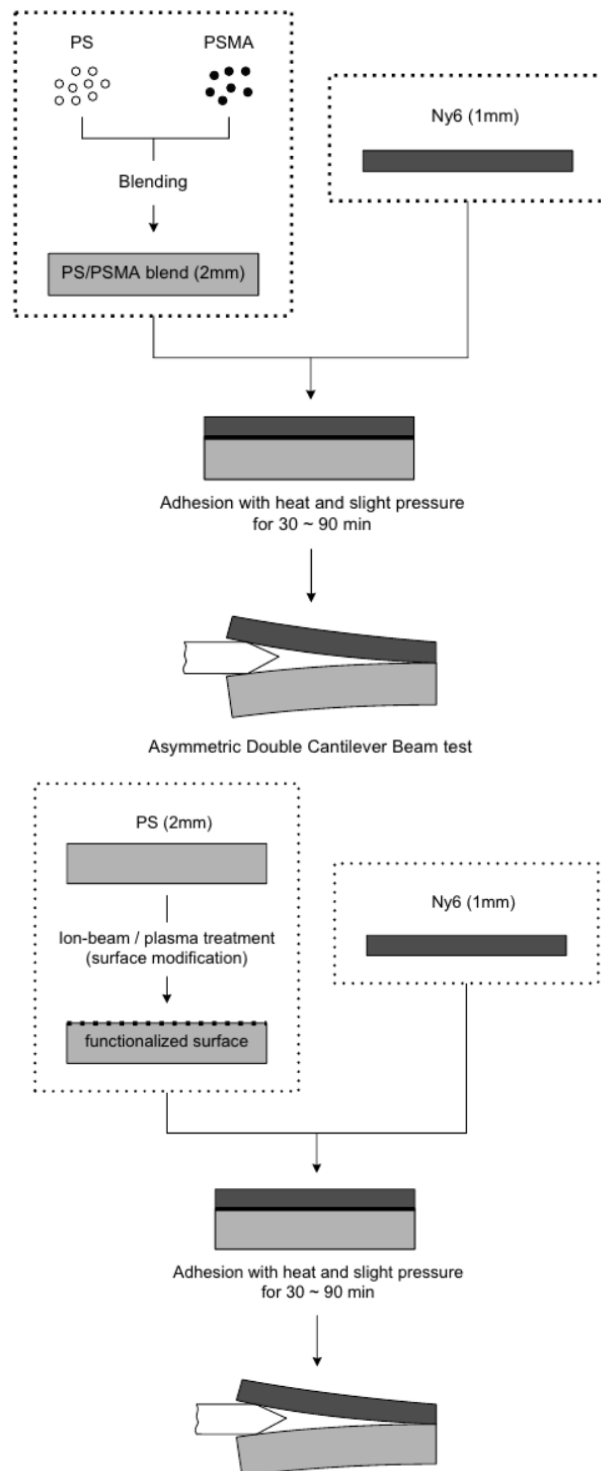


Figure 4. 3. Schematic illustrations of experiments

4. 3. Results and Discussion

4. 3. 1. Adhesion Strength with Bonding Time and Temperature

In a general reactive compatibilization system for immiscible amorphous/crystalline polymer pairs, the reactive components added in amorphous polymer side and the end group of crystalline polymers easily react to form covalent bonds during processing. Our system of PS/PSMA blend and PA6 (polyamide 6) is also like that. The maleic anhydride groups in the blend and the amine end groups of PA6 reacts each other. The schematic representation of structures and reaction between PSMA and polyamide 6 was shown in Figure 4. 2. Through the reaction, PA6 chains were grafted with PSMA chain containing maleic anhydride groups and the copolymer was formed at the interface.

The schematic procedure of specimen preparation and adhesion test of PS/PSMA and PA6 was shown in Figure 4. 3. After the procedure, ADCB test for the measurement of adhesion strength was performed.

The fracture toughness versus the annealing time is plotted in Figure 4.4. Some facts are interesting to note: First, the introduction of PSMA resulted in an improvement in the fracture toughness of the interface. Second, the fracture toughness increased with the annealing temperature, reached its maximum value at a temperature of 200 °C, and then decreased with increase of bonding temperature. Third, this system has optimum annealing time of 90 minutes, and annealing temperature of 200 °C having the highest value of fracture toughness, although it

was less obvious in other cases. Fourth, the fracture toughness increased after some induction time of annealing due to the wetting process between the polymer pairs.

The chemical reaction occurring at the interfaces of reactively blended polymer pairs can be controlled by either diffusion or reactions. Cho and Li insisted that the critical areal densities of the copolymer at the interface increased with annealing temperature until they reached a saturation point at which reactions no longer occurred near the interface due to the steric hindrance caused by the high areal densities. Seo and Ninh concluded that their system of PP/PPMA blend and Ny6 was also diffusion-controlled. Our results agree with that. Actually, either process of diffusion or reaction, could govern the interfacial reaction kinetics, especially in the initial stage of adhesion. The parameters affecting the rates of diffusion and reaction are the bonding temperature and the initial concentration of the functional groups on the polymer surface. For an exact analysis, the effects of the annealing temperature and the initial concentration were needed. In this study, however, we investigate the effects of the annealing temperature and the bonding time at a constant annealing temperature since we cannot precisely control the number of functional groups on the polymer surface.

Figure 4.5 shows the fracture toughens as a function of the annealing temperature at various bonding time. The slope increases with the annealing temperature up to 200 °C and the maximum growth rate having the highest fracture toughness is appeared at 90min of bonding time. The fracture toughness shows a peak at 200 °C and then decrease with higher annealing temperature. In 30 min of short annealing time, the fracture toughness was less than about 50 J/m², and a low annealing

temperature of 180 °C leads to an interfacial toughness of under about 100 J/m². It was for this reason that a low temperature and short annealing time did not give enough wetting process.

In this system, the non-wetting processes doesn't cause the diffusion problem of reactive blending system because the surface modification modify the surface only (less than a hundred nanometers). The IB+O₂, PLASMA, IB+PLASMA processes introduced the functional groups which contain oxygen on the surface. So, this system can be regarded as the reaction-controlled system. The produced hydroxyl groups, carbonyl groups and carboxyl groups reacted with the amine groups of polyamide 6 at the interface. Through the reaction, polyamide 6 was grafted with polystyrene and copolymer was formed at the interface. According to the several recent researches, the interface is occupied with functionalized polymers and is in a reaction-controlled regime.

Figure 4.6, 4.7 and 4.8 shows the variation of fracture toughness between the surface modified PS and PA6 with bonding temperature and time. From these data, we could conclude every surface modification process is effective to enhance the interfacial adhesion. Because the fracture toughness of neat PS and PA6 is about several J/m². The fracture toughness increased with bonding time as the reaction between functionalized PS and the amine groups of PA6 proceeded. As mentioned above, the interface will be occupied fully by graft copolymer formed by the reaction. Then, we could expect the fracture toughness will be saturated at specific value in long bonding time. However, the interfacial strength reached a plateau or decreased after the peak of maximum fracture toughness.

In the variation of fracture toughness with bonding temperature, the fracture toughness increased with the annealing temperature, reached a maximum value at a temperature of 210 °C, and then it decreased with increase of bonding temperature regardless of the three different surface modification processes. The maximum fracture toughness (average value) in IB+O₂ is 227.75 J/m², and that of plasma treatment process is 286.04J/m² and finally that of the combined process has 309.39 J/m².

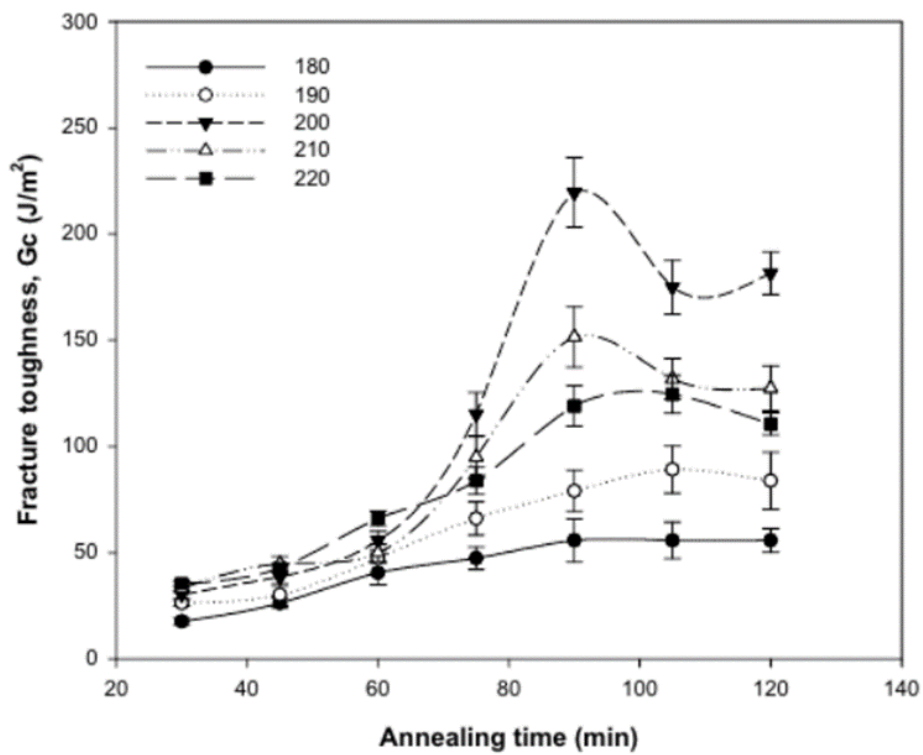


Figure 4. 4. Variation of the fracture toughness of PS(+PSMA)/PA6 interface with the annealing time.

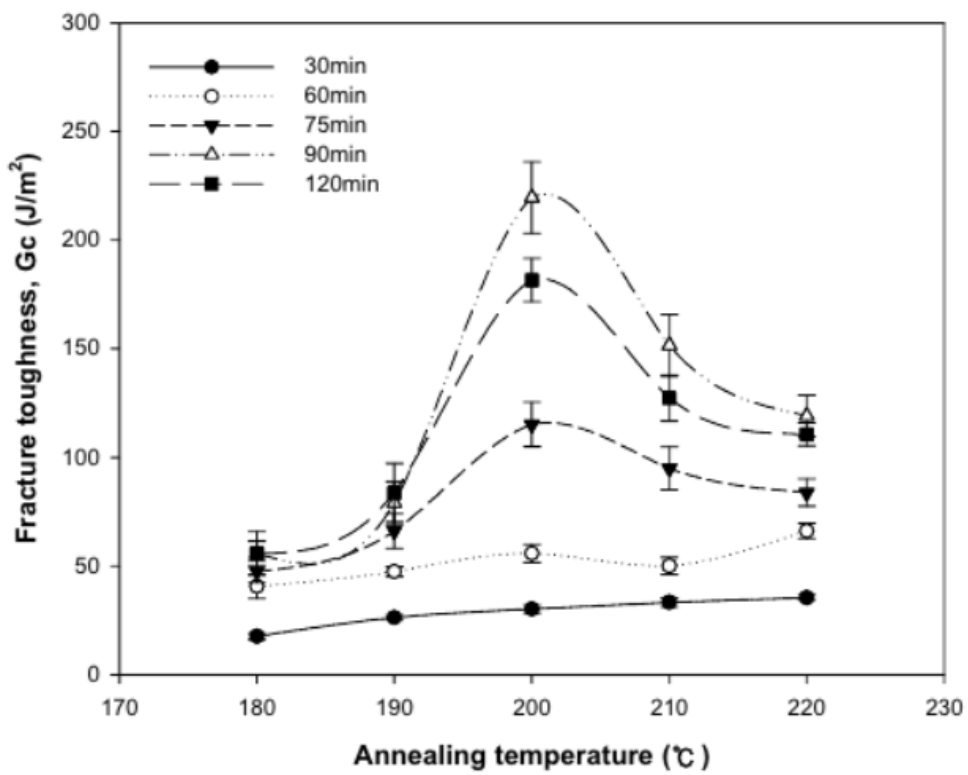


Figure 4. 5. Variation of the fracture toughness of PS(+PSMA)/Ny6 interface with the annealing temperature.

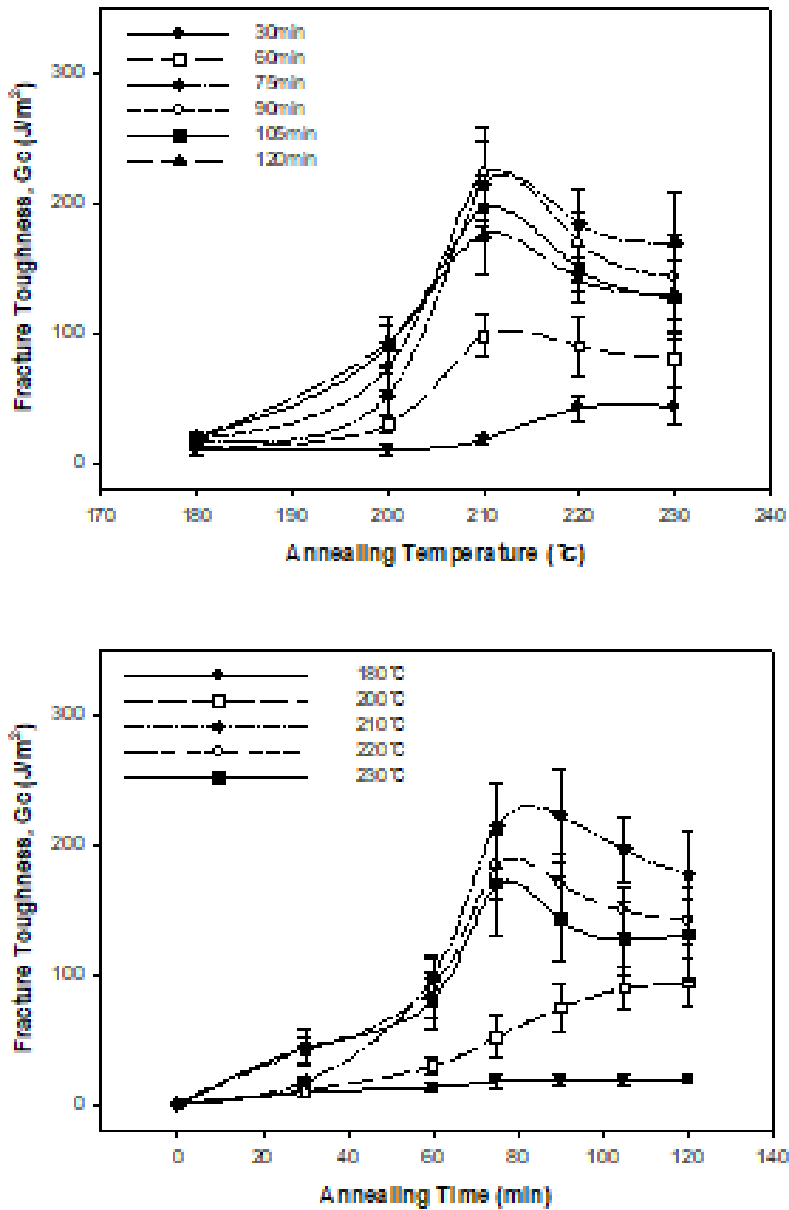


Figure 4. 6. Variation of the fracture toughness between modified PS by ion beam irradiation under reactive oxygen gas and PA6 with (a) bonding temperature and (b) bonding time.

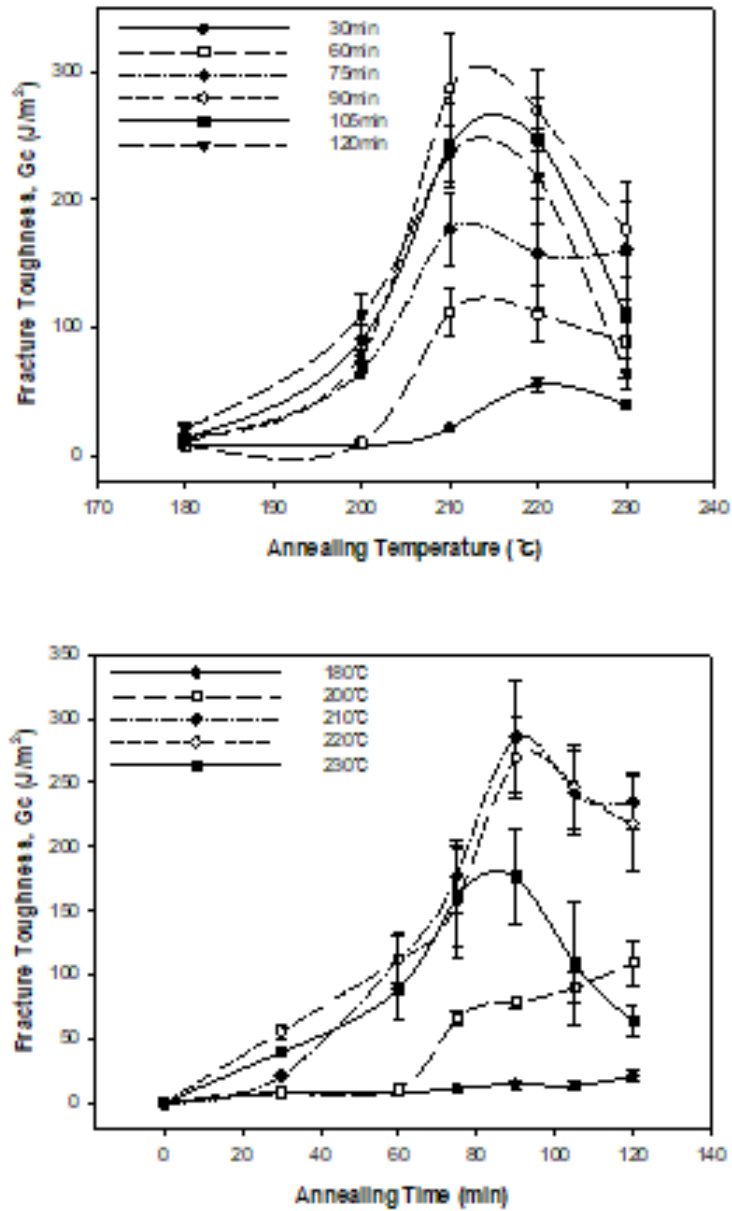


Figure 4. 7. Variation of the fracture toughness between modified PS by oxygen plasma treatment and PA6 with bonding temperature (a), and bonding time (b)

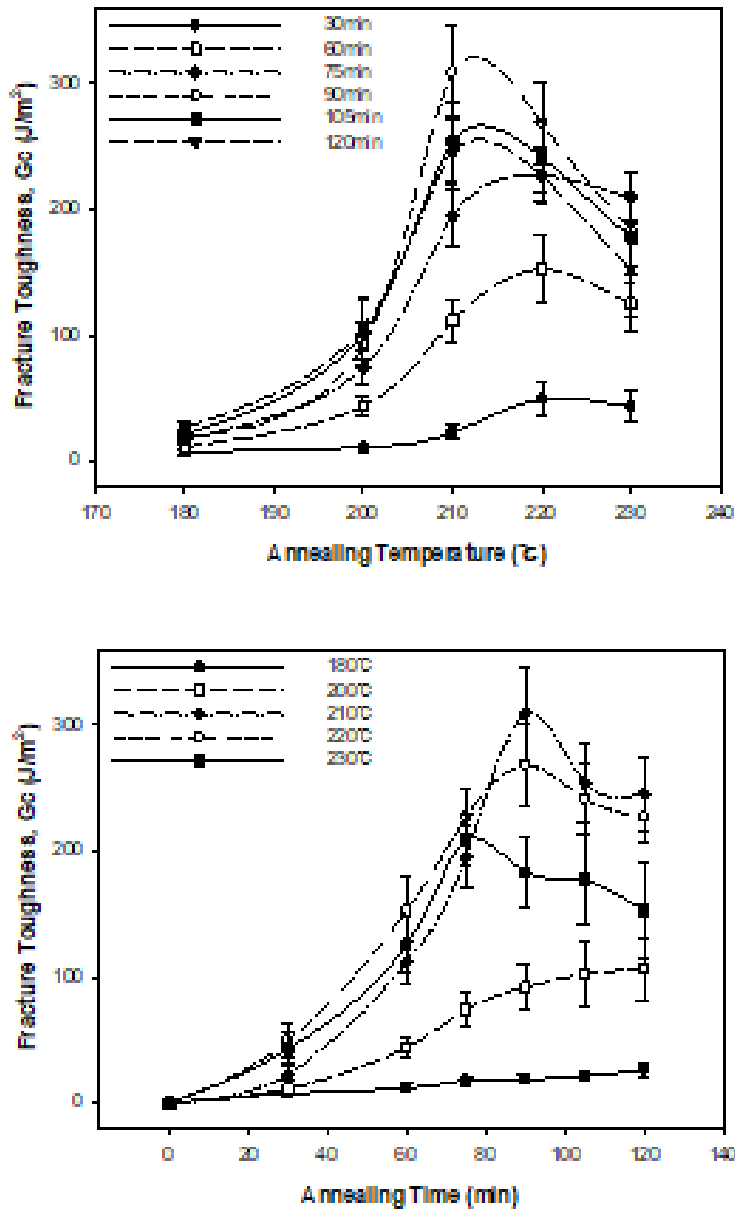


Figure 4. 8. Variation of the fracture toughness between modified PS by plasma treatment after ion beam irradiation without reactive gas and PA6 with bonding temperature (a), and bonding time (b)

4. 3. 2. Fracture Mechanism

The occurrence of maxima in the fracture toughness was ascribed to the occurrence of different failure mechanisms. When the block or graft copolymers are not long enough to be fully entangled with the matrix molecules at both sides, the fracture at the interface is preceded by chain pullout. Because the in-situ graft copolymers produced at the interface have high molecular weights to be fully entangled with matrix polymers at both sides, the fracture occurs by the chain scission even when the areal density of copolymers at the interface is low [23]. As the annealing proceeds, the areal density of graft copolymers goes over some critical values to enable the adhesive strength strong enough to withstand the fracture stress. After a long reaction time has passed, the cohesive strength in the PS side decreased because other normal PS molecules diffuse away from the interface to form a microphase separation between the polystyrene and PSMA molecules. If the cohesive strength becomes lower than the adhesive strength, failure occurs due to cohesive failure between the molecules at or near the interface and other PS molecules below the interface. Then, the fracture will be preceded by the cohesive failure in the weaker polymer side (PS). After some time, both the adhesive strength and cohesive strength reach steady-state values. Hence, a maximum occurs in the variation of the fracture toughness with time. Whether the maximum peak appears or not depends on the relative magnitudes of the adhesive strength and the cohesive strength [18].

Depending on the intrinsic failure energy of the interface, failure prefers the

weaker of the two. This explanation is partly verified in experimental study using X-ray photoelectron spectroscopy (Table 4.2 and Table 4.3). By checking the elemental compositions on the cleaved surfaces, we confirmed that the crack propagated into the PS phase in a long-time annealed specimen because of the very strong adhesion at the interface. The amount of nitrogen on the Ny6 side decreased at first with the bonding time, implying a coverage of PS molecules on this side, and then increased. The initial decrease is obviously attributed to the increased number of PS molecules transferred to the Ny6 side with bonding time. The later time dependence was ascribed to the movement of other PS chains prementioned above. As the reaction time proceeded, the cohesive strength became weaker and fewer chains were transferred to the Ny6 side. Therefore, the fracture toughness at first increased with the annealing time because of the enhanced adhesive strength due to interfacial reactions, passed a peak, and then decreased to a plateau value because of a critical surface coverage by the interacting molecules and a reduced cohesive strength. The adhesive strength also increased with the temperature due to more reactions, but the cohesive strength became lower because of disengagement of PS molecules with the chains at or near the interface. When the annealing temperature was not high enough to induce many reactions at the interface, the adhesion strength was lower than the cohesive strength through the whole process. The failure mechanism, then, followed only the adhesive failure, and no maximum peak appeared [1].

The movement of PS molecules from the interface was directly checked by tracing the deuterated PS molecule movement. Figure 4.10(a)–(e) shows the depth profiles for CH⁻ (blue line), CD⁻ (red line), and carbon ions (black line), with a depth

resolution of ~ 10 nm after $t = 0, 30, 90, 300,$ and 900 min of annealing at 120 °C. This low temperature (120 °C) was chosen to see the time evolution of the d-PS molecules movement because the PS molecule diffusion occurs very quickly at the high annealing (bonding) temperatures. The intensity of the carbon ion, C^{-} , is nearly constant within the tri-layer, indicating that steady-state etching evidently occurs during the measurements. Thus, the abscissa of the etching time can be simply converted to the depth from the surface. The measured concentration profiles for CD^{-} are slightly broadened due to an atomic mixing effect [24, 25]. After correction of this small atomic mixing effect, the actual interfacial thickness can be obtained [26]. It is obvious in Figure 4.10 that more d-PS molecules diffuse into the buffer PS layer side even at a low temperature of 120 °C as the annealing time increases. The reaction between PSMA and Ny6 does not proceed rapidly at this temperature, i.e., the adhesion strength increased insignificantly at this temperature, but it is apparent that d-PS molecules do diffuse into the bulk of the low-potential region. The diffusion behavior of polymers strongly depends on the temperature and on their molecular weight [21,26]. Figure 4.10(f),(g) shows the CD^{-} concentration profile changes after annealing for 30 and 90 min at 150 °C. After 90 min, the CD^{-} concentration profile has almost reached a steady state at this higher temperature, indicating that chemical reactions take place fast at the PS/PSMA and Ny6 interface and diffusion reaches almost to equilibrium.

By using the method of Whitlow and Wool, the interfacial thickness was calculated [27]. Figure 4.11 shows the evolution of the interfacial thickness profile for the h-PS/d-PS interface vs annealing time. The interfacial thickness increases

proportionately with $t_{1/2}$ (t = annealing time), suggesting that the diffusion is Fickian (Figure 4.8) [2,17]. By fitting the concentration profile to the deconvoluted concentration profile $C(x)$ of CD⁻ along the direction normal to the surface, the diffusion coefficient, D , can be obtained as [24]

$$C(x) = \frac{1}{2} \left\{ 1 - \operatorname{erf} \left(\frac{-x}{\sqrt{a^2 + 4Dt}} \right) \right\} \quad (4.3)$$

where a is the instrumental function ($a = 5.5$ nm), t is the annealing time, and x is the distance from the interface (Figure 4.10(h)). The D values at 120 °C were evaluated using eq 4.3 and are listed in Table 4.4. The D value of d-PS ($M_n = 1.8 \times 10^5$ g/mol) at 120 °C is 2.67×10^{-17} cm²/s [27,28]. Although the annealing temperature is low (120 °C), all D values for the present system are greater than this value, which is ascribed to the exothermic reaction occurring at the interface. D goes through a maximum around 90 min and then drops. This result is consistent with the results of the fracture toughness measurement (Figure 4.4) that pass through their peak values at this annealing time and higher annealing temperatures (180, 200, 210, and 220 °C). Therefore, the reaction occurs most actively around this time. The reaction constant values do not vary with the annealing temperature as much as the diffusion coefficient values [21,23,29]. As the annealing time increases, more reactions occur to produce more graft copolymers, which increase the chemical potential at the interface and saturate the interface after the peak time.

The time scale of the disengagement is the reptation time of the molecules

$$\tau_M = \frac{\langle R \rangle^2}{3\pi^2 D} \quad (4.4)$$

where R is the root-mean-square end-to-end distance and D is the diffusion coefficient [24,30]. The reptation times (or disengagement times) of the

nonfunctionalized PS (d-PS) molecules were calculated using the diffusion coefficient values (Table 4.4). All annealing times are longer than the chain disengagement (reptation) times except for an annealing time of 30 min: this annealing time is shorter than the reptation (disengagement) time. Thus, the chain does not show the Fickian diffusion at this time (Figure 4.8). As more diffusion occurs, more nonfunctionalized molecules (d-PS) are disengaged from the produced copolymers or PSMA molecules at the interface (Figure 4.12(a)). In the early stages of annealing, the buildup of the copolymers produced by the reaction is not sufficient to cover the interface, which induces the movement of functionalized molecules (PSMA) to the interface. As the annealing proceeds, the buildup of graft copolymers limits the replenishment of functionalized molecules to the interface. A longer annealing time means that the reaction rate determining step at the polymer–polymer interface changes from the reaction-controlled regime to the diffusion-controlled regime. The reaction therefore slows down for long annealing times but diffusion of nonfunctionalized PS molecules (d-PS) occurs more actively, and thus they can escape from the high-energy interface. The diffusion of nonfunctionalized molecules (d-PS) from the interface is promoted because of the increase in the potential at the interface as annealing time increases. The diffusion of the chains from the interface causes the cohesion of the d-PS molecules with the in-situ graft copolymer molecules formed at the interface to decrease. Thus, the normal molecules' disengagement from the molecules at the interface (graft copolymers or PSMA molecules) leads to a reduced cohesive strength (Figure 4.12(b)). The fracture toughness then initially increases due to the increased concentration of the reacted copolymer at the interface

but later decreases due to the movement of chains, which results in the cohesive failure.

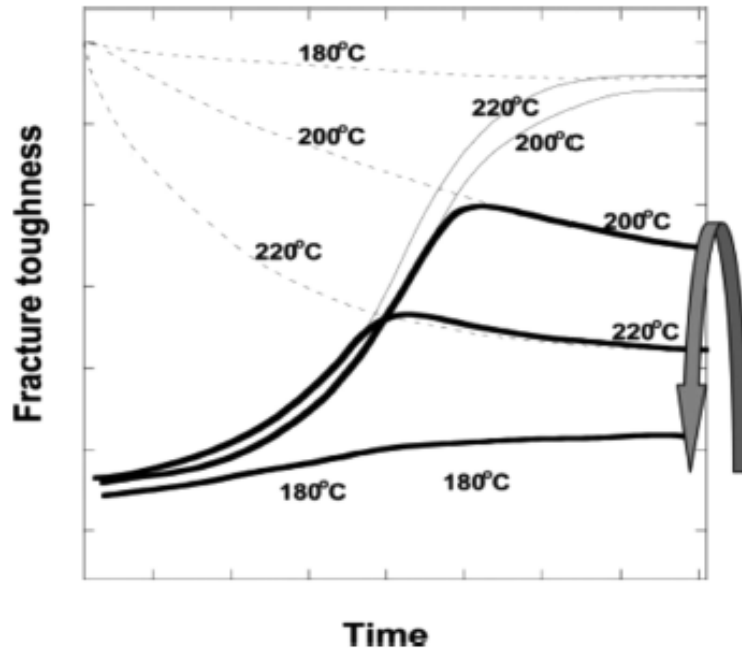


Figure 4. 9. Schematic representation of the locus of failure of PS-(+PSMA)/Ny6 interface. When the adhesive strength (solid line) is lower than cohesive strength (dashed line) the failure occurs first through the adhesive failure. But after the former becomes larger than the latter, the failure occurs through the cohesive failure. Bold lines implicate the overall path of the failure with time at different temperatures. The arrow indicates the fracture toughness variation with the bonding temperature after a long time (90 min)

Table 4. 2. Elemental compositions of fractured PS and PA6 surfaces measured by XPS (variation of annealing time)

Annealing Time (at constant bonding temp of 200°C, min)	PS	Ny6	
	% O	% N	% O
30	9.76	9.37	12.88
60	6.96	5.49	9.57
90	4.25	4.62	8.66
120	5.33	5.92	10.17

Table 4. 3. Elemental compositions of fractured PS and PA6 surfaces measured by XPS (variation of annealing temperature)

Annealing Temperature (at constant bonding time of 90min, °C)	PS	Ny6	
	% O	% N	% O
180	9.54	9.45	12.52
190	8.11	8.49	9.59
200	4.25	4.62	8.66
220	6.21	6.64	8.87

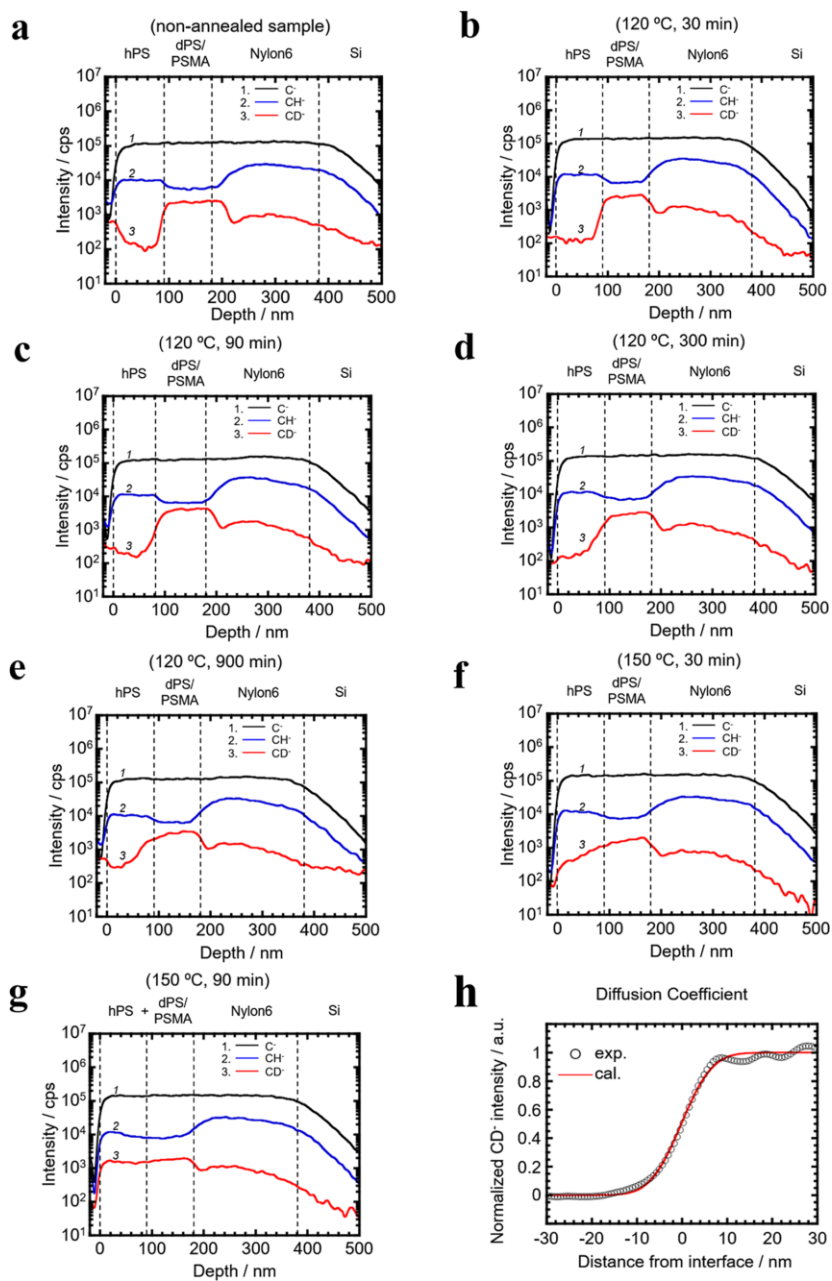


Figure 4. 10. Depth profiles: (a) nonannealed, (b) annealed at 120 °C for 30 min, (c) annealed at 120 °C for 90 min, (d) annealed at 120 °C for 300 min, (e) annealed at 120 °C for 900 min, (f) annealed at 150 °C for 30 min, and (g) annealed at 150 °C for 900 min; (h) calculation of the diffusion coefficient and experimental measurement (annealed at 120 °C for 90 min).

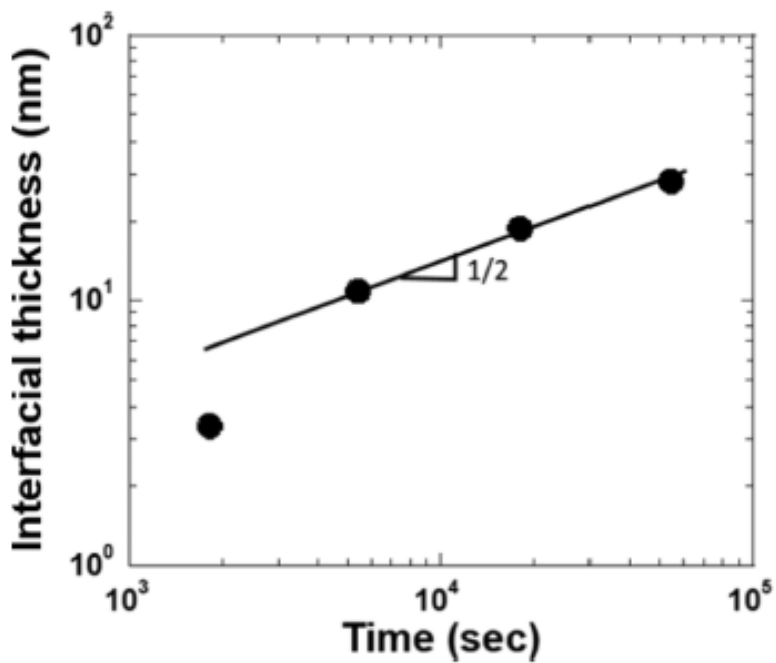


Figure 4. 11. Double-logarithmic plot of interfacial thickness versus annealing time for the (h-PS/d-PS) bilayer annealed at 393 K (120 °C). The slope of 1/2 is drawn in the context of the Fickian diffusion as a guide.

Table 4. 4. Diffusion Coefficients for d-PS, Interfacial Thickness and Reptation Time

Annealing Temperature (°C)	Annealing Time (min)	Diffusion Coefficient (cm ² /s)	Interfacial Thickness (nm)	Reptation Time (s)
120	30 (1800 s)	$(4.5 \pm 0.3) \times 10^{-17}$	3.4 ± 0.8	3.17×10^3
120	90 (5400 s)	$(6.9 \pm 0.2) \times 10^{-17}$	10.9 ± 0.1	2.07×10^3
120	300 (18000 s)	$(5.2 \pm 0.1) \times 10^{-17}$	18.7 ± 3.4	2.74×10^3
120	900 (54000 s)	$(3.2 \pm 0.1) \times 10^{-17}$	25.4 ± 1.3	4.46×10^3

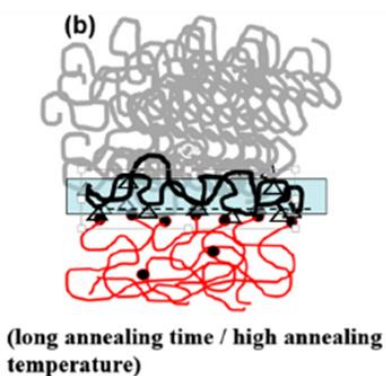
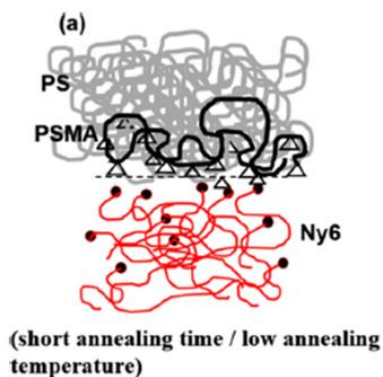


Figure 4. 12. Schematic representation of the variation of the interfacial reactions with the reaction time: (a) early period, (b) later period.^{1,16} Black lines are PSMA chains. Light gray lines are PS chains, and red lines in the lower side are Ny6 chains (Δ = succinic anhydride groups of PSMA and \bullet = amine groups of Ny6). Due to the entanglement of the graft copolymers with other Ny6 and PS molecules on both sides of the interface, the adhesion strength increases with annealing time. For longer annealing times, more graft copolymers are formed at the interface. However, the diffusion of the PS chains from the interface induces cohesion decrease of the PS molecules with the in situ graft copolymer molecules formed at the interface or other entangled PS molecules (shaded region in (b)). The cohesive strength then decreases with the annealing time, and this occurs faster at the higher bonding temperature.

4. 3. 3. Barrier properties of laminates film

The clay/MXD6 nanocomposites shows the high oxygen gas barrier properties due to the high aspect ratio and the rigid platelet of the clay in the polymer matrix. However, water vapor permeability was poor as shown in Table 4. 6. Poly(m-xylene adipamide) is one of the crystalline polyamide. MXD6 contains an aromatic ring and has lower hydrophilicity unlike other aliphatic polyamides. But due to the hydrophilic characteristic of the amide linkage in the polymer, it has relatively high water permeability in spite of the high crystallinity.

In order to overcome this limitation, we tried the non-wetting lamination with aluminum film. As shown in Figure 4.13, the lamination of clay/MXD6 film and aluminum film was performed well. Furthermore, water vapor transmission rate (WVTR) was improved by the lamination. For 6 um Al film, the WVTR can't be measured due to the existence of the pore or the pinholes in Al film. However, WVTR of laminates of 6 um Al film was decreased due to the blocking effect of clay/MXD6 film. Similar trend was observed in 12 um Al film. These results implied that the adhesion between Al film and clay/MXD6 film was established without defects. In addition, it was confirmed that the polymer surface treatment could improve not only the adhesion between polymers but also the adhesion between the polymer (organic) and the inorganic materials.

Table 4. 5. Water vapor transmission rate (WVTR) of different samples

Sample	Thickness (mm)	WVTR (gm-mil/m ² /day)
6um Al	0.007	Fail
12um Al	0.012	0.001
Clay/MXD6 film	0.072	1.016
6um Al + Clay/MXD6	0.078	0.003
12um Al + Clay/MXD6	0.085	0.008

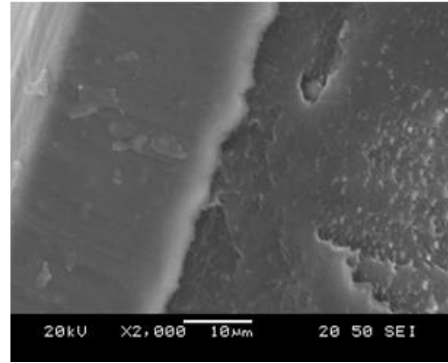
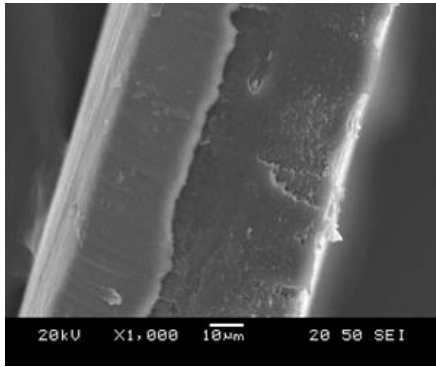


Figure 4. 13. Cross-section of the laminates of Al film and clay/MXD6

4. 4. Conclusions

In this study, we attempted to determine plausible fracture mechanisms at the polymer-polymer interface by investigating experimentally the effect of in situ reactive compatibilization on the fracture toughness of the interface between an amorphous polymer (PS) and a semi-crystalline polymer (Ny6) compatibilized with PSMA. The fracture toughness was found to increase with bonding time, pass through a maximum value, and then reach a plateau for bonding temperatures higher than 190 °C. The fracture toughness also increases with the bonding temperature, with a maximum near 200 °C and then decreases at higher bonding temperatures.

Additionally, we have used DSIMS to directly observe the fracture mechanism change at the polymer–polymer interface reinforced with in situ graft copolymers. The adhesion strength is affected by two different failure mechanisms, i.e., adhesive failure at short bonding times and/or low annealing temperatures due to the small amount of graft copolymers produced at the interface and cohesive failure at long bonding times or high temperatures because of the diffusion of nonfunctionalized molecules into the bulk and thus their disengagement from the produced copolymers at the interface or from other functionalized molecules near the interface. This results in the appearance of a maximum in the fracture toughness at a particular bonding time and temperature. The determined diffusion coefficients and the d-PS concentration profiles confirm this conclusion.

References

- [1] Seo, Y.; Lee, J.; Kang, T. J.; Choi, H. J.; Kim, J. In situ compatibilizer reinforced interface between an amorphous polymer (polystyrene) and a semicrystalline polymer (polyamide nylon 6). *Macromolecules* **2007**, *40*, 5953–5958.
- [2] Harton, S.; Stevie, F.; Ade, H. Diffusion-Controlled Reactive Coupling at Polymer–Polymer Interfaces. *Macromolecules* **2005**, *38*, 3543–3546.
- [3] Jiao, J.; Kramer, E. J.; de Vos, S.; Möller, M.; Koning, C. Morphological changes of a molten polymer/polymer interface driven by grafting. *Macromolecules* **1999**, *32*, 6261–6269.
- [4] Creton, C. Mechanical Properties of Polymer Interfaces in Polymer Surfaces and Interfaces; Richards, R. W., Peace, S. K., Eds.; John Wiley & Sons: Chichester, U.K., 1999.
- [5] Kim, H.-J.; Lee, K.-J.; Seo, Y. Enhancement of interfacial adhesion between polypropylene and nylon 6: Effect of surface functionalization by low-energy ion-beam irradiation. *Macromolecules* **2002**, *35*, 1267–1275.
- [6] Gurney, R.; Henry, A.; Schach, R.; Lindner, A.; Creton, C. Molecular weight dependence of interdiffusion and adhesion of polymers at short contact times. *Langmuir* **2017**, *33*, 1670–1678.
- [7] Seo, Y.; Ninh, T. H.; Hong, S. M.; Kim, S.; Kang, T. J.; Kim, H.; Kim, J. In situ compatibilizer-reinforced interface between a flexible polymer (a functionalized polypropylene) and a rodlike polymer (a thermotropic liquid crystalline polymer). *Langmuir* **2006**, *22*, 3062–3067.
- [8] Creton, C.; Kramer, E. J.; Brown, H. R.; Hui, C. Y. Adhesion and Fracture of Interfaces between Immiscible Polymers: From the Molecular to the Continuum Scale. *Adv. Polym. Sci.* **2002**, *156*, 53–136.

- [9] Zhang, C.; Feng, L.; Hu, G. *Reactive Extrusion: Principles and Applications*; Beyer, G., Hopmann, C., Eds.; Wiley-VCH: Weinheim, 2018; Chapter 9.
- [10] Norton, L. J.; Smigolova, V.; Pralle, M. U.; Hubenko, A.; Dai, K. H.; Kramer, E. J.; Hahn, S.; Berglund, C.; DeKoven, B. Effect of End-Anchored Chains on the Adhesion at a Thermoset-Thermoplastic Interface. *Macromolecules* **1995**, *28*, 1999–2009.
- [11] Boucher, E.; Folkers, J. P.; Creton, C.; Hervert, H.; Leger, L. Enhanced Adhesion between Polypropylene and Polyamide-6: Role of Interfacial Nucleation of the β -Crystalline Form of Polypropylene. *Macromolecules* **1997**, *30*, 2102–2109.
- [12] Laurens, C.; Creton, C.; Leger, L. Adhesion Promotion Mechanisms at Isotactic Polypropylene/Polyamide 6 Interfaces: Role of the Copolymer Architecture. *Macromolecules* **2004**, *37*, 6814–6822.
- [13] Creton, C. F.; Kramer, E. J.; Hui, C. Y.; Brown, H. R. Failure mechanisms of polymer interfaces reinforced with block copolymers. *Macromolecules* **1992**, *25*, 3075–3088.
- [14] Brown, H. R. A molecular interpretation of the toughness of glassy polymers. *Macromolecules* **1991**, *24*, 2752–2756.
- [15] Kim, S.; Lee, J.; Kim, H.; Seo, Y. P.; Hong, S. M.; Takahara, A.; Choi, H. J.; Seo, Y. Enhanced interfacial adhesion between an amorphous polymer (polystyrene) and a semicrystalline polymer [a polyamide (Nylon 6)]. *ACS Appl. Mater. Interfaces* **2011**, *3*, 2622–2629.
- [16] Seo, Y.; Ninh, T. H. Enhanced interfacial adhesion between polypropylene and nylon 6 by in situ reactive compatibilization. *Polymer* **2004**, *45*, 8573–8581.
- [17] Kim, H. J.; Seo, Y. Effect of surface modification on the interfacial tension between the melts of high-density polyethylene and nylon 66: Correlation between rheology and morphology. *Langmuir* **2003**, *19*, 2696–2704.

- [18] Kim, H.-J.; Lee, K.-J.; Seo, Y.; Kwak, S.; Koh, S.-K. HDPE surface functionalization by low-energy ion-beam irradiation under a reactive O₂ environment and its effect on the HDPE/nylon 66 blend. *Macromolecules* **2001**, *34*, 2546–2558.
- [19] Kim, S.; Lee, K.-J.; Seo, Y. Surface modification of poly (ether imide) by low-energy ion-beam irradiation and its effect on the polymer blend interface. *Langmuir* **2002**, *18*, 6185–6192.
- [20] Seo, Y.; Kim, S.; Kim, H.; Kim, J. Nonwetting process for achieving surface functionalization of chemically stable poly (tetrafluoroethylene). *Langmuir* **2005**, *21*, 3432–3435.
- [21] Hu, G.; Lindt, J. Amidification of poly (styrene-co-maleic anhydride) with amines in tetrahydrofuran solution: A kinetic study. *Polym. Bull.* **1992**, *29*, 357–363.
- [22] Antonietti, M.; Coutandin, J.; Sillescu, H. Chainlength and temperature dependence of self-diffusion coefficients in polystyrene. *Makromol. Chem., Rapid Commun.* **1984**, *5*, 525–528.
- [23] Schnell, R.; Stamm, M.; Creton, C. Direct Correlation between Interfacial Width and Adhesion in Glassy Polymers. *Macromolecules* **1998**, *31*, 2284–2292.
- [24] Kawaguchi, D.; Masuoka, K.; Takano, A.; Tanaka, K.; Nagamura, T.; Torikai, N.; Dalglish, R. M.; Langridge, S.; Matsushita, Y. Comparison of interdiffusion behavior between cyclic and linear polystyrenes with high molecular weights. *Macromolecules* **2006**, *39*, 5180–5182.
- [25] Kawaguchi, D.; Tanaka, K.; Takahara, A.; Kajiyama, T. Surface mobile layer of polystyrene film below bulk glass transition temperature. *Macromolecules* **2001**, *34*, 6164–6166.
- [26] Kawaguchi, D.; Tanaka, K.; Kajiyama, T.; Takahara, A.; Tasaki, S. Mobility gradient in surface region of monodisperse polystyrene films. *Macromolecules* **2003**, *36*, 1235–1240.

- [27] Whitlow, S. J.; Wool, R. P. Diffusion of polymers at interfaces: a secondary ion mass spectroscopy study. *Macromolecules* **1991**, *24*, 5926–5938.
- [28] Agrawal, G.; Wool, R.; Dozier, W.; Felcher, G.; Zhou, J.; Pispas, S.; Mays, J.; Russell, T. Interdiffusion of polymers across interfaces. *J. Polym. Sci., Part B: Polym. Phys.* **1996**, *34*, 2919–2940.
- [29] Sillescu, H. Relation of interdiffusion and self-diffusion in polymer mixtures. *Makromol. Chem., Rapid Commun.* **1984**, *5*, 519–523.
- [30] Doi, M.; Edwards, S. F. *The Theory of Polymer Dynamics*; Oxford University Press: New York, 1986; p 196.

Chapter 5. MR Fluid High-Performance

Magnetorheological Suspensions of Magnetic Particle-deposited Carbon Nanotubes with Enhanced Stability

5. 1. Introduction

Magnetorheological (MR) fluids which are suspensions of fine particles in a magnetically insulating fluid are kind of smart materials because they can form a solid-like structure of fibril shapes along the magnetic field direction upon application of a magnetic field [1]. When the magnetic field is applied, randomly dispersed particles can rapidly form fibril shapes (meso-structure) along the field direction due to polarization between the suspended particles. Reverse structural transition happens once the applied field is removed. The structural changes occur very quickly, on the order of milliseconds [2]. The meso-structure formed in response to a magnetic field enable the apparent viscosities of the MR fluids to be increased by 3 to 4 orders of magnitude. The properties of magnetorheological (MR) fluids can be controlled over a wide range by varying the magnetic field intensity. The field-responsive properties of MR fluids are quite useful for a variety of mechanical systems. In the automotive industry, for example, the variable properties of MR fluids have been used in vehicle suspension systems, clutches, power steering pumps,

torque transducer [3–5]. Ferromagnetic materials such as maghemite (Fe_2O_3), magnetite (Fe_3O_4), or carbonyl iron (CI) generally show high magnetization values and less magnetic hysteresis [1,11]. However, MR fluids of these ferromagnetic particles have a drawback of poor long-term stability because of a density mismatch between the magnetic particles and the suspending media. The long-term stability should be improved for wider industrial applications. Significant efforts have been devoted to overcoming the sedimentation problem, such as the introduction of polymer coatings or passivation layers onto the magnetic particles, addition of additives and fillers, or use of a viscoplastic medium [6–10]. Another effective method is to fabricate particles of a low density polymeric material encapsulated by fine magnetic particles [1,11]. We have reported several approaches to improve the stability of MR Fluids in the ferromagnetic materials-based system [9–11]. Especially, the Pickering-emulsion polymerization method to prepare iron oxide (Fe_2O_3 , Fe_3O_4)-coated polystyrene particles was successful [10,11]. Spherical iron oxide nanoparticles were used as a stabilizer, and their MR properties were examined at various magnetic field strengths after the particles were dispersed in silicone oil. The incorporation of the polymer core and the iron oxide shell not only reduced the density of the particles but also improved the dispersibility of the core-shell nanoparticles. The density of the PS/iron oxide particles was significantly reduced, and the stability of the suspensions was improved. In this study, the simple chemical co-precipitation method was used to fabricate a composite of MWCNTs deposited with Fe_3O_4 and FeCo nanoparticles. The morphology, density and the magnetic properties of the particle were investigated. Furthermore, the magnetorheological

behavior of MR fluid that utilized CNT/Fe₃O₄, CNT/FeCo and the sedimentation of the suspension was also studied.

5. 2. Experimental Section

5. 2. 1. Functionalization of CNTs

The MWCNTs used in this study were purchased from Hanwha Nano tech Corp and their diameter is 10 ~ 15 nm. Functionalized MWCNTs were prepared using mixed solution of H₂SO₄/HNO₃. 1g of MWCNTs was added in 400 ml of H₂SO₄/HNO₃ (3:1 volume ratio) mixed solution and heated at 60 °C for 8h under reflux. The sample denoted as F-MWCNTs was filtrated and washed with deionized water for several times and dried in vacuum for 24 h. For further functionalization, F-MWCNTs were immersed in ethylenediamine at 35 °C for 3h under mild sonification [12]. After treatment, the samples were washed with water and dried in a hot air oven at 110 °C for 6 h. The ethylenediamine treated f-MWCNTs are referred to as A-MWCNTs.

5. 2. 2. Synthesis of CNT-Fe₃O₄ particles

The CNT-Fe₃O₄ nanoparticles were prepared by using chemical coprecipitation of Fe₃O₄ nanoparticles onto the surface of A-MWCNTs [13,14]. A general synthesis of CNT-Fe₃O₄ is as follows. A-MWCNTs (1g) was added to 300 ml of deionized water

and then ultrasonicated for an hour. After ultrasonication, 7.2g $\text{FeCl}_3 \cdot 6\text{H}_2\text{O}$ and 3.208g $\text{FeSO}_4 \cdot 7\text{H}_2\text{O}$ were added into the mixture of A-MWCNT and water. The solution was deoxygenated for 1h with nitrogen gas. Then, solution was heated to 70 °C and ammonium hydroxide was added rapidly under stirring for 30 min. After 4h, temperature was then decreased to room temperature. The synthesized particles were collected by using a permanent magnet and washed several times with ethanol and dried in vacuum for 24h. The pure Fe_3O_4 was synthesized via the same procedure without CNTs.

5. 2. 3. Synthesis of CNT-FeCo particles

The CNT-FeCo nanoparticles were prepared by using chemical coprecipitation of FeCo nanoparticles onto the surface of A-MWCNTs. The functionalization of MWCNTs was proceed as described as above. A general synthesis of CNT-FeCo is as follows. A-MWCNTs (1g) was added to 300ml of deionized water and then ultrasonicated for an hour. After ultrasonication, 7.2g $\text{FeCl}_3 \cdot 6\text{H}_2\text{O}$ and 3.208g $\text{CoCl}_2 \cdot 4\text{H}_2\text{O}$ were added into the mixture of A-MWCNT and water. The solution was deoxygenated for 1h with nitrogen gas. Then, sodium borohydride solution (200ml) was added slowly under stirring for 30 min. After an hour, the synthesized particles were collected by using a permanent magnet and washed several times with ethanol and dried in vacuum for 24h.

5. 2. 4. Characterization

The densities of MWCNT, Fe₃O₄, CNT/Fe₃O₄, and CNT/FeCo particles were measured using a helium pycnometer (AccuPyc 1330, Micromeritics Instrument Corporation, Norcross, GA). The morphology of the synthesized particles was observed by scanning electron microscopy (SEM; JEM-7600F, JEOL, JAPAN) and transmission electron microscopy (TEM; JEM-F200, JEOL, JAPAN). Optical microscopy (Olympus BX-51, Japan) was also used to observe the response of MR fluids during exposure to an applied magnetic field. The magnetic characteristics were examined using a vibrating sample magnetometer (VSM; model 7370, Lake Shore Cryotronics, Westerville, OH) over the range of -5 to 5 kOe. The magnetite content of the modified CNTs was measured by thermogravimetric analysis (TGA, TGA/DSC1, Mettler-Toledo, USA). TGA measurement was performed between room temperature and 1000 °C with heating rate 10 °C/min under O₂ atmosphere. MR fluid was prepared by dispersing the particles in silicon oil (KF-96, 10 cS, density (ρ) = 0.96 g/cm³, Shin-Etsu, Japan). The particle concentration was 10 vol%. The rheological properties of the MR fluids were measured using a commercial rotational rheometer (Physica MCR301, Stuttgart, Germany) equipped with a magnetic generator (Physica MRD 180). A parallel-plate measuring system with a diameter of 20 mm was employed at a gap distance of 1 mm. The sedimentation stability of CNT/Fe₃O₄ and CNT/FeCo particle suspensions was checked by using a Turbiscan (Classic MA2000, Formulation, France).

5. 3. Results and Discussion

5. 3. 1. Morphology & Structure

The morphology of Fe₃O₄-deposited CNT was examined by SEM and TEM. Some typical images of CNT/Fe₃O₄ are shown in Figure 5.1. As shown in Figure 5.1, the spherical iron oxide particles covered the outside of the CNTs and the size of most particles ranged from 10 nm to 30nm. The FeCo-deposited CNT showed similar morphology as shown in Figure 5.2. However, coarser particle around CNT was observed in TEM images (~50 nm). Furthermore, the characteristic peaks of iron-cobalt alloys were confirmed in X-ray diffraction pattern and FeCo-decorated CNT was successfully synthesized (Figure 5.3)

5. 3. 2. Magnetorheological behaviors

TGA measurement shows the quantitative analysis of particles (Figure 5.4(a)) which indicates that the content of magnetite in the CNT/Fe₃O₄ is ca 67%. Since magnetic response of the particle is attributed to Fe₃O₄ covering CNTs, the saturation magnetization value is proportional to the amount of remaining Fe₃O₄ nanoparticles. The densities of MWCNT, Fe₃O₄, CNT/Fe₃O₄, and CNT/FeCo are presented in Table 5.1. Figure 5.4(b) shows the magnetic hysteresis loops for pure Fe₃O₄, CNT/ Fe₃O₄, and CNT/FeCo particles in powder state over the range of -5 to 5 kOe. As shown in Figure 4b), very small coercive force and high magnetic saturation value are

observed. The saturation magnetization value of the Fe_3O_4 deposited CNTs was 42.0 emu g^{-1} which was smaller than that of pure Fe_3O_4 (66.7 emu g^{-1}), but in good agreement with the amount of involved Fe_3O_4 (Figure 5.4(a)). In case of the CNT/FeCo, higher saturation magnetization value was observed (66.0 emu g^{-1}). High M_s of CNT/FeCo was due to the saturation magnetization value of pure FeCo (102.3 emu g^{-1})

Once the magnetic field is on, the MR fluid displayed a rapid transition from uniformly dispersed state to chain-like network structures along magnetic field. Figure 5.5 shows a photograph of the MR fluid before and after the application of an external magnetic field. When an external magnetic field was on, the chain-like structures were formed in response to the external field. As soon as the external magnetic field was off, the magnetic particles returned to uniformly dispersed state again. Dynamic oscillatory tests (amplitude and frequency dependence) of CNT/ Fe_3O_4 is shown in Figure 5.6. Figure 5.6(a) exhibits the amplitude-sweep measurement, which represents the change of the storage modulus as a function of the strain, ranging from 0.01 to 100%. The storage modulus tends to increase with the magnetic field strength because of the dipole–dipole interactions between particles. The plateau region is observed in a strain range to 0.02% for both magnetic field strengths of 86 and 343 kA/m. This region is the linear viscoelastic region, where the storage modulus is constant regardless of the applied strain. The meso-structures formed under the magnetic polarization remain undisturbed. As the strain amplitude increased, the storage modulus showed a gradual decrease because the meso-structures started to break apart. Figure 4b shows the frequency-sweep

measurement of the storage modulus (G') and the loss modulus (G'') at a strain of 0.01%. The storage modulus of the particle suspensions were one orders of magnitude larger than the corresponding loss modulus. This indicates that the solid-like elastic properties of those MR fluids upon exposure to the magnetic field was strong because of the mesostructured formation [15]. Though the nanosized Fe_3O_4 particles were surface-deposited on the CNTs surface, they were polarized strongly enough to maintain those chain-like meso-structures.

In most MR fluids, the meso-structures are strong enough to withstand the external shear stress at low shear rates, but they are broken down at high shear rates. The shear stress of the MR suspensions remains at constant values at low shear rates and goes down slightly with the structural change and rises again because of the high shear stress (Figure 5.7(a)). CNT/ Fe_3O_4 particle suspensions have lower shear stress than pure Fe_3O_4 particle suspensions because the uncovered CNTs (small amount of Fe_3O_4 on the CNT surface) and large particles hinders particle aggregation [17]. At very high shear rates, the hydrodynamic stress increased the shear stress. And the dependence of the shear stress on the shear rate and applied magnetic field strength is well demonstrated in Figure 5.7(a). As the shear rate increased, the viscosity of the suspensions decreased linearly (Figure 5.7(b)).

In the case of CNT/ FeCo nanoparticles, MR behavior was very similar to the CNT/ Fe_3O_4 suspensions as shown in Figure 5.8 and 5.9(a). This was because the morphology and structure except for the size of magnetic particles are similar to Fe_3O_4 . Figure 5.9(b) compared the storage modulus dependence between CNT/ Fe_3O_4 and CNT/ FeCo suspension. Due to the high saturation magnetization

value of CNT/FeCo (66.0 emu g⁻¹), the CNT/FeCo suspension showed higher yield stress, storage modulus than CNT/Fe₃O₄ suspension.

The static yield stress was measured using the controlled shear stress (CSS) method. Figure 5.10(a) shows the change of viscosity as a function of the shear stress. The shear viscosity showed a sharp decrease after a certain shear stress value. The values of shear stress marked with arrows in Figure 5.10(a) and the point is the static yield stress that required to initiate flow. Under the applied magnetic field, the system exhibited Bingham fluid behaviors.

$$\tau = \tau_{dy} + \eta_{pl}\dot{\gamma} \quad (5.1)$$

where τ is the shear stress, τ_{dy} is the dynamic stress, η_{pl} is the plastic viscosity and $\dot{\gamma}$ is the shear rate. For the plausible analysis of the MR fluids, the static yield stress is recommended to be applied rather than the dynamic yield stress because it is the stress to initiate the flow (true yield stress) rather than the latter which is the extrapolation of the shear stress in the broken state to zero shear rate. Recently, Seo and Seo suggested a new constitutive model for predicting the static yield stress as follows,

$$\tau = \tau_{sy} \left(1 - \frac{(1 - \exp(-a\dot{\gamma}))}{(1 + (a\dot{\gamma})^\alpha)} \right) + \eta_{pl}\dot{\gamma} \quad (5.2)$$

where τ_{sy} is the static yield stress, η_{pl} is the plastic viscosity, a is the time constant (the reciprocal of the critical shear rate for an aligned meso-structure deformation), and α is the power-law index used to decide the degree of shear thinning. The effects of each parameter on stress behaviors have been described previously [15]. The static yield stress predicted by the Seo-Seo model, the experimental data, the dynamic yield stress by Bingham model are compared in Table 5.2. The static stress values

predicted by Seo-Seo model agreed well with the measured static yield stress because the magnetic polarization dominated the shear stress across almost all shear rates [15], but the dynamic yield stress values are also close to the measurement due to the shallow stress well depth [1].

The suspensions exhibited a wide plateau region over the low shear rate. The dynamic yield stress values were obtained by fitting the above relationship. Figure 5.10(b) shows the dynamic yield stresses of the MR fluids as a function of the magnetic field strength. At low magnetic fields, the yield stress increases almost quadratically (~ 1.65) with the magnetic field strength, whereas it followed a 1.0 power-law under strong magnetic fields [11,16]. At a sufficiently high magnetic field, magnetization saturation occurred, and the polarization force failed to increase with increasing magnetic field intensity.

5. 3. 3. Suspension stability

The light transmission profile as a function of time for Fe_3O_4 , CNT/ Fe_3O_4 , and CNT/FeCo are shown in Figure 5.11. The transmission ratio increased gradually over time due to the sedimentation of the particles. The pure Fe_3O_4 particles suspension showed the highest transmission, reaching 45% within 24h. The CNT/ Fe_3O_4 particles suspensions showed remarkable stability ($\sim 4\%$). In addition, CNT/FeCo suspensions also showed improvement stability ($\sim 13\%$) but lower than CNT/ Fe_3O_4 suspensions. This improvement of stability of magnetic particle decorated CNT are due to the characteristics of CNT. CNT was not responsive to external magnetic field,

it occupies most of the particle volume to reduce its density. The lower density of the CNT/ Fe_3O_4 and CNT/FeCo particle and hollow structure of CNTs contributed to this stability. Moreover, the high aspect ratio of CNTs will be favorable for the supporting effects between the particles [17].

5. 4. Conclusion

In this work, we have reported the fabrication method to enhance the sedimentation stability in Fe_3O_4 -based MR Fluid. Fe_3O_4 -deposited CNTs were synthesized by chemical co-precipitation method using iron ions. The incorporation of CNTs and Fe_3O_4 nanoparticles decreased particle density remarkably. MR fluids that utilized CNT/ Fe_3O_4 showed high magnetorheological performances and exhibited stability against the sedimentation owing to reduced particle-fluid density mismatch, hollow structure of CNTs and the supporting effect of inherent CNT tube-like particles. Though yield stress was lower than that of bare Fe_3O_4 , its excellent improved sedimentation stability can find appropriate applications. In addition, we have fabricated CNT/FeCo nanoparticles to overcome above limitation. Due to the high saturation magnetization of CNT/FeCo, the suspension showed great yield stress and sedimentation stability.

Table 5. 1. The densities of CNT, Fe₃O₄, CNT/Fe₃O₄

	MWCNT	Pure Fe ₃ O ₄	CNT/Fe ₃ O ₄	CNT/FeCo
Density	1.5g/cm ³	4.90g/cm ³	2.91g/cm ³	3.47 g/cm ³

Table 5. 2. Static yield stress and dynamic yield stress of the suspensions of CNT/Fe₃O₄ suspension.

Yield Stress [Pa]		
	M = 86kA/m	M = 343kA/m
τ (exp)	28.8	138.5
τ (static)	33	145
τ (dynamic)	24.1	139.4

Table 5. 3. Static yield stress and dynamic yield stress of the suspensions of CNT/FeCo suspension.

Yield Stress [Pa]		
	M = 86kA/m	M = 343kA/m
τ (exp)	396	765
τ (static)	402	780
τ (dynamic)	401	785

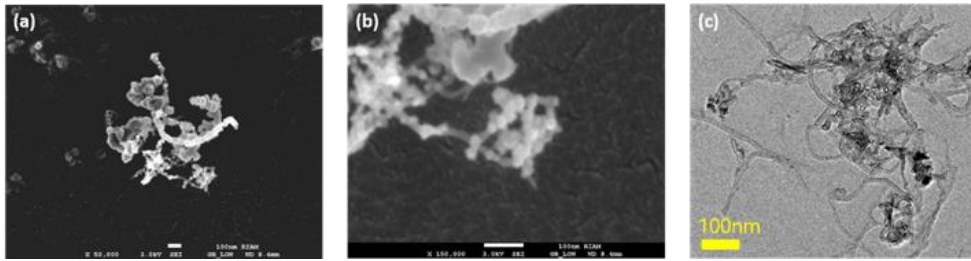


Figure 5. 1. SEM photographs of (a, b) CNT/Fe₃O₄, and (c) TEM images of CNT/Fe₃O₄ particles.

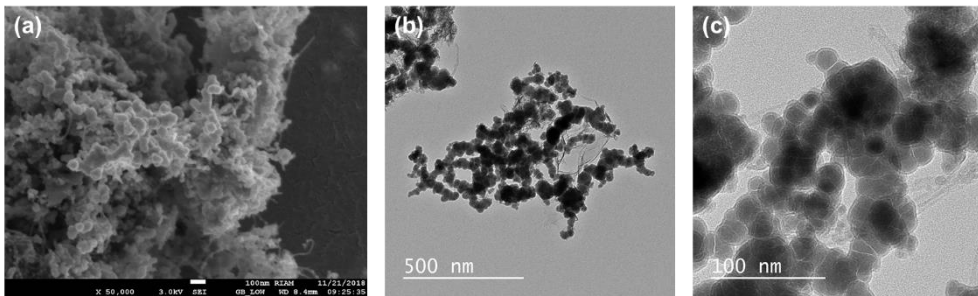


Figure 5. 2. SEM photograph of (a) CNT/FeCo and (b, c) TEM images of CNT/FeCo particles

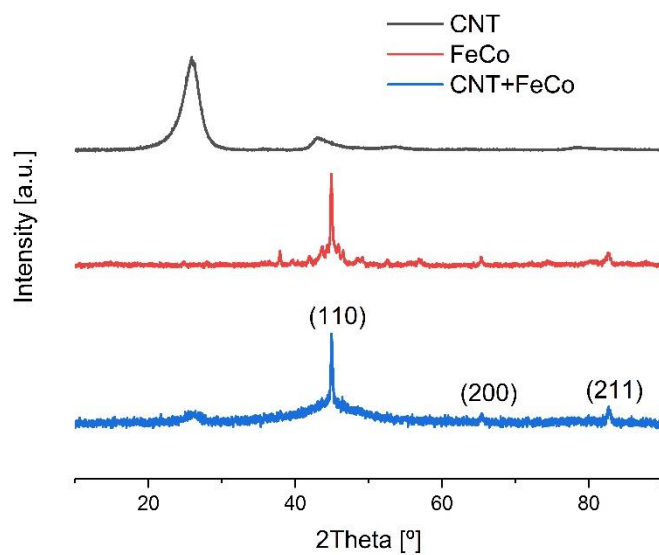


Figure 5. 3. X-ray diffraction patterns of CNT, FeCo, and CNT/FeCo

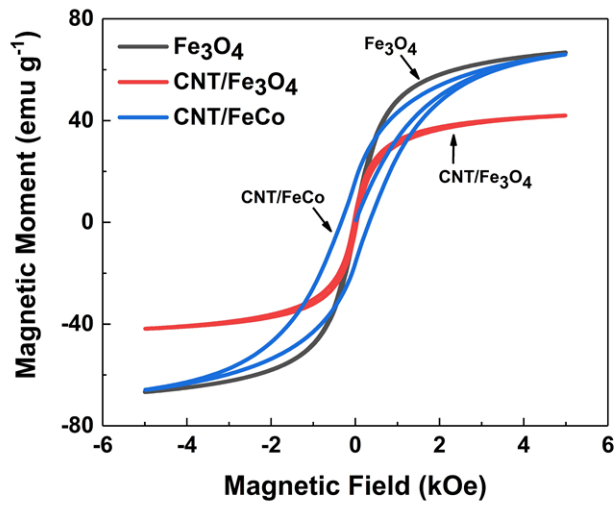
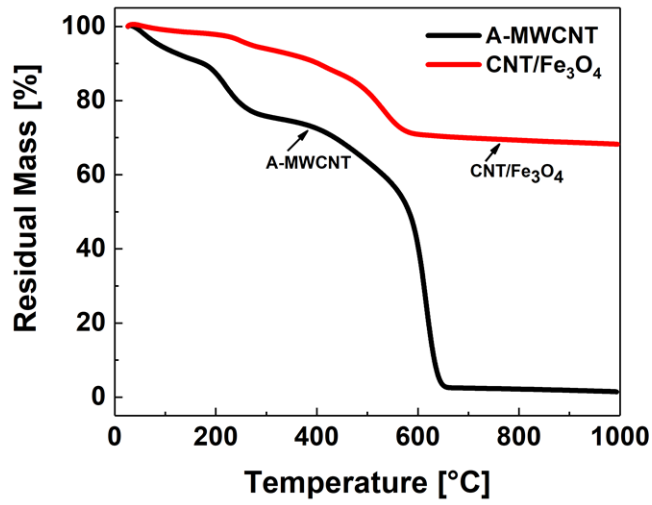


Figure 5. 4. (a) TGA measurement data and (b) VSM data of CNT, CNT/Fe₃O₄, CNT/FeCo

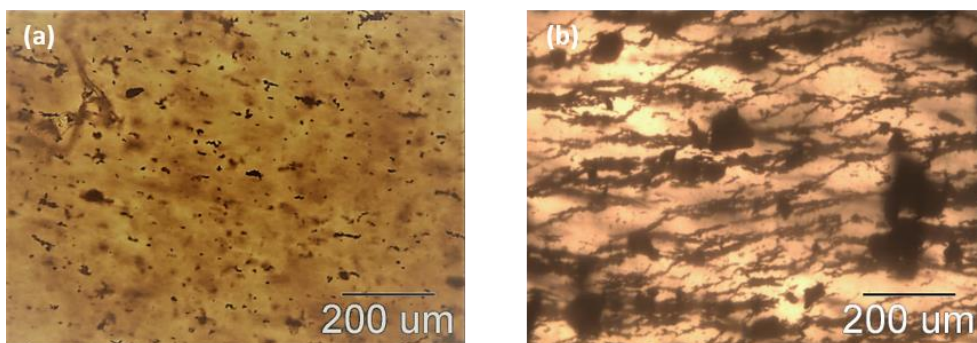


Figure 5. 5. Optical microscope images of CNT/Fe₃O₄ suspension (a) before and (b) after the application of the external magnetic field.

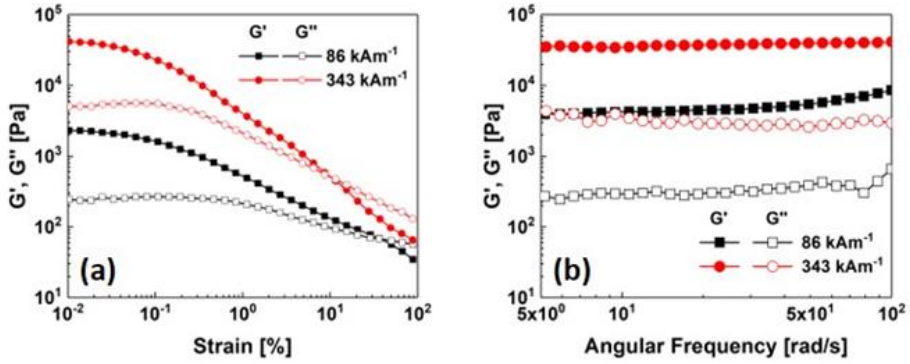


Figure 5. 6. (a) Amplitude-sweep dependence of the storage modulus, G' , and loss modulus, G'' . (b) Frequency dependence of G' , G'' of CNT/ Fe_3O_4 particles

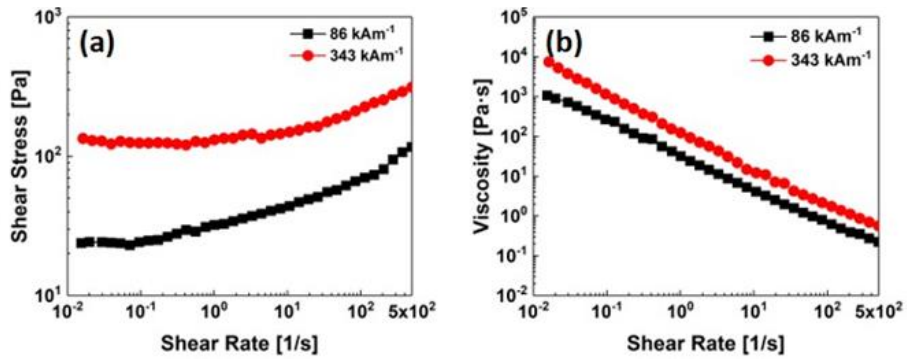


Figure 5. 7. (a) Shear stress and (b) shear viscosity flow curves for 10 vol% CNT/ Fe_3O_4 suspension

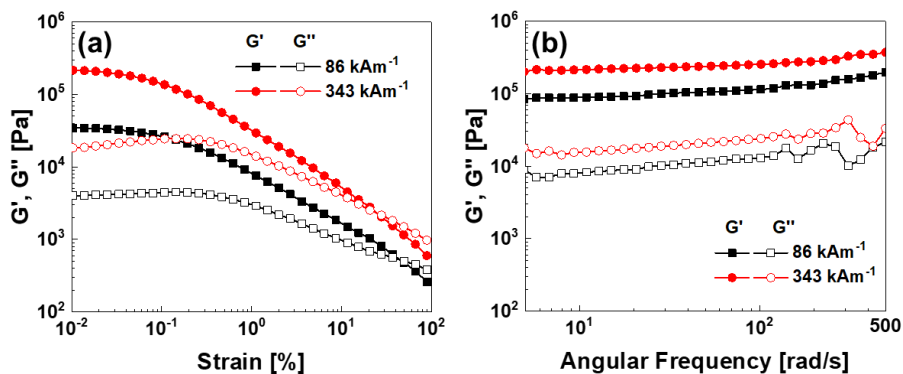


Figure 5. 8. (a) Amplitude-sweep dependence of the storage modulus, G' , and loss modulus, G'' . (b) Frequency dependence of G' , G'' of CNT/FeCo particles

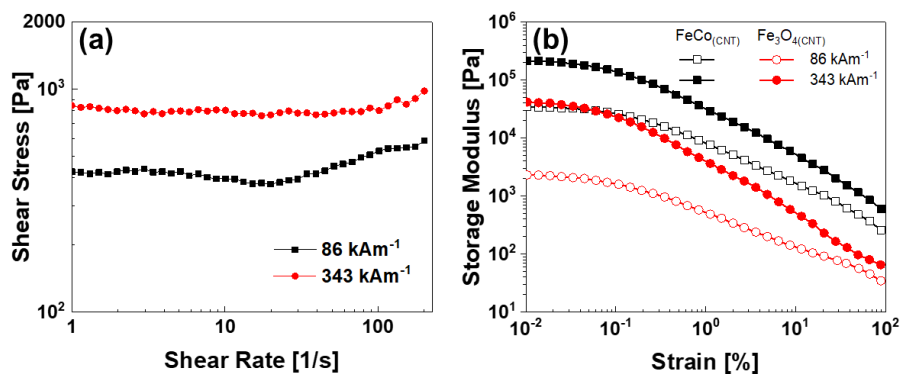


Figure 5. 9. (a) Shear stress flow curve of CNT/FeCo suspension and (b) storage modulus comparison between CNT/Fe₃O₄ and CNT/FeCo suspensions

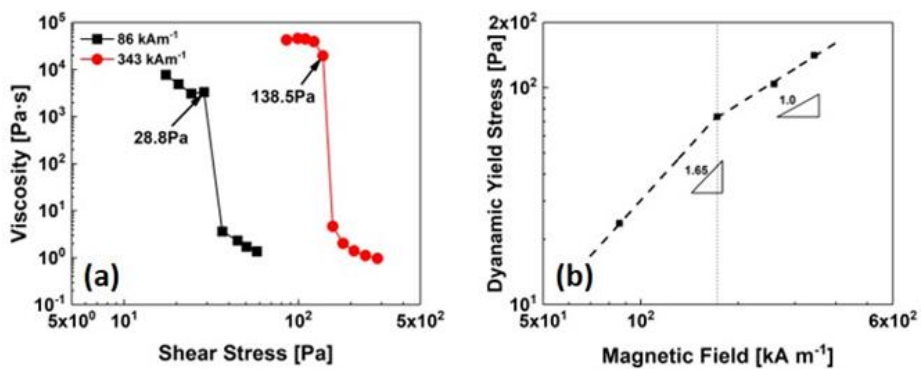


Figure 5. 10. (a) Static yield stress curve and (b) Dynamic yield stress dependence on the magnetic field strength

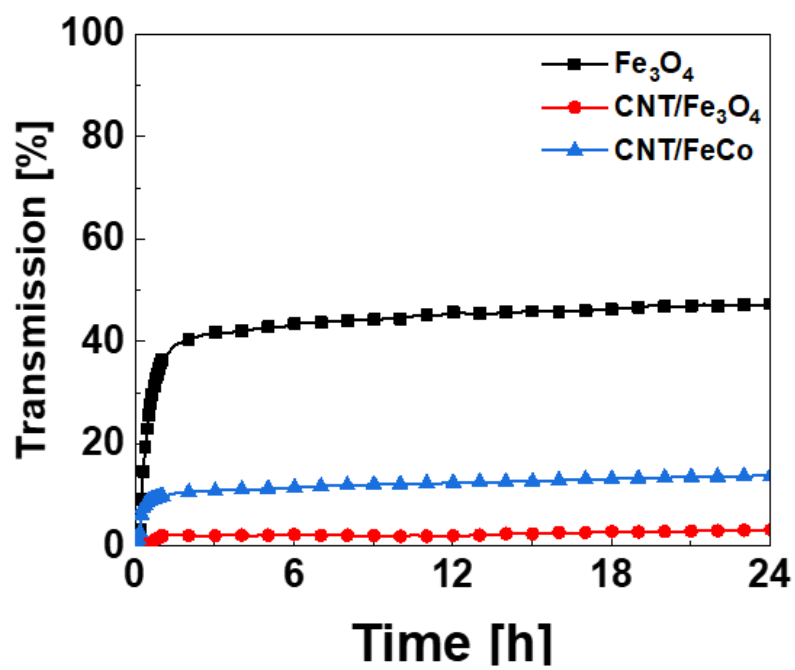


Figure 5. 11. The light transmission [%] as function of time [h] for CNT, CNT/Fe₃O₄ and CNT/FeCo suspensions (10 vol%).

References

- [1] Seo, Y. P.; Han, S., Choi; J.; Takahara, A.; Choi, H. J.; Seo, Y., Searching for a stable high-performance magnetorheological suspension. *Adv. Mat.* **2018**, 30(42), 1704769.
- [2] Seo, Y. P.; Choi, H. J.; Lee, J. R.; Seo, Y., Modeling and analysis of an electrorheological flow behavior containing semiconducting graphene oxide/polyaniline composite particles. *Colloid. Surf. A-Physicochem. Eng. Asp.* **2014**, 457, 363-367.
- [3] Seo, Y. P.; Choi, H. J.; Seo, Y., Analysis of the flow behavior of electrorheological fluids with the aligned structure reformation. *Polymer* **2011**, 52(25), 5695-5698.
- [4] Cvek, M.; Mrlík, M.; Ilčíková, M.; Mosnáček, J.; Münster, L.; Pavlínek, V., Synthesis of silicone elastomers containing silyl-based polymer-grafted carbonyl iron particles: an efficient way to improve magnetorheological, damping, and sensing performances. *Macromolecules* **2017**, 50(5), 2189-2200.
- [5] Choi, H.; Zhang, W.; Kim, S.; Seo, Y., Core-shell structured electro-and magneto-responsive materials: Fabrication and characteristics. *Materials* **2014**, 7(11), 7460-7471.
- [6] Hu, B.; Fuchs, A.; Huseyin, S.; Gordaninejad, F.; Evrensel, C., Atom transfer radical polymerized MR fluids. *Polymer* **2006**, 47(22), 7653-7663.

- [7] Seo, Y. P.; Choi, H. J.; Seo, Y., A simplified model for analyzing the flow behavior of electrorheological fluids containing silica nanoparticle-decorated polyaniline nanofibers. *Soft Matt.* **2012**, 8(17), 4659-4663.
- [8] Chuah, W. H.; Zhang, W. L.; Choi, H. J.; Seo, Y., Magnetorheology of core-shell structured carbonyl iron/polystyrene foam microparticles suspension with enhanced stability. *Macromolecules* **2015**, 48(19), 7311-7319.
- [9] Kim, Y. J.; Liu, Y. D.; Seo, Y.; Choi, H. J., Pickering-emulsion-polymerized polystyrene/Fe₂O₃ composite particles and their magnetoresponse characteristics. *Langmuir* **2013**, 29(16), 4959-4965.
- [10] Han, S.; Choi, J.; Seo, Y. P.; Park, I. J.; Choi, H. J.; Seo, Y., High-Performance Magnetorheological Suspensions of Pickering-Emulsion-Polymerized Polystyrene/Fe₃O₄ Particles with Enhanced Stability. *Langmuir* **2018**, 34(8), 2807-2814.
- [11] Murugesan, S.; Myers, K.; Subramanian, V. R., Amino-functionalized and acid treated multi-walled carbon nanotubes as supports for electrochemical oxidation of formic acid. *Appl. Catal. B* **2011** 103(3-4), 266-274.
- [12] Huiqun, C.; Meifang, Z.; Yaogang, L., Novel carbon nanotube iron oxide magnetic nanocomposites. *J. Magn. Magn. Mater.* **2006**, 305(2), 321-324.
- [13] Yang, L.; Hu, J.; Dong, A.; Yang, D., Novel Fe₃O₄-CNTs nanocomposite for Li-ion batteries with enhanced electrochemical performance. *Electrochim. Acta* **2014**, 144, 235-242.
- [14] Seo, Y. P.; Seo, Y., Modeling and analysis of electrorheological suspensions in shear flow. *Langmuir* **2012**, 28 (6), 3077-3084.

- [15] Choi, H. J.; Cho, M. S.; Kim, J. W.; Kim, C. A.; Jhon, M. S., A yield stress scaling function for electrorheological fluids. *Appl. Phys. Lett.* **2001**, 78(24), 3806-3808.
- [16] Pu, H.; Jiang, F., Towards high sedimentation stability: magnetorheological fluids based on CNT/Fe₃O₄ nanocomposites. *Nanotechnology* **2015**, 16(9), 1486.

Chapter 6. Conclusions

6. 1. Overall Conclusions

In conclusion, to test the feasibility of substitutes for lead in X-ray radiation shielding applications, three different non-lead metals (tungsten, tin and bismuth-tin alloy (BiSn)) were used to prepare metal-polymer composites. Tin exhibits a shielding efficiency that is comparable to that of tungsten between 29 keV (the K-edge energy of tin) and 69 keV (the K-edge energy of tungsten). Considering the lightness of tin, it can be used to shield low energy X-ray radiation. BiSn exhibits much better shielding (a low dose ratio) than tin, and the shielding was comparable to that of tungsten for all X-ray energy ranges. It is composed of 42% tin and 58% bismuth, so it effectively shields low energy X-ray radiation due to its tin component and high energy level radiation due to its bismuth component; the K-edge energy (90 keV) is much higher than that of tungsten. Thus, we have demonstrated that BiSn exhibits better performance than tungsten and is a suitable candidate for X-ray shielding applications.

Based on this result, we pressed a multilayered sheet of gauze on which BiSn suspension was painted. The sheet was found to exhibit good X-ray shielding but also non-uniformity in the dispersed metal phase. The lamination of the stacked sheet with a WP film or a BiSnP film was found to improve the non-uniform dose ratio

over the whole surface. The melting and agglomeration of the BiSn particles mean that the sheet laminated with a BiSnP film exhibits a more uniform dose ratio than the sheet laminated with a WP film. An important feature of the BiSn alloy is its absorption of high-energy photons by its high atomic number component (bismuth) and low-energy photons by its low atomic number component (tin), which means that its X-ray radiation shielding is very effective.

The BiSn alloy promises to be useful in the manufacturing of X-ray radiation shielding apparels because of its excellent shielding, nontoxicity and low density. Further, it can be processed with typical polymer processing equipment. These results suggest that the use of non-lead metal (BiSn)/polymer composites as a substitute for the harmful lead currently widely used in X-ray shielding plates and medical gowns is feasible.

In order to test the feasibility of substitutes for the lead in the shielding equipment against high energy radiation of γ -ray (667 keV from ^{137}Cs source), multilayer composites of (BiSn/polymer)/tungsten were fabricated. All prepared composite sheets show a fairly good shielding ability against the high energy γ -ray radiation. Both the BiSn (400phr)/polymer sheet and tungsten flakes showed the shielding efficiency following the Beer-Lambert law. The transmittance of the tungsten sheet is expressed as $(I/I_0)_{\text{Tungsten}} = \exp(-0.23282 \cdot x)$ while that of the BiSn/polymer composite follows the fitting equation of $(I/I_0)_{\text{BiSn/polymer}} = \exp(-0.0308 \cdot x)$ where x is the thickness of the composite material in mm. Therefore, tungsten sheet exhibits the 7 times shielding efficiency than the BiSn (400phr)/polymer composite sheet of the same thickness. When the BiSn/polymer composite sheet and tungsten sheet are

combined to form multilayered laminates, a synergistic effect was observed such that 12 mm thick tungsten sheet show the same 95% shielding efficiency once it is adhered on the 10 mm thick BiSn/polymer

In case of EMI shielding composites, Sendust/MWCNT/polymer composites were prepared by applying a solution blending method and using an internal mixer. The incorporation of MWCNTs with micro-forged Sendust could significantly improve the electromagnetic wave absorption and EMI shielding efficiency compared to Sendust/polymer composites. The loss mechanism of the Sendust/MWCNT/polymer composites consists of both magnetic loss and dielectric loss. Added MWCNTs could improve the permittivity of composites, causing a large increase in dielectric loss. The composite containing 100 phr Sendust and 15 phr MWCNTs absorbed 60 % of the energy at 1 GHz and demonstrates a wide shielding frequency range. On the other hand, the reflection loss value reached -17 dB at 4.6 GHz in the composite containing 5 phr MWCNTs. The total SE value increased with the amount of MWCNT due to the enhanced dielectric loss caused by increased permittivity and improvement in conductivity of the ternary composites. In addition, the composite produced by this approach has the practical advantage of being able to produce light and thin microwave absorption materials with excellent EMI shielding efficiency in a wide frequency range.

Furthermore, we have used DSIMS to directly observe the fracture mechanism change at the polymer–polymer interface reinforced with in situ graft copolymers. The adhesion strength is affected by two different failure mechanisms, i.e., adhesive failure at short bonding times and/or low annealing temperatures due to the small

amount of graft copolymers produced at the interface and cohesive failure at long bonding times or high temperatures because of the diffusion of nonfunctionalized molecules into the bulk and thus their disengagement from the produced copolymers at the interface or from other functionalized molecules near the interface. This results in the appearance of a maximum in the fracture toughness at a particular bonding time and temperature. The determined diffusion coefficients and the d-PS concentration profiles confirm this conclusion.

6. 2. Further Works

In this study, composite materials with various barrier properties were fabricated and analyzed. We believe that these studies suggest a method to obtain higher barrier properties in composite materials. However, further challenges still remained and summarize as follows.

1. In EMI shielding, it was confirmed that the combination of dielectric material and magnetic material has a synergistic effect. However, the influence of the morphology of the fillers on EMI SE needs to be clarified. Also, it is necessary to confirm the possibility of shielding materials which have both two characteristics.

2. EMI shielding composites have characteristics required depending on the place and environment (absorption, reflection). The shielding material having a multilayer structure can obtain versatile shielding properties as well as blocking

properties for wide ranges (frequency). Therefore, it is necessary to study the shielding properties of such multilayer materials.

3. In the case of iron cobalt alloys, it is known that crystal structure can be grown through reduction, thereby increasing the saturation magnetization. This effect can improve the performance of MR Fluid. We are currently studying whether this effect can be seen in CNT/FeCo particles.

국문 초록

복합재료는 다른 형태의 재료를 조합하여 만든 multiphase 재료라고 볼 수 있다. 복합재료는 구성물질 각각의 특성으로부터 얻을 수 없는 여러 가지 다양한 성질은 갖는 특징이 있다. 복합재료의 조성, 분산, 형태, 결정화도, 결정구도 그리고 계면에서의 구조 등의 변화를 통해 성질을 조절할 수 있다. 이런 뛰어난 가공성형성(개질성) 때문에 복합재료는 항공, 자동차, 전자, 건설, 에너지, 생명과학 및 다른 여러 산업 분야에서 요구되는 특징을 만족시키기 위해 사용되고 있다. 복합재료의 필러 선택에 따라서 부여되는 특징 중 차단 특성은 여러 가지 산업분야 및 일상생활에서 중요한 요소다. 사람이나 물체를 외부로부터 보호하는 차폐재료는 인체를 상해로부터 지키거나, 제품이 올바르게 작동하도록 한다. 가장 일반적인 차단 요소는 수분이나 기체 등이 있으며, 또한 전자파, 방사선 등 강한 에너지를 갖는 복사선도 차단해야 할 외부 요인 중 하나이다.

본 연구에서는 고분자 복합재료가 갖는 경량성, 가공용이성 등을 활용하여 다양한 차단성을 갖는 복합재료를 제조하였다. 이 연구에서는 외부차폐요소로서 이온화 방사선, 마이크로파, 수증기 및 외력에 초점을 두고 진행하였다. 방사선 차폐 복합재료의 경우, 납을 대신하여 비스무트, 주석 합금과 텅스텐을 사용하여 복합재료를 만들었다. 또한 이를 적층 하여 다층구조로 형성하여 방사선 차폐 특성을 분석하였다. 이러한 과정을 통해 엑스선과 감마선을 효율적으로 차폐할 수 있었다.

또한 전자과 차폐를 위해 유전물질인 탄소나노튜브와 자성물질인 센더스트 합금을 조합을 통해 기존 차폐재료보다 가벼우면서도 더 높은 차단효율을 갖는 복합재료를 제조하였다. 두 재료의 조합을 통해 발생하는 전기적 특성의 변화가 이러한 향상의 원인임을 여러 가지 분석방법을 통해 확인하였다.

추가적으로, 여러 가지 차단 특성을 갖는 복합재료를 하나의 다층재료로 성형하기 위한 기초 연구로 고분자 계면에서의 접착 거동에 대한 연구를 진행하였다. 서로 섞이지 않는 고분자 간의 접착력을 일반적으로 매우 낮다. 이를 극복하기 위해 in-situ 상용화제를 첨가하거나 표면처리를 진행함으로써 고분자 간의 접착력을 향상시킬 수 있었다. 그 과정에서 접착력이 온도와 시간에 따라 변화하는 것을 확인하였으며, 추가적인 질량분석 및 표면분석을 통해 이러한 거동이 발생하는 원인 분석하여, 고분자 간의 접착을 합리적으로 이해할 수 있는 거동을 제시하였다. 또한, 표면처리 기술을 도입해 고분자 복합체와 금속산화물 필름 간의 접착력을 향상시켰다. 이를 통해, 높은 수증기 차폐 특성을 갖는 라미네이트를 제작할 수 있었다.

마지막으로 동력 차단 재료로 자기응답성유체에 관한 연구를 진행하였다. 그 중에서도 자기응답성 유체의 침전 안정성을 개선하기 위해 탄소나노튜브에 자성물질을 코팅한 물질을 합성하고 이를 이용해 높은 안정성을 얻는데 성공하였다.

주요어: 복합재료, 복합체, 전자파 차폐, X선 차폐, 감마선 차폐, 계면
접착, 계면 파괴 거동, 다층 구조 복합체

학번: 2013-30935

List of Publication

- [1] **Kim, Hoveon**, and Yongsok Seo. "Polymer/Polymer Interface Adhesion by in Situ Compatibilization." *Procedia materials science* 3 (2014): 1644-1649.
- [2] Oh, Kyoung Hwan, **Hoveon Kim**, and Yongsok Seo. "A facile synthetic route to novel thermotropic liquid crystalline polymers and characterization of their mesophases." *RSC Advances* 7.47 (2017): 29772-29778.
- [3] Park, Seongeun, **Kim, Hoveon**, Kim Yoonkwan, Kim Eunhee and Yongsok Seo. "Multilayer-Structured Non-leded Metal/Polymer Composites for Enhanced X-ray Shielding." *MRS Advances* 3.31 (2018): 1789-1797.
- [4] **Kim, Hoveon**, Daisuke Kawaguchi, Keiji Tanaka and Yongsok Seo. "Fracture Mechanism Change at a Heterogeneous Polymer–Polymer Interface Reinforced with in Situ Graft Copolymers." *Langmuir* 34.37 (2018): 11027-11033.
- [5] Lee, Horim, **Kim Hoveon**, Kim Dong Young, and Yongsok Seo. "Pure Piezoelectricity Generation by a Flexible Nanogenerator Based on Lead Zirconate Titanate Nanofibers." *ACS Omega* 4.2 (2019): 2610-2617.
- [6] Oh, Kyunghwan, **Hoveon Kim**, and Yongsok Seo. "Synthesis of novel thermotropic liquid crystalline polymers by a reactive extrusion process." *RSC Advances* 9.22 (2019): 12189-12194.
- [7] **Kim, Hoveon**, Sehyun Kim, and Yongsok Seo. "High-Performance Magnetorheological Suspensions of Fe₃O₄-deposited Carbon Nanotubes with Enhanced Stability." *MRS Advances* 4.3-4 (2019): 217-224.
- [8] **Kim, Hoveon**, Park Seongeun, Kim Sehyun, and Yongsok Seo. "Microwave Absorption and Shielding Property of Fe–Si–Al Alloy/MWCNT/Polymer Nanocomposites." *Langmuir* (2019).

- [9] **Kim, Hoveon**, Kyunghwan Oh, and Yongsok Seo. "Rheological and Mechanical Properties of a Novel Polyamide 6 Synthesized by Anionic Polymerization of ϵ -caprolactam in a Twin-Screw Extruder." *Polymer* (2019).
- [10] **Kim, Hoveon**, Kim Sehyun and Yongsok Seo. "Electromagnetic Shielding Property of magnetic particle coated CNT", *in preparation*.
- [11] **Kim Hoveon**, and Yongok Seo. "Improvement of Mechanical Properties by Introducing Curable Functional Monomers in Stereolithography 3D Printing", *in preparation*.

Appendix

Appendix A. Improvement of Mechanical Properties by Introducing Curable Functional Monomers in Stereolithography 3D Printing

A. 1. Introduction

Additive manufacturing, commonly referred to as 3D printing (3DP), has emerged as a powerful and dynamic technology to produce a wide range of complex structures/components, already enabling rapid prototyping and beginning to impact industrial production significantly. 3D printing can provide a simple route to the production of highly customized structures, tailored toward specific applications, while simultaneously reducing the cost and time associated with traditional subtractive fabrication techniques. [1-5]

Among all the 3DP technologies, stereolithography (SLA) is used to produce models, prototypes, and fabricate final parts of products. In SLA printing process, UV curable resin is used. During printing process, the stereolithography resin (SLR) is polymerized layer by layer by an UV laser or other sources. After being cured by the UV light, a crosslinked polymer network is formed. The main advantage over the other 3D printing techniques is high resolution, dimensional accuracy, and surface quality.[6-7]

Nowadays, commercial desktop stereolithography apparatus were developed.[8-9] These desktop level stereolithography apparatuses usually use bottom up systems with inexpensive laser (405 nm wavelength) and the acrylate based SLR as the printing materials due to the limited choice of photoinitiators (radical polymerization). In bottom up system, the curing of the SLR layer occurs directly above the resin tank. Then, the cured layer is detached from the tank, as the platform move upwards (peel off process). After that, uncured resins fill the gap between the cured layer and the bottom of the tank and curing process proceeds again. By repeating these steps, the final part can be obtained.[10]

However, poor mechanical properties of SLR due to insufficient interlayer adhesion are common to most desktop SLA apparatus, limiting their application as functional materials.[11] Past research proposes the printed parts are incompletely cured.[12] Therefore, the several researches have been conducted to improve the mechanical properties of SLA resins. [13-16]

Generally, dual-cure system contains two kinds of reactive functional groups: a UV-curable functional groups and a thermally curable functional group. After being heated and exposed to UV light, such a system will form an enhanced crosslinked network.[17-20] This approach can effectively solve the problem like insufficient curing by UV irradiation at the interface between layers. In this study, we introduced reactive functional groups into the SLR resins which contains acrylate double bond only to construct the dual-cure system in 3D stereolithography.

A. 2. Experimental Section

A. 2. 1. Materials

A commercial stereolithography resin (Clear Resin, XYZ Printing) was used as a base resin. Clear Resin consists of urethane diacrylates, acrylic monomers and photoinitiator. Glycidyl methacrylate (GMA) was used to introduce for the reaction with the hydroxyl groups of 2-hydroxy-3-phenoxypropyl acrylate (HPA). The photoinitiator was diphenyl(2,4,6-trimethylbenzoyl)phosphine oxide. 1,8-Diazabicyclo[5.4.0]-7-undecene (DBN) was used as a thermal catalyst to promote the reaction between epoxy and hydroxyl group. All reagents were used without any further purification.

A. 2. 2. Preparation of dual curable stereolithography resin

To formulate the dual curable stereolithography resins (SLRs), the mixture of thermally curable acrylic monomers (GMA and HPA) was prepared first. The equivalent ratio of the epoxy and hydroxyl groups was kept at 1. The mixture contains 5 wt% of the photoinitiator and 3 wt% of thermal catalyst was stirred at room temperature for 2 h before use. The ratio of the neat SLR to the acrylic mixture was optimized to 4 through the several pre-experiments.

A. 2. 3. 3D printing by using stereolithography

A Nobel 1.0 desktop 3D printer (XYZ Printing) was used to fabricate three-dimensional parts. This device is equipped with a 405 nm wavelength laser. Multiple printing options are available, but in this study, we have set all options to default and set the layer thickness to only 50 μm . Geometry of the test specimens used in this study was fabricated according to the ASTM D638 Type V.[21] In order to cause the fracture to occur at the interlayer, test specimens were printed in the vertical direction. After printing, the samples were washed by isopropanol several times to remove uncured SLRs. Dual cured samples were cured in a convection oven for two hours at various temperature (80 $^{\circ}\text{C}$, 120 $^{\circ}\text{C}$, and 160 $^{\circ}\text{C}$) to achieve fully cured 3d printing samples. Table 1 shows the description for the sample in this study.

A. 2. 4. Characterization

Chemical reaction involving thermally curable functional groups (epoxy and hydroxyl groups) were analyzed by differential scanning calorimetry (DSC, DSC 823e, Mettler Toledo). In DSC measurements, the printed sample (UV-cured) was heated from 30 $^{\circ}\text{C}$ to 200 $^{\circ}\text{C}$ at 5 $^{\circ}\text{C min}^{-1}$.

The FT-IR spectra were obtained before and after thermal curing process using a FT-IR instrument (TENSOR 27, Bruker) equipped with an attenuated total reflectance (ATR) accessory. Quantitative analysis was performed by monitoring the disappearance of the band at 910 cm^{-1} of the C-O bond in the epoxy group upon heat

treatment. Conversion of epoxy groups was calculated through the area of the absorption peak at 910cm^{-1} .

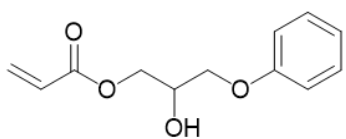
The gel fraction was measured to confirm the crosslinked structure of the cured samples after UV and thermal curing. The UV and dual-cured samples were soaked in acetone for 24 h at $60\text{ }^{\circ}\text{C}$. The remaining part was dried under a vacuum oven for 24 h. The gel fraction was calculated using the following equation.

$$\text{Gel fraction (\%)} = (W_f / W_i) \times 100 \quad (\text{A. 1})$$

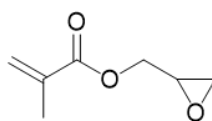
where W_i is the initial weight of the sample, and W_f is the weight of remaining part.[19] The measurements were performed five times for each sample and the average value was used.

The mechanical properties such as the tensile strength, elongation at break, and elastic modulus were obtained according to ASTM D638. Tensile test of specimens was conducted on a universal test machine (Instron 5543, Instron). The crosshead speed was 10 mm min^{-1} .

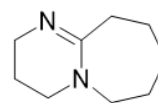
Dynamic mechanical analysis (DMA Q800, TA Instrument) was performed to observe the temperature dependence of viscoelastic properties for the 3D printed final parts. The DMA test was performed with a frequency of 1 Hz, an oscillating amplitude of 0.05 % and a heating rate of $2^{\circ}\text{C min}^{-1}$. The temperature dependence of storage modulus, E' and loss tangent ($\tan \delta$) was measured from $-20\text{ }^{\circ}\text{C}$ to $140\text{ }^{\circ}\text{C}$.



(a)



(b)



(c)

Figure A. 1. Chemical structure of (a) HPA, (b) GMA, and (C) DBN

Table A. 1. Formulation of stereolithography resins

	Clear Resin	Thermally monomer mixture	Post Cure
Reference	100	0	No Post cure
Mix-Uncure	80	20	No Post-cure
Mix-Heatcure	80	20	Heat Post-cure (Dual Cure)

A. 3. Results and Discussion

The reaction scheme of the chemical reaction in dual curable SLRs during post heat treatment is represented in Scheme 1. Without thermally curable monomers, the crosslinking network was formed by the reaction of C=C double bonds only. When the curable mixture was introduced to neat SLR, additional bonds were formed by the chemical reaction between thermally curable functional group and these bonds contributed to the increase of crosslinking density of the existing polymer structure.

Figure A. 1 shows the DSC thermogram of UV cured sample. As shown in Figure A.1, the exothermic peak of the curing reaction was observed. By introducing the thermal catalyst, the peak temperature decreased 30 °C.

To investigate the reaction of epoxy with hydroxyl groups after heat treatment, we analyzed the FT-IR spectra. In Figure A.2, the epoxy group peak at approximately 910cm^{-1} appeared by the addition of the curable mixture and disappeared after thermal curing process. This implies that the epoxy groups reacted with the hydroxyl groups almost completely. About 90% of epoxy groups reacted after heat curing process and unreacted part was due to the reduction of chain mobility in the crosslinking network.[22]

As shown in Figure A.3, a gel fraction corresponding to a crosslinking density of 90% was achieved with UV curing in neat SLA resin. However, a gel fraction of the uncured sample decreased by about 10% with UV curing. The introduction of the curable mixture which having a single C=C bond per monomer decreases the crosslinking that was occurred by UV curing. Also, the change in transparency of

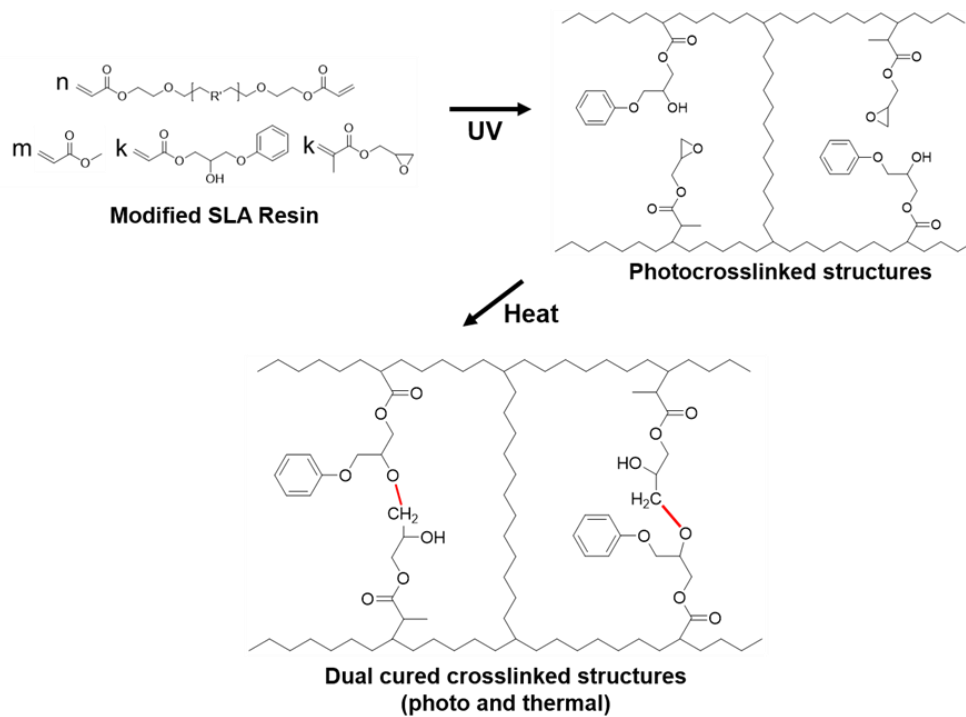
the modified SLA resin could affect the crosslinking reaction. After thermal curing process, the gel fraction increased slightly to about 90%. This effect is due to the bonding between the epoxy and hydroxyl groups in the curable mixture but there was little difference from the neat SLA resin. Therefore, the crosslinking density of the final parts could be evaluated as similar as that of the neat SLA resin.

Figure A.4 shows the temperature dependence of the mechanical properties. The tensile properties were improved when the curing temperature was increased to 120 °C. However, when the temperature increased from 120 °C to 160 °C, no improvement in tensile properties was not observed. This is because the reaction between functional groups didn't occur sufficiently at 80°C and the reaction was completely occurred at 120 °C or 160°C.[18, 23] Based on the result, we set the optimal thermal curing condition for 2 h at 120 °C.

Figure A.5(a) shows the stress-strain curve and the tensile properties of the samples. The tensile strength and elongation at break of SLA resins are shown in Figure A.5(b). When introducing the reactive functional monomers mixture, the uncured sample showed a lower tensile strength and a longer elongation at break. This behavior can be interpreted as the decrease of crosslinking density as well as incomplete curing of the resins due to the change of SLA resins properties. [11, 24] In the dual-cured sample, the tensile strength was significantly improved and elongation at break decreased slightly. This effect in mechanical properties is well known by increasing the crosslinking density.[23, 25] The noticeable point is that the mechanical properties of the heat-cured sample was greatly improved even though the overall crosslinking density evaluated by the extraction was similar. This

implies that the improvement in mechanical properties is due to other effects than the increase of the overall crosslinking density. Although, the reactions between thermally curable functional groups don't always occur between the interfaces, some of them may react in the vertical direction at the interlayer and contribute to the improvement of the interlayer adhesion.

DMA measurement was performed to investigate the viscoelastic properties of the final parts to understand the structure/properties relationships. The temperature associated with the peak of loss tangent ($\tan \delta$) is defined as the glass transition temperature (T_g). Similar remarkable changes could be observed in storage modulus with change in mechanical properties as shown in Figure A.6(a). The uncured sample exhibited that lower storage modulus values compared to reference, while the dual cured sample showed the highest storage modulus due to the formation of dense crosslinking network via the UV-thermal dual cure process.[15, 26] Figure A.6(b) shows the temperature dependence of loss tangent for all samples. The glass transition temperature was slightly increased by 7°C due to the increase of the crosslinking density. On the other hand, the dual cured sample showed a higher $\tan \delta$ value than the reference, even though it had a high crosslinking density. The height of the $\tan \delta$ reflects the mobility of the polymer segments between crosslinks in the glass transition region.[26] This transition could be due to the increased linearity of the polymer segments between crosslinks with the introduction of thermally curable monoacrylates. These results agreed with the result from the mechanical properties – higher tensile strength, longer elongation at break.



Scheme A. 1. Reaction scheme of the reaction during the UV and thermal cure

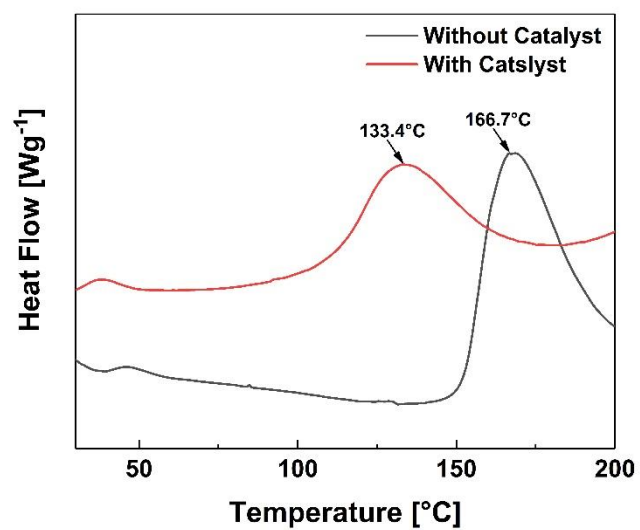


Figure A. 1. DSC thermograms of UV cured mixed resin

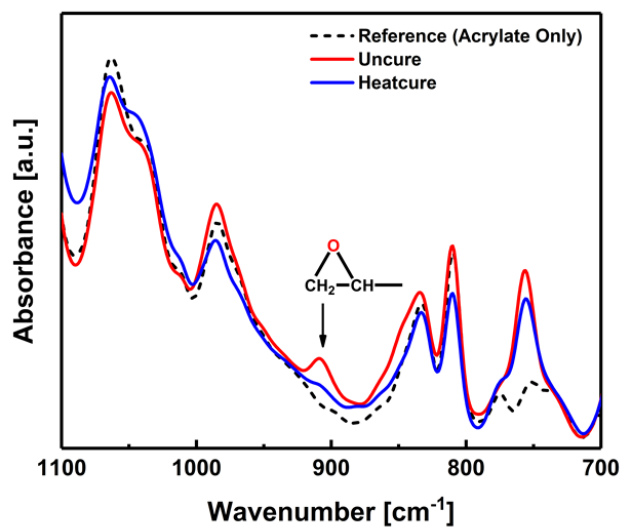


Figure A. 2. FT-IR Spectra of neat SLR and modified SLR before and after thermal curing process

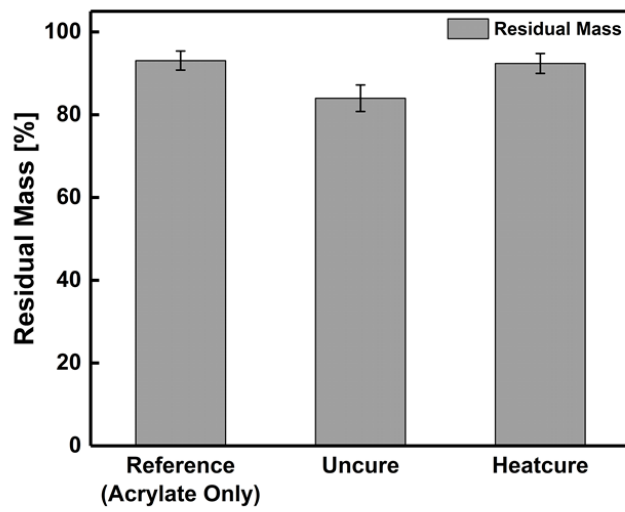


Figure A. 3. The gel fraction of different samples

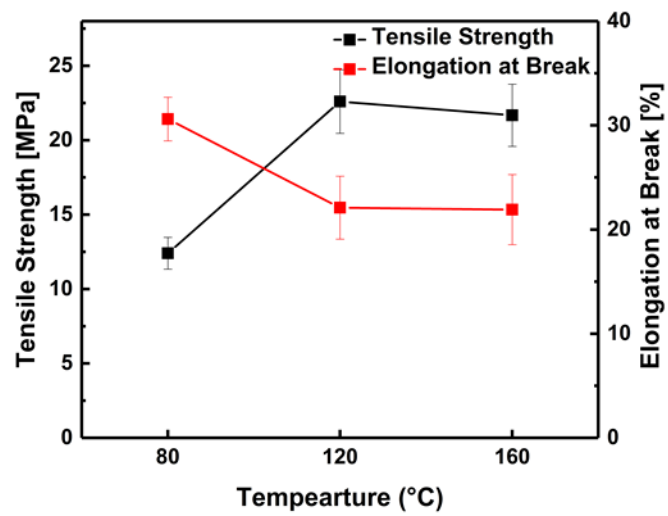


Figure A. 4. The temperature dependence of the mechanical properties of dual-cured sample

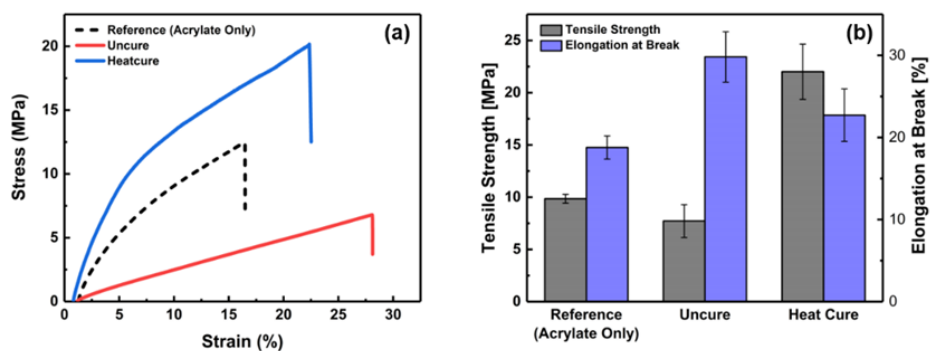


Figure A. 5. (a) Stress-strain curve and (b) tensile properties of different samples

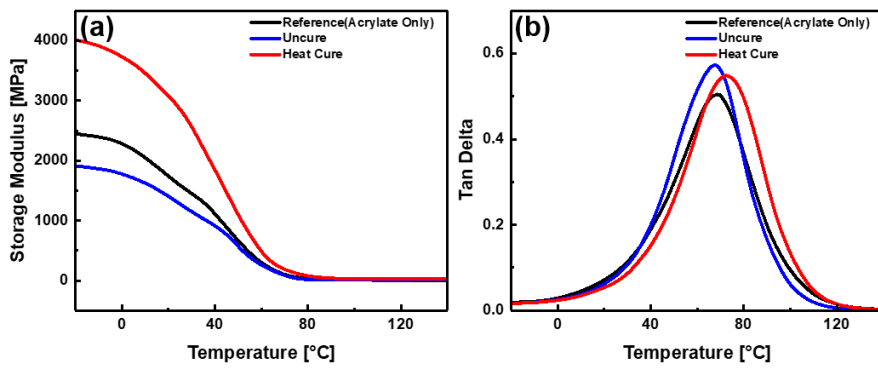


Figure A. 6. The DMA test result of different samples: (a) storage modulus and (b) $\tan \delta$

A. 4. Conclusion

A novel three-dimensional composite curing process was developed by adding acrylic monomers having a thermally curable group in 3D stereolithography. Hydroxyl groups and epoxy groups of acrylate monomers were completely reacted during heat cure process. The dual curing process improved the mechanical properties of the final products such as tensile strength, storage modulus and elongation at break. This enhancement was caused by the development of the strong interlayer adhesion in the vertical direction as well as the increase of crosslinking density of the final parts. The newly developed three-dimensional printing and curing process enables to fabricate the final parts showing superior interlayer adhesion and the mechanical properties compared to the case which have an insufficient interlayer bonding.

A. 5. References

- [1] Bikas, H.; Stavropoulos, P.; Chryssolouris, G. Additive manufacturing methods and modelling approaches: a critical review. *Int. J. Adv. Manuf. Technol.* **2016**, *83* (1-4), 389-405.
- [2] Stansbury, J. W.; Idacavage, M. J. 3D printing with polymers: Challenges among expanding options and opportunities. *Dent. Mater.* **2016**, *32* (1), 54-64.
- [3] Chapiro, M. Current achievements and future outlook for composites in 3D printing. *Reinf. Plast.* **2016**, *60* (6), 372-375.
- [4] Levy, G. N.; Schindel, R.; Kruth, J.-P. Rapid manufacturing and rapid tooling with layer manufacturing (LM) technologies, state of the art and future perspectives. *CIRP annals* **2003**, *52* (2), 589-609.
- [5] Gao, W.; Zhang, Y.; Ramanujan, D.; Ramani, K.; Chen, Y.; Williams, C. B.; Wang, C. C. L.; Shin, Y. C.; Zhang, S.; Zavattieri, P. D. The status, challenges, and future of additive manufacturing in engineering. *Comput. Aided. Des.* **2015**, *69*, 65-89.
- [6] Lee, J.-Y.; An, J.; Chua, C. K. Fundamentals and applications of 3D printing for novel materials. *Appl. Mater. Today.* **2017**, *7*, 120-133.
- [7] Kruth, J. P.; Leu, M.-C.; Nakagawa, T. Progress in additive manufacturing and rapid prototyping. *Cirp Annals* **1998**, *47* (2), 525-540.
- [8] He, Y.; Wu, W.-b.; Fu, J.-z. Rapid fabrication of paper-based microfluidic analytical devices with desktop stereolithography 3D printer. *Rsc Advances* **2015**, *5* (4), 2694-2701.
- [9] Monzón, M.; Ortega, Z.; Hernández, A.; Paz, R.; Ortega, F. Anisotropy of photopolymer parts made by digital light processing. *Materials* **2017**, *10* (1), 64.
- [10] Manapat, J. Z.; Chen, Q.; Ye, P.; Advincula, R. C. 3D printing of polymer nanocomposites via stereolithography. *Macromol. Mater. Eng.* **2017**, *302* (9), 1600553.
- [11] Salmoria, G. V.; Ahrens, C. H.; Beal, V. E.; Pires, A. T. N.; Soldi, V. Evaluation of post-curing and laser manufacturing parameters on the properties of SOMOS 7110 photosensitive resin used in stereolithography. *Mater. Des.* **2009**, *30* (3), 758-763.

- [12] Fuh, J. Y. H.; Lu, L.; Tan, C. C.; Shen, Z. X.; Chew, S. Curing characteristics of acrylic photopolymer used in stereolithography process. *Rapid Prototyp. J.* **1999**, *5* (1), 27-34.
- [13] Cho, Y. H.; Lee, I. H.; Cho, D. W. Laser scanning path generation considering photopolymer solidification in micro-stereolithography. *Microsyst. Technol.* **2005**, *11* (2-3), 158-167.
- [14] Heller, C.; Schwentenwein, M.; Russmueller, G.; Varga, F.; Stampfl, J.; Liska, R. Vinyl esters: low cytotoxicity monomers for the fabrication of biocompatible 3D scaffolds by lithography based additive manufacturing. *J. Polym. Sci. A* **2009**, *47* (24), 6941-6954.
- [15] Mohtadizadeh, F.; Zohuriaan-Mehr, M. J.; Hadavand, B. S.; Dehghan, A. Tetra-functional epoxy-acrylate as crosslinker for UV curable resins: synthesis, spectral, and thermo-mechanical studies. *Prog. Org. Coat.* **2015**, *89*, 231-239.
- [16] Cui, J.; Yu, G.; Pan, C. A novel UV-curable epoxy acrylate resin containing arylene ether sulfone linkages: Preparation, characterization, and properties. *J. Appl. Polym. Sci.* **2014**, *131* (22).
- [17] Chen, W.-H.; Chen, P.-C.; Wang, S.-C.; Yeh, J.-T.; Huang, C.-Y.; Chen, K.-N. UV-curable PDMS-containing PU system for hydrophobic textile surface treatment. *J. Polym. Res.* **2009**, *16* (5), 601-610.
- [18] Decker, C.; Masson, F.; Schwalm, R. Dual-curing of waterborne urethane-acrylate coatings by UV and thermal processing. *Macromol. Mater. Eng.* **2003**, *288* (1), 17-28.
- [19] Decker, C.; Viet, T. N. T.; Decker, D.; Weber-Koehl, E. UV-radiation curing of acrylate/epoxide systems. *Polymer* **2001**, *42* (13), 5531-5541.
- [20] Park, C.-H.; Lee, S.-W.; Park, J.-W.; Kim, H.-J. Preparation and characterization of dual curable adhesives containing epoxy and acrylate functionalities. *React. Funct. Polym.* **2013**, *73* (4), 641-646.
- [21] International, A. *ASTM D638-14, Standard Test Method for Tensile Properties of Plastics*, ASTM International: 2015.
- [22] Dean, K.; Cook, W. D.; Burchill, P.; Zipper, M. Curing behaviour of IPNs formed from model VERs and epoxy systems: Part II. Imidazole-cured epoxy. *Polymer* **2001**, *42* (8), 3589-3601.

- [23] Noh, S. M.; Lee, J. W.; Nam, J. H.; Byun, K. H.; Park, J. M.; Jung, H. W. Dual-curing behavior and scratch characteristics of hydroxyl functionalized urethane methacrylate oligomer for automotive clearcoats. *Prog. Org. Coat.* **2012**, *74* (1), 257-269.
- [24] Colton, J.; Blair, B. Experimental study of post-build cure of stereolithography polymers for injection molds. *Rapid Prototyp. J.* **1999**, *5* (2), 72-81.
- [25] Krumova, M.; Lopez, D.; Benavente, R.; Mijangos, C.; Perena, J. M. Effect of crosslinking on the mechanical and thermal properties of poly (vinyl alcohol). *Polymer* **2000**, *41* (26), 9265-9272.
- [26] Asif, A.; Shi, W.; Shen, X.; Nie, K. Physical and thermal properties of UV curable waterborne polyurethane dispersions incorporating hyperbranched aliphatic polyester of varying generation number. *Polymer* **2005**, *46* (24), 11066-11078.